



HAL
open science

Controlled dynamics of a levitated nanoparticle in a tailored optical potential

Damien Raynal

► **To cite this version:**

Damien Raynal. Controlled dynamics of a levitated nanoparticle in a tailored optical potential. Data Analysis, Statistics and Probability [physics.data-an]. Université Paris-Saclay, 2023. English. NNT : 2023UPASP126 . tel-04510266

HAL Id: tel-04510266

<https://theses.hal.science/tel-04510266>

Submitted on 18 Mar 2024

HAL is a multi-disciplinary open access archive for the deposit and dissemination of scientific research documents, whether they are published or not. The documents may come from teaching and research institutions in France or abroad, or from public or private research centers.

L'archive ouverte pluridisciplinaire **HAL**, est destinée au dépôt et à la diffusion de documents scientifiques de niveau recherche, publiés ou non, émanant des établissements d'enseignement et de recherche français ou étrangers, des laboratoires publics ou privés.

Maîtrise de la dynamique d'une
nanoparticule en lévitation dans un
potentiel optique contrôlé
*Controlled dynamics of a levitated nanoparticle in a
tailored optical potential*

Thèse de doctorat de l'université Paris-Saclay

École doctorale n° 572, Ecole Doctorale Ondes et Matière (EDOM)
Spécialité de doctorat: Physique
Graduate School : Physique, Référent : ENS Paris-Saclay

Thèse préparée dans le laboratoire Lumière Matière et Interfaces (LuMIIn),
sous la direction de Jean-Sébastien LAURET, Professeur à l'ENS Paris-Saclay,
membre Junior de l'Institut Universitaire de France,
et le co-encadrement de Loïc RONDIN, maître de conférences à l'Université
Paris-Saclay

Thèse soutenue à Paris-Saclay, le 06 Octobre 2023, par

Damien RAYNAL

Composition du jury

Thierry Lahaye
Directeur de recherches, Université Paris-Saclay
Yann Louyer
Maître de conférences, Université de Bordeaux
Eric Lutz
Professeur, University of Stuttgart
Nadine Meyer
Associate Professor, ETH Zürich

Président
Rapporteur & Examineur
Rapporteur & Examineur
Examinatrice

Title: Controlled dynamics of a levitated nanoparticle in a tailored optical potential

Keywords: Optical tweezers, nanoparticle, out-of-equilibrium thermodynamics, nonlinearity

Abstract: Optical levitation of nanoparticles in vacuum emerged over the last decade as an attractive platform to study various phenomena, such as fundamental interactions, quantum physics at the mesoscale, as well as out-of-equilibrium nanothermodynamics. A critical advantage of this approach over competing systems is the unprecedented control that can be enforced on the levitated particle and its environment. In this context, finely tuning the trapping potential in time and space represents a welcomed addition to the existing toolbox, allowing for example, the generation of non-Gaussian statistics.

One goal of this thesis is to study out-of-equilibrium dynamics in the underdamped regime, which is of fundamental and practical interest since most nano-mechanical systems are operated in this regime. The stochastic nature of the thermodynamic processes at play was first probed by studying the relaxation of a levitating particle between two thermal equilibria. This highlighted the existence of a characteristic relaxation timescale, corresponding to the time necessary for the particle to dissipate its excess energy to the surrounding bath. Subsequently, shortcuts to equilibrium pro-

ocols were implemented and tested for the first time in the underdamped regime, enabling an acceleration of the relaxation time of the particle by more than one order of magnitude. Further, these protocols proved to be robust to variations of the system parameters for modest accelerations.

Next, the generation and characterization of arbitrarily shaped potentials was explored, at first, to extend the study of thermodynamic processes to the case of non-harmonic potentials, where nonlinearities come into play. The superposition of multiple beams diffracted by an acousto-optic modulator was used to generate various potentials, from harmonic through flat to double-well geometries, thus allowing to tune their nonlinearities. To reconstruct unambiguously the real potential shape from the particle dynamics, the range of detection was extended five-fold by an original use of the Unscented Kalman filter, thus covering the full extent of the potential.

This work paves the way for the study of general state-to-state transformations between tailored potentials and opens a new playground to study thermodynamics at the nanoscale.

Titre: Maîtrise de la dynamique d'une nanoparticule en lévitation dans un potentiel optique contrôlé

Mots clés: Pincés optiques, nanoparticule, thermodynamique hors d'équilibre, non-linéarités

Résumé : Au cours de la dernière décennie, la lévitation de nanoparticules dans le vide s'est illustrée comme une plateforme de choix pour l'étude de nombreux phénomènes, parmi lesquels les interactions élémentaires, la physique quantique à l'échelle mésoscopique, ainsi que la nanothermodynamique hors d'équilibre. Comparée à d'autres systèmes, un atout majeur de cette approche réside dans le contrôle remarquable qu'il est possible d'exercer sur la nanoparticule et son environnement. Dans ce contexte, la maîtrise complète de l'évolution spatio-temporelle du potentiel de piégeage constitue un ajout significatif aux techniques existantes, en permettant par exemple la génération de statistiques non Gaussiennes.

L'un des objectifs de cette thèse est l'étude et le contrôle de la dynamique hors équilibre d'une nanoparticule dans le régime sous-amorti, dont l'importance est à la fois fondamentale et pratique, étant donné qu'une grande partie des systèmes nano-mécaniques opère dans ce régime. La nature stochastique des processus thermodynamiques à l'œuvre a d'abord été étudiée à travers la relaxation d'une particule en lévitation entre deux équilibres thermiques. A ainsi été mis en lumière un temps de relaxation caractéristique, correspondant au temps nécessaire à la dissipation de l'énergie de la particule dans son environnement. Par la suite, des

protocoles de raccourcis vers l'équilibre ont pour la première fois été implémentés et testés dans le régime sous-amorti, permettant d'accélérer le retour à l'équilibre de la particule d'un ordre de grandeur. Pour de modestes accélérations, ces protocoles se sont avérés robustes à un changement dans les paramètres du problème.

La génération et la caractérisation de potentiels de formes arbitraires ont ensuite été explorées, avec comme objectif initial d'étendre l'étude de processus thermodynamiques au cas de potentiels non harmoniques, pour lesquels les non-linéarités entrent en jeu. À l'aide d'un modulateur acousto-optique permettant de générer une superposition de faisceaux diffractés, différents potentiels ont ainsi été générés : harmoniques, plat, double puits... permettant un ajustement des non-linéarités. Pour reconstituer de façon non ambiguë la forme réelle du potentiel à partir de la dynamique de la particule, une utilisation originale du filtre de Kalman sans parfum (*Unscented Kalman Filter*) a permis d'étendre la plage de linéarité de la détection d'un facteur cinq, couvrant ainsi toute l'étendue du potentiel.

Ce travail ouvre la voie à l'étude de transformations générales d'état à état entre potentiels arbitraires, et offre de nouvelles perspectives à l'étude de la thermodynamique à l'échelle nanométrique.

Contents

1	Introduction	11
1.1	Non-equilibrium physics	11
1.2	Optical tweezers	14
1.3	Outline of the thesis	16
2	Trapping of a levitated particle in vacuum	19
2.1	Optical forces	19
2.1.1	Polarizability	22
2.1.2	Strongly focused beam	22
2.2	Dynamics of a trapped particle	28
2.2.1	Langevin equation	28
2.2.2	Response function and Power spectral distribution	30
2.2.3	Equilibrium probability distribution and Fokker-Planck equation	31
2.3	Experimental setup	33
2.3.1	Control of the trapping potential	34
2.3.2	General description	36
2.4	Measurements and (linear) calibration	41
2.4.1	Detection in the paraxial approximation	43
2.4.2	Calibration in the linear range	47
2.4.3	Realistic model of extended measurement	49
3	Shortcuts to equilibrium in the underdamped regime	57
3.1	Relaxations in the overdamped and underdamped regimes	58
3.1.1	STEP protocols	58
3.1.2	Theoretical model of relaxation	59
3.1.3	Experimental results	60
3.2	Shortcuts to equilibrium	65
3.2.1	Principle of ESE protocol	66
3.2.2	Implementation	68
3.2.3	Experimental results	68
3.2.4	Energetics	72
3.3	Robustness of ESE protocols	74
3.4	Conclusion	78
4	Generation and characterization of arbitrary potentials	79
4.1	Generation of arbitrary potentials	79
4.1.1	Beam shaping of focal fields	80
4.1.2	1D arbitrary potential from single beams superposition	81
4.1.3	Control of potential nonlinearities in a dual beams configuration	85

4.2	Characterization of nonlinear measurements and effects on Gaussian distributions	89
4.2.1	Study of displaced harmonic traps	89
4.2.2	Existing approaches	91
4.3	Non-linear Kalman filter	92
4.3.1	Principle and state of the art	92
4.3.2	Validation of UKF on simulated data	95
4.3.3	Experimental demonstration of UKF	96
4.3.4	Observation of the particle dynamics in a strongly nonlinear potential	99
4.3.5	Conclusion	102
5	General Conclusion	103

Remerciements

Ce jour d'automne qui ressemblait aux derniers du printemps le remplissait de bonheur. [...]

Il roulait comme une vague parmi ses frères-vagues, s'il est permis de s'exprimer ainsi ; et pourquoi ne serait-ce pas permis, lorsqu'un homme qui s'est usé à un travail solitaire retrouve la communauté, et le bonheur de couler dans la même direction qu'elle !

— Robert Musil (trad. Philippe Jaccottet), *L'HOMME SANS QUALITÉS* (1930)

Arrivé au terme de cette aventure humaine et scientifique qu'est une thèse, et en partance vers d'autres horizons, c'est avec une émotion non feinte que je formule ces remerciements.

Ces trois lumineuses années passées à Orsay, je les dois évidemment avant tout à mes directeurs de thèse, Jean-Sébastien Lauret et Loïc Rondin, qui m'ont d'abord fait confiance en m'acceptant en stage de M2 (merci Clarisse pour m'avoir la première indiqué qu'il n'était pas nécessaire de s'expatrier pour travailler sur les pinces optiques), puis en thèse, sur la généreuse recommandation de mes précédents encadrants de stage à l'IMPMC, Andrea Gauzzi et Yannick Klein. Au-delà d'une disponibilité dont bien des thésards seraient envieux, j'ai beaucoup apprécié votre patience et votre bienveillance, qui m'ont permis de mener à bien ce travail en essayant de concilier liberté, rigueur et pragmatisme.

Je tiens également à remercier les membres de mon jury, qui m'ont fait l'honneur de lire ce travail et d'assister à ma soutenance, en les complétant par des questions qui continuent de stimuler ma réflexion : Thierry Lahaye en tant que président du jury, Eric Lutz et Yann Louyer en leur qualité de rapporteurs, et Nadine Mayer en tant qu'examinatrice.

La première moitié de cette thèse, portant sur l'implémentation de raccourcis vers l'équilibre, a été l'opportunité d'une collaboration très fructueuse avec Emmanuel Trizac et David Guéry-Odelin. Et je suis bien conscient de la chance que j'ai eue d'échanger avec des théoriciens accessibles et pédagogues comme l'ont toujours été Emmanuel et David.

En changeant un peu de focale, il me faut ici dire quelques mots de la vie quotidienne au LuMIn.

Me conformant sans originalité à la structure organisationnelle de notre laboratoire, je tiens d'abord à exprimer toute ma gratitude envers notre directeur, Fabien Brete-

naker, qui nous a très gentiment prêté le Mephisto MOPA nécessaire aux premières expériences de piégeage au début de ma thèse. Sur un plan extra-scientifique, merci Fabien de m'avoir fait découvrir, à côté du maestro André Rieu, cet autre géant du kitsch, Richard Clayderman.

Je remercie également le services administratif du laboratoire, et en particulier Céline Fortabat, pour avoir toujours été là quand il s'agissait d'organiser une mission ou de préparer une commande, ce qui est un peu le nerf de la guerre pour faire avancer une thèse.

Un autre élément essentiel a été le concours d'ingénieurs mécaniciens, à l'ISMO d'abord, puis au 505, en la belle personne de Sébastien Rousselot (qui, quand il n'est pas occupé à subvenir aux multiples demandes des chercheurs, est également prêt à faire le taxi pour organiser un pot de thèse).

Ma thèse a encore bénéficié du soutien de talentueux ingénieurs en électronique, Colin Lopez et Simon L'Hortet, qui ont conçu et réalisé la photodiode quatre quadrants (QPD) qui a permis de considérablement simplifier nos mesures.

Avec Fabien et Sébastien, c'est également Gaëlle Allard et Elsa Cassette que je remercie pour s'être occupés, à côté de leurs emplois du temps déjà chargés, de la vie quotidienne au 505, en affrontant avec patience et ténacité les obstacles (pour rester diplomate) qui ont accompagné l'installation dans ce bâtiment.

Last but not least, j'ai une pensée pleine d'affection pour Laurence, la gardienne de ces lieux, dont la pugnacité face aux pratiques illégales des camions de nettoyage de la société "Les Balais Roses" (choix de nom pour le moins douteux) n'a d'égale que la bonne humeur qu'elle nous communiquait à chacune de ses rondes.

Le plus dur maintenant : remercier tous les stagiaires, thésards, postdocs dont j'ai croisé la route, en essayant d'en oublier le moins possible (pardon d'avance).

En premier lieu, mon camarade de lutte, qui a commencé sa thèse en même temps que moi, Hugo. Si les années ont hélas dégarni ton front plus vite que le mien, ce n'est certainement que pour mettre davantage en valeur cette tête bien faite, capable de mener de front l'organisation d'afterworks entre thésards, le démontage et remontage de la macro-PL, deux sujets de thèse, et j'en passe (on me dit que tu n'as jamais été observé dans la même pièce que le mêmeur masqué, mais j'en dis sans doute déjà trop). Je suis certain que tu feras bon usage des pins "EM!" que je t'ai laissé, et que leur aspect déjà dépassé te rappellera qu'il faut, selon le mot du poète, prendre garde "aux conservateurs de vieilles anarchies"...

Thomas Liu et Thomas Campos ensuite, deux individus qui au-delà du prénom, partagent également un goût inné pour la chose bien faite, en science comme en humanité. Vos qualités ont suscité en bien des occasions mon admiration sincère, et j'avoue que le rêve hawaïen si bien vendu par le vlogueur Campos est peut-être pour quelque chose dans ma décision d'aller explorer à mon tour d'autres horizons. Pour ce qui est du groupe lévitation, j'ai eu la chance d'être pendant mon stage de M2 et au début de ma thèse guidé par François et Timothée. J'ai ensuite eu le

plaisir de travailler avec Léo, Bastien, Pierre et Ines, Lucas et tout dernièrement Alex, en essayant de partager mon "savoir", ce qui se résumera peut-être pour eux à ce mantra : être patient et prudent dans ses mouvements.

J'ai aussi eu le bonheur de partager deux de ces trois années avec Joanna et Christine, deux postdocs au grand coeur. J'ai toujours en mémoire nos riches débats sur la marche du monde, Dalida ou la dialectique du taboulé et de la semoulette! Pendant ma dernière année, j'ai aussi fait la connaissance des doctorants de Fabien et Fabienne, Joseph, Duc-Ahn, et Sonya, qui au-delà de leurs mérites sur le plan scientifique, se sont révélés de passionnants interlocuteurs, avec des points de vue qui souvent complétaient utilement le solipsisme franco-français, et donnaient envie de découvrir le vaste monde.

Et enfin il y a aussi tous les autres, que j'ai peut-être moins côtoyé de par leur éloignement relatif à l'ENS, mais qu'il était toujours très plaisant de retrouver au détour d'un séminaire jeune ou d'un verre : Gauthier, Isis, Alan, Cassandra, Marie-Charlotte et tant d'autres...

Je n'oublie pas non plus les rencontres de l'école d'été "The New Mechanics" à laquelle j'ai eu la chance de participer durant tout le mois d'août 2022 aux Houches, et où à côté de grands noms du domaine, j'ai pu côtoyer la relève internationale, sur les bancs de l'amphi comme dans de splendides randonnées. Merci encore pour tous ces bons moments aux gentils organisateurs, Pierre-François Cohadon, Samuel Deléglise et Pierre Verlot.

Un peu plus loin dans le temps, je pense aussi à mes camarades du M2 LOM, en premier lieu les membres du "FC Saclay", Clarisse, Antoine et Guillaume, avec qui j'ai pu découvrir les environs d'Orsay au-delà de ma rue. Merci aussi à Maxime pour avoir entretenu la connexion du M2 SMNO canal lévitation, au détour de nos rencontres à Benasque ou à l'ENS Ulm.

Toujours plus loin, je mêle ici deux groupes qui se sont peu à peu confondus au fil des ans, celui de mes amis de Télécom Bretagne et de prépa à LLG :

Matthew, avec qui je me suis lancé dans cette aventure un peu folle de Glif it dès la sortie d'école, à une époque où nous rêvions de créer une nouvelle façon de communiquer sans se soucier de profit immédiat... raisonnement d'affreux gauchistes et/ou de fils à papa!

Arnaud, Cédric et Guillaume, autres compagnons d'école et comme moi navigateurs assez passionnés pour braver les éléments les samedis matin dans la rade de Brest, malgré l'absence récurrente et démoralisante de vent (et pardon Guillaume pour le cadre photo inutilisé depuis bientôt une dizaine d'années).

Bertrand, guide hors pair à Barcelone, qui m'a aidé à emménager puis à déménager d'Orsay, et dont la connaissance des méandres de l'aéroport Charles de Gaulle lors de mon départ me laisse supposer qu'il exerce peut-être des activités d'importations en provenance du Mexique, avec la complicité de Jessica.

Chatura, Yesmine, Julia, Céline, Alexandre, Ludovica et Matthieu, dont l'amitié continue depuis maintenant 15 ans me touche infiniment.

Benjamin, qui supporte avec abnégation depuis tant d'années mes positions les plus radicales, comme celle de systématiquement régler la destination du GPS sur Null Island (au large du Ghana), entraînant quelques détours malencontreux en Valais.

Olivier enfin, qui feint pour une raison qui m'échappe d'avoir oublié cette fin d'après-midi de septembre 2008 où, apercevant son reflet dans la vitre d'une porte coupe-feu, je me retournai en le surprenant d'un "FEVRIER !", brisant ainsi la glace qui recouvre souvent les échanges des premières semaines entre préparateurs. Merci pour ton humour d'un goût parfois douteux mais constant depuis cette époque!

J'ai déjà dépassé de beaucoup la longueur recommandée pour des remerciements, aussi je conclus ici rapidement en remerciant ma famille : mes tantes Christine, Brigitte et Babeth, mon oncle Bernard, mon cher cousin Florian, qui j'espère me pardonne certains jugements à l'emporte-pièce, mes cousins Fabreguettes de première (Marc, Catherine, Pierre, Alexandra) et deuxième (Caro, Luc, Aldine) générations, qui m'ont soutenu tout au long de mes années parisiennes.

Enfin, je pense évidemment beaucoup à mes parents et à mon frère, et je les remercie pour avoir toujours souhaité le meilleur pour moi, même si depuis une quinzaine d'année ma trajectoire a pu parfois donner l'impression d'un *Coup de Dés*. Cette thèse leur est dédiée.

1 - Introduction

Le rassurant de l'équilibre, c'est que rien ne bouge. Le vrai de l'équilibre, c'est qu'il suffit d'un souffle pour faire tout bouger.

— Julien Gracq, LE RIVAGE DES SYRTES (1951)

1.1 . Non-equilibrium physics

From its inception in the 19th century, classical thermodynamics was mostly concerned with average properties of macroscopic systems in equilibrium, *i.e.* in which these properties do not change over time. The emergence of statistical physics at the end of this century, through the works of Maxwell, Boltzmann and Gibbs, offered another description of equilibrium, which extended beyond classical systems: a system is in equilibrium when all configurations of a given energy are visited with equal probability. The introduction of probabilistic tools in physics opened a whole new window through which to peer at reality.

While classical thermodynamics is efficient to describe macroscopic systems, in which fluctuations around equilibrium are negligible, this is not the case for microscopic systems. Among different mysteries surviving at the dawn of the 20th century, the observation of the erratic motion of pollen particles in a liquid, described by Brown in 1827, was first solved by Einstein during its *annus mirabilis* [1], in 1905, and separately by Smoluchowski [2]. By giving solid ground to atomistic theory, Einstein's explanation of Brownian motion uncovered the important link between the stochastic nature of collisions between a particle and surrounding water molecules on one side, and their averaged viscous effect on the other side. A few years later, in 1909, Perrin experimentally confirmed the pertinence of this interpretation [3], in the results presented in figure 1.1.

The balance between chaotic, fluctuating collisions and viscous, dissipative damping, is called a *fluctuation-dissipation relation*, and is observed in many areas of physics, such as Johnson-Nyquist noise in electronics [7], or laser threshold [8]. These phenomena are part of a broader class of fluctuation-dissipation theorems, uncovered by Onsager [9], Callen [10] and Kubo [11]. Crucially, while the initial relation dealt with a particle at equilibrium with its environment, the subsequent developments allowed to describe systems near equilibrium. As noted by Kubo [12], these theorems have indeed two complementary aspects:

- Knowing the characteristics from a system at equilibrium, it is possible to predict its intrinsic noise or fluctuations (a topical example being Johnson-Nyquist noise in electronics).

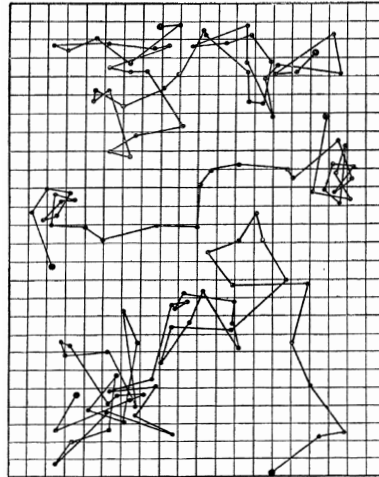


Figure 1.1: Drawings by Perrin [3] of the Brownian motion of 1 μm diameter putty particles, measured every 30 s, the mesh being 3 μm . After corroborating almost perfectly Einstein's predictions, Perrin adds: "*These drawings only give a faint idea of the prodigious entanglement of the real trajectory. If, indeed, we sampled every second, each of these segments would be replaced by a 30-sided polygonal contour relatively as complex as the one produced here, and so forth.*". This observation hints at the fractal nature of Brownian motion, which would be developed 60 years later by Mandelbrot [4].

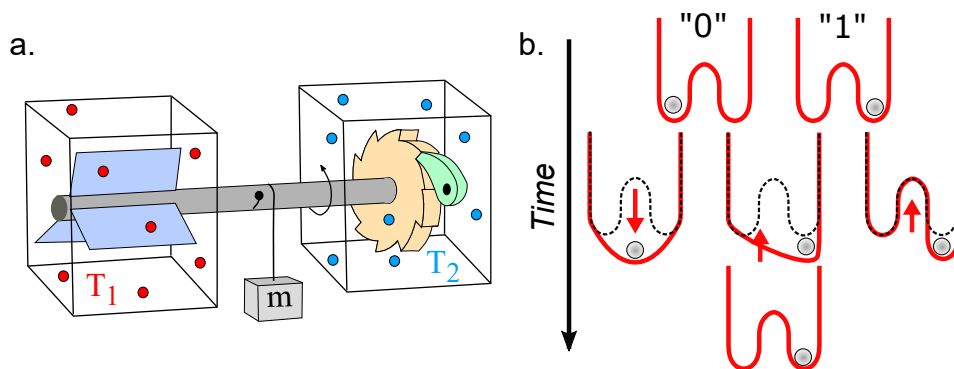


Figure 1.2: Non-equilibrium toy models. a. Feynman's ratchet, adapted from [5]. A mass m is suspended to a rod, whose right side is fixed on a ratchet mechanism, allowing it to rotate only in one direction. This motion is powered by the collisions of molecules with the paddle on the left. A naive analysis would conclude that this machine allows to extract mechanical work from thermal energy, even when $T_1 = T_2$, which is normally forbidden by the second law of thermodynamics. Feynman proved that this is not the case, because on average, the ratchet will move as much forward as backward.

b. Landauer's bound, adapted from [6]. Here, the bit state is represented by the position of a particle in one side of a double-well potential. The erasure protocol consists in an irreversible destruction of the initial information, putting the bit in the final state "1". Landauer and Bennett proved that due to the second law, erasure is a dissipative process, with at least $k_B T \ln(2)$ joules lost to the environment.

- Reversely, the statistical or spectral properties of the fluctuations can be used to determine the characteristics of the system (an example of which would be Onsager's derivation of kinetic coefficients).

Using the linear response theory developed by Kubo, an experimentalist can then perform two types of measurements to probe a physical quantity [13] :

- Susceptibility measurements, in which a system is driven by a harmonic force. An example can be found in the study of magnetic materials (spin-glasses, superconductors), through AC magnetic measurements, in which an AC field is applied to a sample to measure its magnetization properties.
- Relaxation measurements, where a force applied for a long time is suddenly changed, and the return to equilibrium of a system is observed. This is the case of nuclear magnetic resonance, in which the decay of an induced spin polarization is measured. Similarly, in optomechanics, the ring-down technique is used to determine the properties of a resonator [14, 15].

As satisfying as linear response theory is, it fails to properly describe systems far from equilibrium. In the last decade of the 20th century, a renewal of interest in out-of-equilibrium physics lead to the formulation of fundamental results by Evans [16], Jarzinsky [17, 18] and Crooks [19]. These efforts culminated in the formulation of *stochastic energetics*. This framework, developed initially by Sekimoto [20] and Seifert [21], is primarily concerned with extending the second law of thermodynamics to the microscopic world, and finding answers to the following questions :

- What is the correct definition of work, heat and entropy for stochastic processes, which are ubiquitous at small scales ? Sekimoto answered these questions by using mostly Stratonovich's definition of stochastic integrals (while noting that in certain situations, especially in chemistry, Itô's definition may be more convenient).
- Can we convert thermal energy into work ? Related to the concept of Feynman's ratchet (shown in figure 1.2 a.), in which a system apparently violates the second law of thermodynamics by extracting mechanical work from random fluctuations, this provocative question has important consequences for microscopic heat engines and molecular motors, such as those found in cells.
- What is the minimal energy necessary to perform one irreversible logical operation ? First explored through the thought experiment of Maxwell's demon, the physical nature of information was comforted by Landauer's principle (shown in figure 1.2 b.), which states that the minimal cost to erase one bit of information is $k_B T \ln(2)$ (today's computers operate about a thousand times above this limit, which leaves room for improvements).

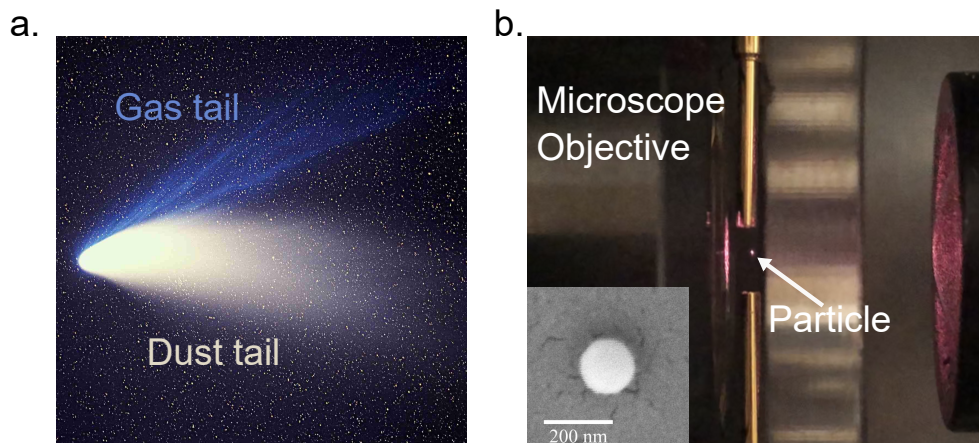


Figure 1.3: Two different observable effects of the forces exerted by light on particles
 a. Hale-Bopp comet (1997, from [29]), with two visible tails : the gas tail, produced by the interactions of ionised gases with the solar wind, and the dust tail, which is a macroscopic manifestation of the forces exerted by sunlight on microscopic particles.
 b. Silica nanoparticle (75 nm in radius, pictured in inset adapted from [30]) trapped by a strongly focused laser beam.

As noted in [22], bit erasure is only one of many operations that can be performed on a computer, and stochastic energetics is needed to go beyond this simple case.

To this day, non-equilibrium physics remains a very active field, due to the drive to engineer and control efficient artificial systems at the nanoscale, as well as the need to gain a better understanding of life's fundamental mechanisms.

Of the many experimental approaches to test and refine theoretical models, one particularly stands out: optical tweezers. We thus take a small detour to present the many important developments of this technique.

1.2 . Optical tweezers

The observation that light exerts forces on objects is ancient, dating back at least to Kepler's observation of the great comet of 1618 in *De Cometis*, in which he stated that the tails of a comet were "*formed by matter that the Sun's rays chase through their impulses outside the comet's body*" [23, 24]. A mathematical description of these physical processes was made possible only with the advance of modern electromagnetism and the introduction of Maxwell's stress tensor in 1873 [25]. The next milestone in the domain would come shortly after the invention of the laser in 1960 [26]. Scientists noticed that dust particles were sometimes trapped in amplification cavities. This raised the interest of Arthur Ashkin, who demonstrated that by using strongly focused light, it was possible to efficiently trap micron-sized particles, in single or multiple beams [27, 28].

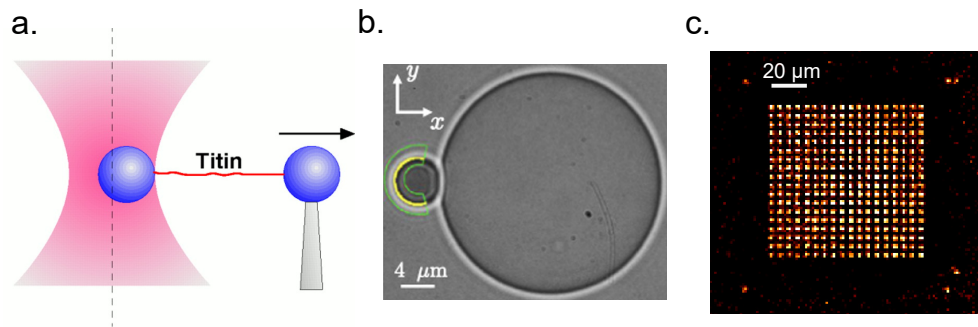


Figure 1.4: Different uses of optical tweezers : a. In biology, adapted from [37]. The two ends of a titin protein are attached to latex beads, one of them on top of a micropipette, and the second in an optical tweezer. By moving the micropipette, the protein is stretched in cycles, which generates a fluctuating force measured through the displacements of the second bead.
 b. In colloidal weak forces detection, adapted from [38]. Similar in idea, a trapped silica microsphere (on the left) is brought in close range of a bigger static one, allowing to probe the elusive Casimir interaction.
 c. In cold atoms, adapted from [39]. An array of 300 Rubidium atoms is generated by as many trapping potentials separated by 5 μm, with applications to quantum simulations.

More than a single experiment, optical tweezers became a set of techniques that encompasses diverse setups and scales, ranging from atoms and molecules to cells.

In atomic physics, Ashkin's collaborator Chu used this technique to trap neutral atoms in a single beam [31]. Many further inventions, such as magneto-optical traps [32], lead to exquisite control of assembly of atoms and the realization of Bose-Einstein condensates [33]. As a complementary approach, the interest for trapping arrays of individual atoms [34, 35] or molecules [36] as taken off in the last decade, with the possibility to use them as quantum simulators.

In out-of-equilibrium physics, while Perrin's original experiment relied on the observation of freely diffusing Brownian particles, the opportunity to trap, manipulate and, above all, perform repeated measurements of the dynamics of a single particle, allows to precisely compute statistical quantities, and thus perform extensive studies of subtle phenomena.

A first class of paradigmatic experiments were conducted with trapped microparticles suspended in fluids (*a.k.a.* colloids) [40]. To give a rapid account of their versatility, the use of colloids allowed to study :

- Validations of concepts such as fluctuation theorems and the Jarzynski equality [41].
- Implementations of Feynman's ratchet [42].
- Demonstrations of the paradoxical conversion of information to energy through

Maxwell Demon's [43], and analogously of Landauer's principle [44, 45].

- In biology, work exerted on vesicles by kinesin proteins [46], or the folding-unfolding transitions of muscle proteins [37], pictured in figure 1.4 a.
- Realization of heat engine [47].
- Anomalous relaxation such as the Mpemba effect [48].
- Anomalous diffusion [49, 50] and stochastic resetting [51].
- Weak forces such as the Casimir interaction [38], pictured in figure 1.4 b.

Closer to the subject of this thesis, trapping of particles in vacuum took off in 2008, with the impressive first demonstration that it was not only possible to directly measure the position but also the velocity of a trapped Brownian particle [52], a feat that was supposed to be technically too challenging in Einstein's seminal paper in 1905¹. Ensued successful demonstrations of generalized fluctuation theorems [54, 55], a generalisation of Landauer's bound [56], or direct measurement of Kramers turnover [57].

Compared with colloidal experiments, the dynamic regime of levitated particles is fundamentally different : in a rarefied gas, the equations describing the motion of a particle contain inertia, a quantity usually neglected in fluids due to the prevalence of viscous damping. As noted by Gieseler & Millen [58], this regime is thus more fundamental, bridging the gap with the quantum regime.

Indeed, building on this, the whole field of "levitodynamics" matured in the 2010's, borrowing techniques pioneered in cold atoms and optomechanics, such as sideband [59, 60] and feedback [61, 62, 63] cooling. This lead to remarkable advances toward cooling a particle into its quantum ground state, performed by teams in Zurich [64] and Vienna [30, 65]. The perspective of reaching the ground state with a solid object of a mass comparable to that of a Bose-Einstein condensate ($\approx 10^8$ atoms) is particularly exciting, with proposals to test quantum entanglement at the mesoscale [66, 67] as well as collapse models [68].

1.3 . Outline of the thesis

In this thesis, I propose to master the dynamics of a levitated nanoparticle toward the study and control of nano-systems out-of-equilibrium thermodynamics. I more specifically focus on controlling the particle trapping potential in time and space.

I will introduce in chapter 2 the fundamentals of optical levitation, and the characteristics of our experimental setup. I will then present the principle behind the

¹Interestingly, this experiment in vacuum predates its counterpart in liquid, where the measurement of instantaneous velocities is more demanding [53].

characterisation of levitated particle dynamics and the advantages and limitations of our measurement scheme.

In chapter 3, I will show how we use this setup to study a particle's transition between two thermal equilibria. By carefully engineering the trapping potential, I will demonstrate that the natural relaxation of the systems can be shortened, allowing us to reach equilibrium 15 times faster than the natural thermalisation time of the system.

A natural extension of this work is the study of transformations involving non-Gaussian distributions. Toward this goal, I demonstrate in chapter 4 an approach to generate arbitrarily shaped 1D optical potential for levitated particles. I then discuss the challenges raised by the measure of the particle dynamics in such potential, and I demonstrate that the use of advanced analysis methods based on Kalman filtering can overcome this limitation.

Finally, I offer a summary and some perspectives on my work in chapter 5.

2 - Trapping of a levitated particle in vacuum



— Yellow Magic Orchestra, CASTALIA (1979)

Optical tweezers, presented in the previous chapter as a potent tool to explore out-of-equilibrium physics, rest on the control of optical forces. After introducing the theory, I present our experimental setup and its crucial features :

- The ability to finely tune the coupling of our system to the environment.
- The capacity to control in time and space the trapping potential, by using an acousto-optic-modulator.

Finally, I discuss the measurement scheme we use to track the particle dynamics, first in the commonly used linear range, then beyond it.

2.1 . Optical forces

In its simplest form, Lorentz's force describes the effect of an electromagnetic field (\mathbf{E} , \mathbf{B}) on a charge q moving at velocity \mathbf{v} as :

$$\begin{aligned} \mathbf{F}(\mathbf{r}, t) &= q[\mathbf{E}(\mathbf{r}, t) + \mathbf{v}(\mathbf{r}, t) \times \mathbf{B}(\mathbf{r}, t)] \\ &= \int_V [\rho(\mathbf{r}, t)\mathbf{E}(\mathbf{r}, t) + \mathbf{j}(\mathbf{r}, t) \times \mathbf{B}(\mathbf{r}, t)]dV \end{aligned} \quad (2.1)$$

where the second line generalizes the first one by considering a distribution of charges ρ and of currents \mathbf{j} . This equation is at the core of many instrumental developments in particle or charged plasma physics, and explains for example the curved trajectories of charged particles in bubble chambers.

In our case, we will be looking at bigger objects, namely a bulk dielectric (silica) particle. A characteristic of dielectric materials is that an external electric field will move all electrical charges out of their equilibrium position, so that the material exhibits a polarization density \mathbf{P} of induced dipole moments, as pictured in figure 2.1. \mathbf{P} is linked to currents density \mathbf{j} as $\partial\mathbf{P}/\partial t = \mathbf{j}$, and by a conservation law to charges density ρ as $-\nabla \cdot \mathbf{P} = \rho$.

From this, we can rewrite the Lorentz equation as:

$$\mathbf{F}(\mathbf{r}, t) = \int_V [-\mathbf{E}\nabla \cdot \mathbf{P} + \frac{\partial\mathbf{P}}{\partial t} \times \mathbf{B}]dV \quad (2.2)$$

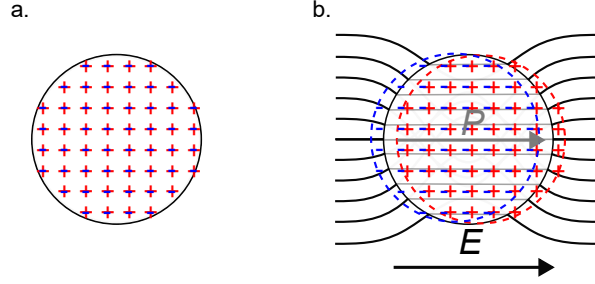


Figure 2.1: Dielectric sphere. a. In the absence of an electric field, negative and positive charges occupy the same position. b. The presence of an electric field \mathbf{E} creates a separation of charges, which reduces the electric field inside the dielectric and induces a polarization density \mathbf{P} .

Carrying the integration, we obtain for $i \in \{x, y, z\}$

$$\mathbf{F}(\mathbf{r}, t) = \int_V [\mathbf{P} \cdot \nabla \mathbf{E} + \frac{\partial \mathbf{P}}{\partial t} \times \mathbf{B}] dV - \int_{dV} (\mathbf{P} E_i) \cdot \mathbf{n} da \quad (2.3)$$

By considering a volume bigger than the particle, we make sure that there are no charges on the surface involved in the second integral, which is thus zero. We then make the hypothesis that the particle is much smaller than the wavelength of the electromagnetic field (which is justified in our case, with $r_{\text{part}} = 75 \text{ nm} \ll \lambda = 1064 \text{ nm}$). It is then legitimate to use the *dipole approximation*: since the field does not vary significantly over the dimensions of the particle, and is assumed homogeneous in its volume, the polarization density can be replaced by a punctual dipole located at the position of the centre of the particle \mathbf{r}_0 , so that $\mathbf{P} = \mathbf{p} \delta(\mathbf{r} - \mathbf{r}_0)$.

The forces acting on the particle are then :

$$\begin{aligned} \mathbf{F} &= (\mathbf{p} \cdot \nabla) \mathbf{E} + \dot{\mathbf{p}} \times \mathbf{B} \\ &= (\mathbf{p} \cdot \nabla) \mathbf{E} + \mathbf{p} \times (\nabla \times \mathbf{E}) + \frac{d}{dt} (\mathbf{p} \times \mathbf{B}) \\ &= \sum_i p_i \nabla E_i + \frac{d}{dt} (\mathbf{p} \times \mathbf{B}) \end{aligned} \quad (2.4)$$

The last term of this equation vanishes if we average over time, so that :

$$\begin{aligned} \langle \mathbf{F} \rangle &= \sum_i \langle p_i(t) \nabla E_i(t) \rangle \\ &= \sum_i \frac{1}{2} \text{Re} \{ \underline{p}_i^*(t) \nabla \underline{E}_i(t) \} \end{aligned} \quad (2.5)$$

where we introduced the complex expressions for p_i and E_i .

We now make the assumption that dipole and field are linked through the

polarizability of the material $\alpha(\omega)$ by the linear relation¹:

$$\underline{\mathbf{p}} = \alpha(\omega)\underline{\mathbf{E}} \quad (2.6)$$

Assuming the particle to be spherical, $\alpha = \alpha' + i\alpha''$ is a complex scalar. The optical forces acting on the particle are then :

$$\langle \mathbf{F} \rangle = \sum_i \frac{\alpha'}{2} \text{Re}\{\underline{\mathbf{E}}_i^* \nabla \underline{\mathbf{E}}_i\} + \sum_i \frac{\alpha''}{2} \text{Im}\{\underline{\mathbf{E}}_i^* \nabla \underline{\mathbf{E}}_i\} \quad (2.7)$$

After some vectorial calculus, we finally obtain :

$$\begin{aligned} \langle \mathbf{F} \rangle &= \frac{\alpha'}{4} \nabla |\mathbf{E}|^2 + \frac{k\alpha''}{\epsilon_0 c} \langle \mathbf{S} \rangle + \frac{ck\alpha''}{2\epsilon_0} \nabla \times \langle \mathbf{L} \rangle \\ &= \mathbf{F}_{\text{grad}} + \mathbf{F}_{\text{scat}} + \mathbf{F}_{\text{curl}} \end{aligned} \quad (2.8)$$

where we have introduced the time-averaged Poynting vector (akin to the energy flux density of the field) $\langle \mathbf{S} \rangle = \frac{1}{2\mu_0} \text{Re}\{\underline{\mathbf{E}} \times \underline{\mathbf{B}}^*\}$ and the time-averaged curl of the spin density of the field $\langle \mathbf{L} \rangle = \frac{\epsilon_0}{4\omega} \text{Im}\{\underline{\mathbf{E}} \times \underline{\mathbf{E}}^*\}$, with c the speed of light in vacuum, $k = \frac{2\pi}{\lambda}$ the wavevector, ϵ_0 the vacuum permittivity, and μ_0 the vacuum magnetic permeability.

Optical forces can then be factored into three components:

- First, the *gradient force* \mathbf{F}_{grad} allows the simplest realization of single-beam optical traps for scales ranging from atoms to μm particles [27]. Indeed, this force derives from a potential U_{opt} such that $\mathbf{F}_{\text{grad}} = -\nabla U_{\text{opt}} \propto -\nabla |\mathbf{E}|^2$, hence its name. Its magnitude depends then essentially on α' and of the gradient of the intensity of the field $I \propto |\mathbf{E}|^2$. This offers a rich playground for generating complex optical potential through an engineering of I , which will be the matter of chapter 4.
- Second, the *scattering force* \mathbf{F}_{scat} is directly proportional to the time-averaged Poynting vector of the laser field and can thus be naively seen as a momentum exchange between incident photons and the particle. It is therefore non-conservative and is also known as the radiation pressure force. While useful for cooling, Ashkin derived what he called an "*optical Earnshaw theorem*" [70], showing that a particle cannot be trapped using only \mathbf{F}_{scat} .
- Finally, \mathbf{F}_{curl} is the *curl force*, and derives from the time-averaged curl of the spin density of the field $\langle \mathbf{L} \rangle$. It is also non-conservative. While orders of magnitude smaller than the other components and thus usually neglected, it is important to take it into account when dealing with anisotropic particles such as dimers and trimers [71, 72].

¹In all generality, α is a tensor of rank 2, depending on the anisotropy of the particle, its material properties, and the field wavelength. For the sake of completeness, for ultra-fast dynamics, equation 2.6 should also include higher order terms, accounting for the nonlinear response of the material to the field variations, which is used in nonlinear optical trapping [69].

To realize an optical tweezer, it is thus crucial that the gradient force is the dominant force. Therefore, we propose to characterize the relative importance of each of the three force components in our experiment. The first step is then to describe the polarizability α and the optical field distribution that controls the optical trap properties.

2.1.1 . Polarizability

For a particle of volume V and complex relative permittivity $\underline{\epsilon}(\omega)$ in a medium of relative permittivity $\underline{\epsilon}_m(\omega)$, electrostatic polarizability is given by the Clausius-Mossotti relation :

$$\alpha_{\text{static}}(\omega) = 3\epsilon_0 V \frac{\underline{\epsilon}(\omega) - \underline{\epsilon}_m(\omega)}{\underline{\epsilon}(\omega) + 2\underline{\epsilon}_m(\omega)} \quad (2.9)$$

This formula needs a correction in the case of an oscillating field. The polarizability depends then both on the incoming field and the particle's scattered field. Its full derivation is obtained by evaluating the scattered field at the centre of a dielectric sphere and linking it to the polarization density \mathbf{P} [73]. The end result gives

$$\alpha(\omega) \approx \alpha_{\text{static}}(\omega) \left[1 - i \frac{k^3}{6\pi\epsilon_0} \alpha_{\text{static}} \right]^{-1}. \quad (2.10)$$

For a transparent particle, such as silica, the static polarizability is at first order real, such that the polarizability can be written:

$$\alpha(\omega) \approx \alpha_{\text{static}}(\omega) + i \frac{k^3}{6\pi\epsilon_0} \alpha_{\text{static}}^2(\omega) \quad (2.11)$$

The imaginary part of this expression is called the *radiative correction*.

We note that this last expression allows drawing a few important conclusions. With $\alpha_{\text{static}} \propto V$, we infer that through α'' , \mathbf{F}_{scat} and \mathbf{F}_{curl} scale quadratically with V , while \mathbf{F}_{grad} scales linearly. This means that for big (μm) particles, \mathbf{F}_{scat} becomes important and must be counterbalanced by other forces (such as a counter-propagating beam), while for nanoscale objects \mathbf{F}_{grad} dominates.

To increase the value of \mathbf{F}_{grad} , we must thus optimize α' and ∇I . While α' is defined by the size of the nanoparticle, the choice of material [74] and wavelength of the trapping laser (through $\underline{\epsilon}(\omega)$), ∇I is often a more amenable parameter.

2.1.2 . Strongly focused beam

To maximize ∇I , a strongly focused optical field is desirable. This is generally done using high numerical aperture (N.A.) objectives.

A description of how strong focusing affects light necessitates to take into account its vectorial nature (*i.e.* polarization). This is done through Richards-Wolf theory [75]. We will just give a flavour of it, and refer the interested reader to the very clear introduction provided for example in [76]. Richards-Wolf theory rests on a few assumptions :

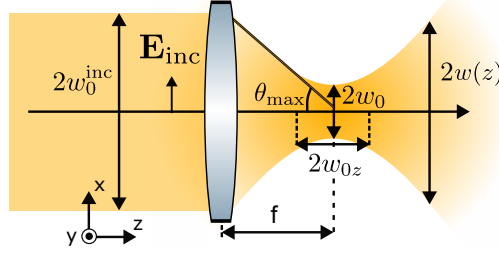


Figure 2.2: Focusing of a Gaussian beam linearly of initial waist w_0^{inc} polarized along x . After the focusing element, the field is constrained to the angular sector defined by the divergence angle θ_{max} , by a new waist w_0 and by the Rayleigh range w_{0z} .

- The refraction of optical rays by an aplanatic optical element of focal length f follows Abbe's *sine condition*, which tells that the distance h between the incident ray and the optical axis is $h = f \sin(\theta)$, where θ is the divergence of the refracted ray.
- The energy flux along each ray is constant, which constitutes the *intensity law*.
- The refracted far-field \mathbf{E}_∞ should be expressed from the incident field \mathbf{E}_{inc} by taking into account how refraction differently affects the perpendicular and parallel components of its polarization.
- Finally and most importantly, the focal field can be linked to the far-field through the *angular spectrum representation* :

$$\mathbf{E}(\rho, \phi, z) = -\frac{ikf e^{-ikf}}{2\pi} \int_0^{\theta_{\text{max}}} \int_0^{2\pi} \mathbf{E}_\infty(\theta, \phi) e^{ikz \cos \theta} e^{ik\rho \sin \theta \cos(\phi-\varphi)} \sin \theta d\phi d\theta \quad (2.12)$$

This expression is called the Debye-Wolf integral. It can be understood as an expression of the field resulting from the interference of all plane waves \mathbf{E}_∞ incoming from a sphere of radius f restricted to the angular sector defined by the numerical aperture (through the divergence angle $\theta_{\text{max}} \approx \sin(\theta_{\text{max}}) = \text{N.A.}/n$).

Until now, all expressions used for the optical forces or for the Debye integral do not make any assumptions over the shape of the incident field \mathbf{E}_{inc} . By finding separable solutions of the Helmholtz equation :

$$(\nabla^2 + k^2)\mathbf{E}(r) = 0 \quad (2.13)$$

it is possible to define different classes of beam geometries [77], such as (non-diffracting) Bessel beams, Airy beams, Laguerre-Gaussian beams... The choice of geometry depends on the intended use of optical trapping (for example, the structure of Bessel beams can be used to sort μm particles [78]).

In this thesis, we will only consider the simplest form, a Gaussian beam, which is the most frequently used approximation of a beam produced by laser sources ².

²keeping in mind that it is nonetheless a non-physical approximation [76, 79]

For a linearly polarized Gaussian beam, the expression of the incoming field at the waist $z \equiv 0$ is:

$$\mathbf{E}_{\text{inc, Gauss}}(x, y, 0) = \mathbf{E}_0 e^{-\frac{x^2+y^2}{w_{0,\text{inc}}^2}} \quad (2.14)$$

with \mathbf{E}_0 a constant vector, and $w_{0,\text{inc}}$ the beam waist. The general expression of this field for any z can be computed using the *angular representation* :

$$\mathbf{E}_{\text{inc, Gauss}}(x, y, 0) = \int_{-\infty}^{+\infty} \int_{-\infty}^{+\infty} \hat{\mathbf{E}}_{\text{inc, Gauss}}(k_x, k_y, 0) e^{i[k_x x + k_y y + k_z z]} dk_x dk_y \quad (2.15)$$

with $\hat{\mathbf{E}}_{\text{inc, Gauss}}(k_x, k_y, 0)$ the Fourier transform of $\mathbf{E}_{\text{inc, Gauss}}$ in the plane $z = 0$. For a field propagating along the z -axis, the paraxial approximation means that the transverse wavenumbers k_x and k_y are small compared to k_z , and thus :

$$k_z = k \sqrt{1 - (k_x^2 + k_y^2)/k^2} \approx k - \frac{k_x^2 + k_y^2}{2k} \quad (2.16)$$

From this comes the textbook equation of a paraxial Gaussian beam (with $\rho = \sqrt{x^2 + y^2}$):

$$\mathbf{E}_{\text{Gauss, parax}}(\rho, z) = \mathbf{E}_0 \frac{w_0}{w(z)} e^{-\frac{\rho^2}{w^2(z)}} e^{i[kz - \eta(z) + k\rho^2/2R(z)]} \quad (2.17)$$

with

$$\begin{aligned} w(z) &= w_0(1 + z^2/w_{0z}^2)^{1/2} && \text{the beam radius} \\ R(z) &= z(1 + w_{0z}^2/z^2) && \text{the wavefront radius} \\ \eta(z) &= \arctan(z/w_{0z}) && \text{the phase correction} \end{aligned}$$

where $w_{0z} = \frac{kw_0^2}{2}$ is the so-called Rayleigh range or diffraction length of the Gaussian beam. These notations are summarized in figure 2.2.

Assuming that the waist of the incident Gaussian beam defined by equation (2.14) coincides with the center of the optical element of focal length f , it can be expressed in spherical coordinates as:

$$\mathbf{E}_{\text{inc, Gauss}}(\theta, \phi) = \mathbf{E}_0 e^{-\frac{f^2 \sin^2 \theta}{w_{0,\text{inc}}^2}} \quad (2.18)$$

From this simple expression, the far field \mathbf{E}_∞ in equation (2.12) can then be deduced, as detailed in [76]. By computing the Debye integral corresponding to realistic experimental parameters, we thus obtain the focal fields, derive \mathbf{F}_{grad} , \mathbf{F}_{scat} and \mathbf{F}_{curl} , and plot their vector flows respectively along the $x = 0$, $y = 0$ and $z = 0$ planes, as presented in figure 2.3

A detailed look at the variations of the intensity along each of the axes is presented in figure 2.4 (blue line). It can be observed that the width of these

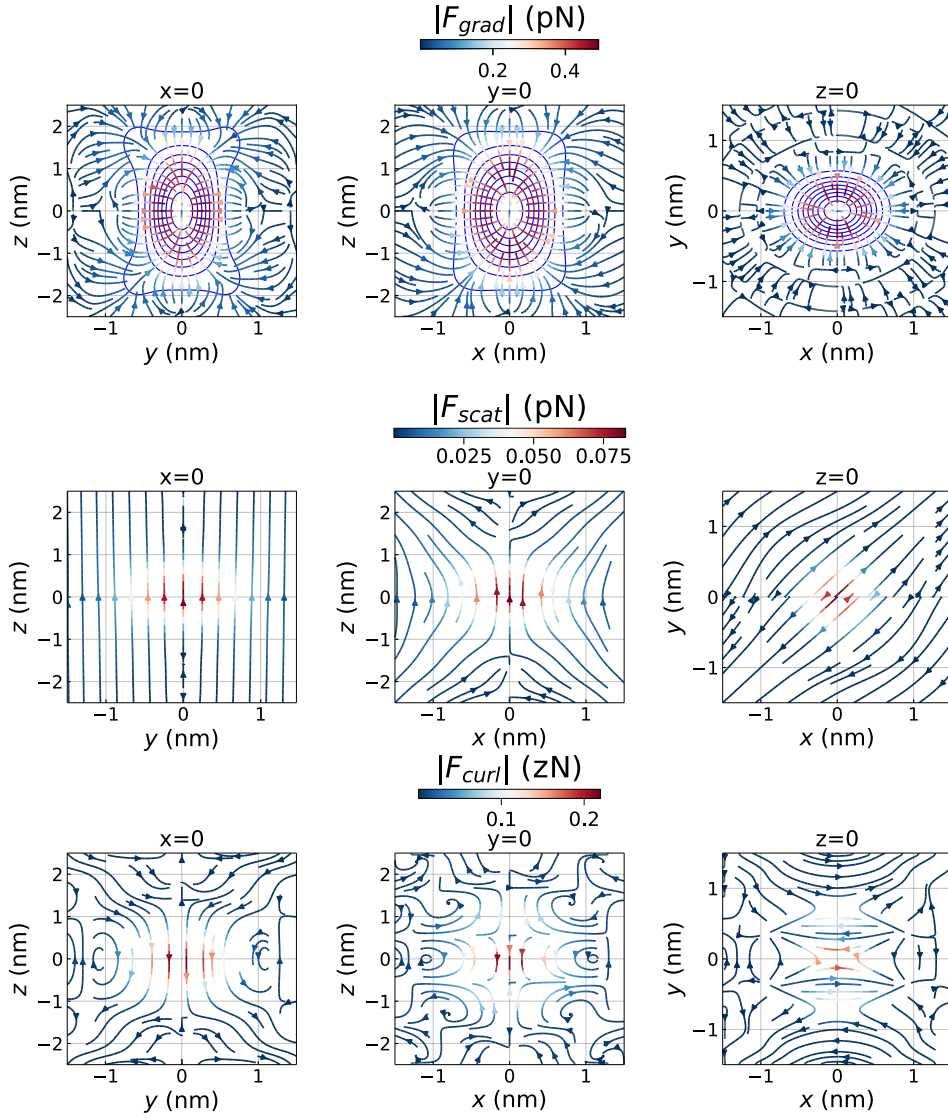


Figure 2.3: Force fields derived from the exact computation of focal fields, performed by taking parameters close to our experimental setup: the field is polarized along x , $\lambda = 1064$ nm, the incident beam waist $w_0 = 2$ mm, $P_{\text{las}} = 100$ mW, $f = 1.8$ mm, N.A. = 0.85. Top: \mathbf{F}_{grad} , the blue contours representing intensity isosurfaces, whose deformations far from focus is a noticeable effect of strong focusing. The field is elongated in the direction of polarisation x . Middle: \mathbf{F}_{scat} . Bottom: \mathbf{F}_{curl} .

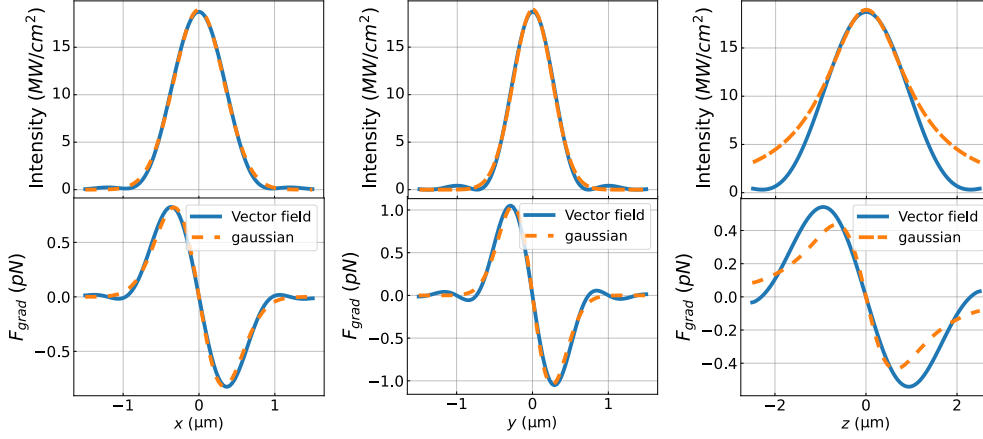


Figure 2.4: Simulation of the field intensity (top), its derivation leading to the force F_{grad} (bottom), represented along x , y and z axes, for the exact computation of the field from equation 2.12. A fit of these curves with the Gaussian approximation of equation 2.19 gives the following parameters : $w_{0x} = 690$ nm, $w_{0y} = 560$ nm, $w_{0z} = 1170$ nm (and thus $w_0 = 630$ nm).

intensity distributions is different. In particular, the distribution along the axis of polarization, x , is broader than along y .

This complete computation provides a good representation of strongly focused fields. However, the complete determination is computationally heavy and does not provide easy access to the values of the optical forces. An alternative is to model these fields by a Gaussian approximation with adapted parameters [80, 81], notably the effective waists w_{0x} and w_{0y} :

$$\mathbf{E}_{\text{focus, approx}}(x, y, z) = \mathbf{E}_0 \frac{w_0}{w(z)} e^{-\left(\frac{x^2}{w_{0x}^2} + \frac{y^2}{w_{0y}^2}\right) \frac{w_0^2}{w(z)^2} + i\phi(x, y, z)} \quad (2.19)$$

where

$$\phi(x, y, z) = kz - \eta(z) + \frac{k(x^2 + y^2)}{2z\left(1 + \frac{w_{0z}^2}{z^2}\right)} \quad (2.20)$$

A fit of the intensities obtained from the previous computation in figure 2.4 with this model provides the values $w_{0x} = 690$ nm, $w_{0y} = 560$ nm, $w_{0z} = 1170$ nm. This will be used in the modelling of the trapping beam in the following of the thesis.

From a Taylor expansion up to order 4, we can then express the trapping

potential in powers of w_{0i} :

$$\begin{aligned}
U_{\text{opt}}(x, y, z) &= -\frac{\alpha'}{4} |\mathbf{E}_{\text{focus, approx}}^2(x, y, z)| = -\frac{\alpha'}{2c\epsilon_0} I_0 \frac{w_0^2}{w(z)^2} e^{-\left(\frac{2x^2}{w_{0x}^2} + \frac{2y^2}{w_{0y}^2}\right) \frac{w_0^2}{w(z)^2}} \\
&\approx -U_0 \left(1 - \left(2\frac{x^2}{w_{0x}^2} + 2\frac{y^2}{w_{0y}^2} + \frac{z^2}{w_{0z}^2}\right)\right. \\
&\quad + \left(2\frac{x^4}{w_{0x}^4} + 2\frac{y^4}{w_{0y}^4} + \frac{z^4}{w_{0z}^4}\right) \\
&\quad \left. + \left(4\frac{x^2y^2}{w_{0x}^2w_{0y}^2} + 4\frac{x^2z^2}{w_{0x}^2w_{0z}^2} + 4\frac{y^2z^2}{w_{0y}^2w_{0z}^2}\right)\right) + \mathcal{O}(x^4 + y^4 + z^4)
\end{aligned} \tag{2.21}$$

with $I_0 = \frac{c\epsilon_0}{2} |E_0|^2$ and $U_0 = \frac{\alpha'}{2c\epsilon_0} I_0$.

The expression of \mathbf{F}_{grad} in the case of a Gaussian beam is thus :

$$\begin{aligned}
\mathbf{F}_{\text{grad}}(x, y, z) &= -\nabla U_{\text{opt}}(x, y, z) \\
&= - \begin{pmatrix} k_x x (1 + \xi_x x^2 + \xi_y y^2 + \xi_z z^2) \\ k_y y (1 + \xi_x x^2 + \xi_y y^2 + \xi_z z^2) \\ k_z z (1 + 2\xi_x x^2 + 2\xi_y y^2 + \xi_z z^2) \end{pmatrix}
\end{aligned} \tag{2.22}$$

with $k_i = I_0 \frac{2\alpha'}{c\epsilon_0 w_{0i}^2}$ for $i \in \{x, y\}$ and $k_z = I_0 \frac{\alpha'}{c\epsilon_0 w_{0z}^2}$, and $\xi_i = -\frac{2}{w_{0i}^2}$.

Hence, to first order, \mathbf{F}_{grad} acts as a restoring force, following in first approximation Hooke's law for a spring of stiffness k_i along each axes. These stiffnesses depends on :

- The real part of the polarizability α' .
- The laser power through I_0 .
- The focusing through w_{0i} .

The ξ_i are called Duffing terms, and are responsible for the nonlinear dynamics of the particle. Their effect becomes preponderant when the oscillations of the particle are of the order of w_{0i} . Duffing terms are frequently encountered in nanomechanical systems [82], and levitated nanoparticles are an excellent testbed to explore and characterize the underlying dynamics [83].

While we will be interested in nonlinearities in chapter 4, they will stem from shaping the potential, and we will not explicitly consider Duffing terms in the following.

Likewise, the expression of \mathbf{F}_{scat} for a Gaussian beam is [84, 85] :

$$\mathbf{F}_{\text{scat}}(x, y, z) = \frac{\alpha''}{\alpha'} k_z \begin{pmatrix} kxz \\ kyz \\ \zeta_0 + \zeta_x x^2 + \zeta_y y^2 + \zeta_z z^2 \end{pmatrix} \tag{2.23}$$

where $\zeta_0 = w_{0z}(w_{0z}k - 1)$, $\zeta_i = (k/2 - 2(w_{0z} - kw_{0z}^2)/w_{0i})$ for $i \in \{x, y\}$ and $\zeta_z = (2 - kw_{0z})/w_{0z}$.

Figure 2.4 shows that \mathbf{F}_{scat} mostly affects the trapping by pushing the particle along the z axis, counteracting \mathbf{F}_{grad} . One can thus define a new equilibrium position z_{eq} for which $\mathbf{F}_{\text{grad}}(0, 0, z_{\text{eq}}) + \mathbf{F}_{\text{scat}}(0, 0, z_{\text{eq}}) = \mathbf{0}$. This leads to first order to :

$$z_{\text{eq}} \approx \frac{\alpha''}{\alpha'} w_{0z} (w_{0z}k - 1) \approx 108 \text{ nm} \quad (2.24)$$

where we used the previously obtained value of w_{0z} . Importantly, the position of the trapping potential along z does not depend on the intensity of the trapping laser, but on the volume of the particle (through α''/α') and the focusing (through w_{0z}).

So, in the following we will account only the gradient force, and will generally use the harmonic approximation described by the first order of equation 2.21.

2.2 . Dynamics of a trapped particle

2.2.1 . Langevin equation

The dynamics of a particle trapped in a harmonic potential generated by the previously introduced Gaussian beam can be described by the Langevin equation :

$$\ddot{\mathbf{r}} + \Gamma \dot{\mathbf{r}} + \frac{\mathbf{F}_{\text{opt}}(r)}{m} = \frac{1}{m} \left[\mathbf{F}_{\text{fluct}}(t) + \sum_i \mathbf{F}_i \right] \quad (2.25)$$

Projected along x , and assuming the harmonic approximation as mentioned before, this equation becomes:

$$\ddot{x} + \Gamma \dot{x} + \Omega_{0x}^2 x = \frac{1}{m} \left[F_{\text{fluct}}^x(t) + \sum_i F_i^x \right] \quad (2.26)$$

where $\Gamma = 2\pi \times \gamma$ is a damping coefficient, $\Omega_{0x} = \sqrt{\frac{k_x}{m}} = 2\pi f_{0x}$ is the oscillation frequency of the particle along the x -axis, and $\mathbf{F}_{\text{fluct}}$ is a random force accounting for the stochastic nature of this Brownian harmonic oscillator, an example of which can be seen on figure 2.5 b. $\sum_i F_i^x$ represents the sum of other forces projected along x , such as gravity, Coulomb forces... While in the present work these forces will be neglected, one attractive point about levitated systems is that they can be designed to detect very weak forces [86, 87].

An important relation, mentioned in chapter 1, links $\mathbf{F}_{\text{fluct}}$ to Γ : the *fluctuation-dissipation* theorem, which states that for a system at thermal equilibrium, it is a delta-correlated function :

$$\langle \mathbf{F}_{\text{fluct}}(t) \mathbf{F}_{\text{fluct}}(t + \tau) \rangle = 2m\Gamma k_B T \delta(\tau) \quad (2.27)$$

the physical meaning of which is that the system does not exhibit memory, *i.e.* the value of $\mathbf{F}_{\text{fluct}}$ at an instant is not determined by its past.

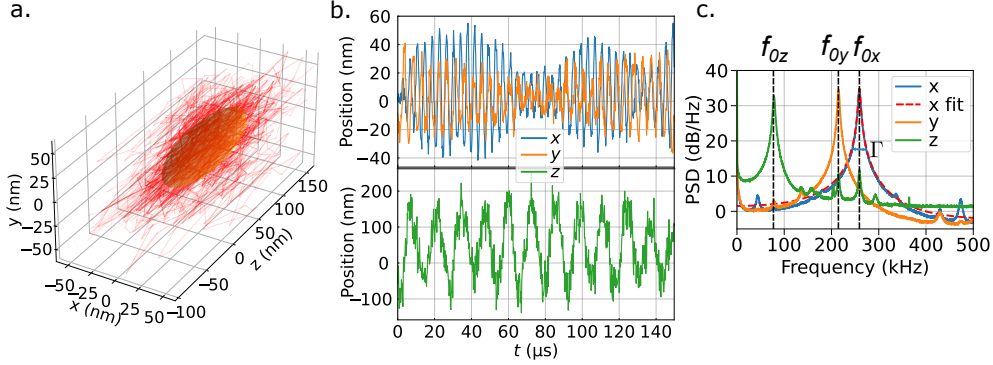


Figure 2.5: Dynamics of a particle trapped in a harmonic potential, at $p_{\text{gas}} = 5$ mbar. a. 3D Brownian dynamics of a particle exploring a 3D harmonic potential. The ellipsoidal volume (orange) can be seen as an equiprobability surface, and is defined by the standard deviations $\sigma_x, \sigma_y, \sigma_z$, which values are 24, 20 and 72 nm, showing an anisotropy that originates directly from the different stiffness along each axis. b. The same dynamics, projected along the 3 axes. The harmonic and stochastic nature of the dynamics is evident, with markedly different amplitudes and frequencies of oscillations for the 3 axes. c. Power density spectra of the 3 axes, showing the profile described by equation 2.33, peaked at the resonant frequencies f_{0x}, f_{0y} and f_{0z} . From a fit, the full width at half maximum directly gives access to the damping $\Gamma/2\pi \approx 4.4$ kHz, which is far smaller than $f_{0x} = 259$ kHz, $f_{0y} = 215$ kHz and $f_{0z} = 78.5$ kHz, thus confirming that we are well in the underdamped regime.

In all generality, the damping term Γ is related to various physical processes. While levitated experiments are immune to most damping phenomena encountered in clamped systems such as cantilevers or membranes [82], they are affected as well by photon recoil at high vacuum [88]. Here, we consider only the damping induced by gas collisions, which is the dominant process for our experiments. The damping can in this case be derived from classical theory. It depends on the particle shape [89, 90], and for a sphere it writes [91] :

$$\Gamma_{\text{gas}} \approx \frac{6\pi\eta r_{\text{part}}}{m} \frac{0.619}{0.619 + \text{Kn}} (1 + c_k) \stackrel{\text{Kn} \gg 1}{\approx} \frac{6\pi\eta r_{\text{part}}}{m} \frac{0.619}{\text{Kn}} \quad (2.28)$$

where $\eta = 18.27 \times 10^{-6}$ Pa·s is the viscosity of air and $\text{Kn} = l/r_{\text{part}}$ with l being the mean free path of a gas molecule is the Knudsen number, and $c_k = 0.31\text{Kn}/(0.785 + 1.152\text{Kn} + \text{Kn}^2)$. This expression indicates that the radius of the particle r_{part} can be obtained by simply measuring Γ , a property that will come in handy for the calibration procedure presented further in this chapter.

Typical time traces of the particle dynamics in a simple optical trap recorded at a pressure of $p_{\text{gas}} = 5$ mbar are shown in figure 2.5 b³. These dynamics are completely related to the Langevin equation 2.26. We see the oscillating motion,

³Experimental details on the trapping and measurement will be discussed in section 2.3

with the characteristic frequency $f_{0i} = \Omega_{0i}/2\pi$, along the three axes $i \in \{x, y, z\}$, corresponding to an underdamped harmonic oscillator. The Brownian nature of the motion and the role played by the damping Γ is highlighted by the evolution of the oscillation amplitude on a typical timescale $t_v = 1/\gamma \approx 46 \mu\text{s}$. Note that the natural frequencies of these oscillators also change on a similar timescale, even if it is hardly noticeable here. The direct recording of time traces provides interesting insights into the particle dynamics, but it is hardly directly usable for extracting qualitative information. To go further, it is thus critical to use data analysis tools. In the following, we will focus on two approaches : the spectral distribution and the equilibrium probability distribution.

2.2.2 . Response function and Power spectral distribution

When looking at a dynamical system, it is often a good idea to study its response function χ or its power spectral density (PSD) $S(\Omega)$, which are in our experiments less sensitive to low frequency noise such as thermal drifts.

By taking its Fourier transform, the Langevin equation 2.26 can be rewritten in the spectral domain as :

$$\begin{aligned}\tilde{x}(\Omega)m[-\Omega^2 - i\Gamma\Omega + \Omega_0^2] &= \tilde{F}_{\text{fluct}}(\Omega) \\ \tilde{x}(\Omega)\chi(\Omega)^{-1} &= \tilde{F}_{\text{fluct}}(\Omega)\end{aligned}\quad (2.29)$$

where $\hat{x}(\Omega)$ is the Fourier transform of x and $\chi(\Omega) = \chi'(\Omega) + i\chi''(\Omega)$ is the response function of the system. This last function can be defined by its reactive part :

$$\chi'(\Omega) = \frac{1}{m} \frac{\Omega_0^2 - \Omega^2}{(\Omega_0^2 - \Omega^2)^2 + \Gamma^2\Omega^2} \quad (2.30)$$

and its dissipative part :

$$\chi''(\Omega) = \frac{1}{m} \frac{\Gamma\Omega}{(\Omega_0^2 - \Omega^2)^2 + \Gamma^2\Omega^2} = m\Gamma\Omega|\chi(\Omega)|^2 \quad (2.31)$$

The poles of $\chi(\Omega)$ are $\Omega^\pm = -i\Gamma/2 \pm \sqrt{\Omega_0^2 - \Gamma^2/4}$. They define two regimes:

- For $\Omega_0 > \Gamma/2$, the poles have real and imaginary parts : this is the **under-damped** regime
- For $\Omega_0 < \Gamma/2$, the poles have only an imaginary part : this is the **over-damped** regime

We will come back to the differences between these two regimes in chapter 3.

The PSD :

$$\begin{aligned}\text{PSD}_{xx}(\Omega) &= \langle |\hat{x}(\Omega)|^2 \rangle \\ &= \langle |\tilde{F}_{\text{fluct}}(\Omega)|^2 |\chi(\Omega)|^2 \rangle\end{aligned}\quad (2.32)$$

is then directly obtained by using the fluctuation-dissipation theorem as :

$$\begin{aligned} \text{PSD}_{xx}(\Omega) &= \frac{2m\Gamma k_B T}{2\pi} \frac{\chi''(\Omega)}{m\Gamma\Omega} \\ &= \frac{A}{\pi} \frac{\Gamma\Omega_0^2}{(\Omega_0^2 - \Omega^2)^2 + \Gamma^2\Omega^2} \end{aligned} \quad (2.33)$$

where $A = \frac{k_B T}{m\Omega_0^2} = \langle x^2(t) \rangle$ is the area under the PSD.

In the rest of this thesis, we use this expression to fit experimental PSD computed from acquired signals time traces⁴, and extract the parameters Ω_0 , A and Γ . An example of the procedure is shown in figure 2.5 c.

2.2.3 . Equilibrium probability distribution and Fokker-Planck equation

While the Langevin equation describes the dynamics of a trapped Brownian particle, it is often of interest to use the instruments of probability theory.

At thermal equilibrium, the equilibrium probability density of a trapped Brownian particle is given by the *Maxwell-Boltzmann* distribution

$$\rho(\mathbf{q}, \mathbf{p}) = \rho_0 e^{-\frac{U(\mathbf{q}) + \frac{1}{2}m\mathbf{p}^2}{k_B T}} \quad (2.34)$$

where $\mathbf{q} = (x, y, z)$ and $\mathbf{p} = (\dot{x}, \dot{y}, \dot{z})$ are respectively the position and momentum vectors.

At equilibrium, \mathbf{q} and \mathbf{p} are uncorrelated. This property is directly observable on figure 2.6, where $\rho(x, v_x)$ is represented. The contours representing isosurfaces of $\rho(x, v_x)$ are ellipses whose principal axes are oriented along the figure axes, which means that there is no cross-terms xv_x in its definition. Hence, the density of probabilities $\rho(\mathbf{q})$ and $\rho(\mathbf{p})$ are separable and in particular

$$\rho(\mathbf{q}) = \rho_{q,0} e^{-\frac{U(\mathbf{q})}{k_B T}} \quad (2.35)$$

Under the assumption that x , y and z are also uncorrelated, we can further separate their respective distributions to obtain :

$$\rho(x) = \rho_{x,0} e^{-\frac{U(x)}{k_B T}} \quad (2.36)$$

By taking the logarithm of this expression, we can thus obtain the shape of the potential along x in units of $k_B T$.

Experimentally, we obtain an approximation of ρ by computing histograms from time traces. For a precise description of ρ , its moments can be computed as:

$$\mu_i = \int_{-\infty}^{\infty} x^i \rho(x) dx \quad (2.37)$$

⁴we use the `psd` routines from the *Matplotlib* Python library

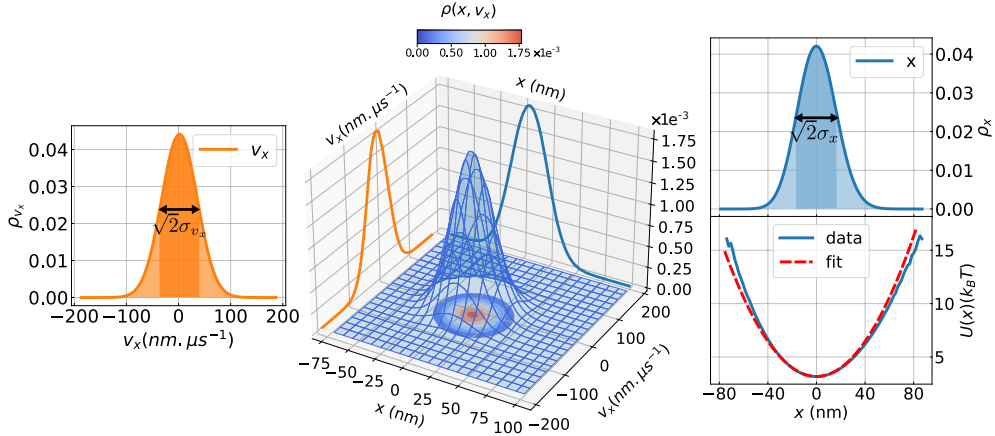


Figure 2.6: Probability density function $\rho(x, v_x)$, computed from the experimental time traces presented in figure 2.5. x and v_x being uncorrelated, $\rho(x, v_x)$ is separable into the marginal distributions ρ_x and ρ_{v_x} . Both have a Gaussian profile, the area under $\sqrt{2}\sigma_x$ (resp. $\sqrt{2}\sigma_{v_x}$) representing 68% of the total as expected. By taking the logarithm of $\rho_x(x)$, we obtain $U(x)$ in units of $k_B T$. A fit of this harmonic potential gives a very good approximation of k_{trap} compared to the value obtained from the expression $m\Omega_{0x}^2$ (16.9 vs 17.0×10^{-3} pN/nm).

A Gaussian distribution is entirely determined by its two first moments⁵. To study a distribution, one usually look at the following four quantities which can be derived from the moments :

- The *mean* $\langle X \rangle = \mu_1$.
- The *variance* $\sigma_{xx} = \langle (X - \langle X \rangle)^2 \rangle = \langle X^2 \rangle - \langle X \rangle^2 = \mu_2 - \mu_1^2$, or alternatively the standard deviation $\sigma_x = \sqrt{\sigma_{xx}}$, which characterizes the *width* of the distribution. For a Brownian harmonic oscillator, the *equipartition theorem* leads to $\sigma_x = \sqrt{\frac{k_B T}{k_x}}$ (the same being true for σ_y and σ_z). The different stiffnesses explain the elongated shape of the volume explored by the particle visible in figure 2.5 a. .
- The *skewness* $\gamma_1 = \langle \left(\frac{X - \langle X \rangle}{\sigma_x} \right)^3 \rangle = \frac{\mu_3 - 3\mu_1\mu_2 + 2\mu_1^3}{(\mu_2 - \mu_1^2)^{3/2}}$, which relates to the asymmetry of a distribution⁶.
- The *kurtosis* $\kappa = \langle \left(\frac{X - \langle X \rangle}{\sigma_x} \right)^4 \rangle = \frac{\mu_4 - 3\mu_2^2 + 12\mu_2\mu_1^2 - 4\mu_1\mu_3 - 6\mu_1^4}{(\mu_2 - \mu_1^2)^2}$. A large class of processes, especially in biology or financial-market modeling, follow non-

⁵The *moment problem*, which asks if the sequence of all moments is sufficient to characterize uniquely a distribution of probability, has been the subject of intense work in mathematics for over a century [92]. In most physically relevant cases yet, we consider that the knowledge of moments encodes the information relative to the distribution.

⁶As a cultural note, simulating highly skewed distributions is a challenging task [93].

Gaussian diffusions and have "fat-tailed" distributions. They can be efficiently characterized by computing their kurtosis [94].

While most of current work in stochastic thermodynamics is done by considering the mean and variance of distributions, recent propositions regarding first passage times emphasize the importance of looking at skewness and kurtosis [95], in particular with respect to statistical kinetics.

As noted in [96], moments can be used to derive a Taylor expansion of the transformation of a random variable X by a nonlinear function h (in chapter 4, we will consider for h the nonlinear measurement function of our system). In turn, the mean and (co)variance of $h(X)$ can thus be expressed by functions of the moments of X multiplied by derivatives of h computed at $\langle X \rangle$. This highlights the pertinence of considering moments, and is the basis of the Unscented Kalman Filter presented in the chapter 4.

For distributions which can be fully described by their first two moments, such as a Gaussian distribution, their time evolution is described by the Fokker-Planck equation. In the case of a freely diffusing Brownian particle, its expression is :

$$\frac{\partial \rho}{\partial t} = \Gamma \frac{\partial [v\rho]}{\partial v} + \Gamma \frac{k_B T}{m} \frac{\partial^2 \rho}{\partial v^2} \quad (2.38)$$

the first term corresponding to a *drift* and the second to a *diffusion* of the probability distribution.

For a particle trapped in a 1D-potential $U(x)$, the Fokker-Planck equation can be modified to take into account the effect of the gradient force $F_{\text{grad}}(x) = -\frac{\partial U_{\text{opt}}(x)}{\partial x} = -m\Omega_0^2 x^2$. From [97], we obtain the Kramers-Klein equation :

$$\frac{\partial \rho}{\partial t} + v \frac{\partial \rho}{\partial x} - \frac{1}{m} \frac{\partial U_{\text{opt}}(x)}{\partial x} \frac{\partial \rho}{\partial v} = \Gamma \frac{\partial [v\rho]}{\partial v} + \Gamma \frac{k_B T}{m} \frac{\partial^2 \rho}{\partial v^2} \quad (2.39)$$

of which a solution at equilibrium is the Maxwell-Boltzmann distribution.

This expression is mainly used in chapter 3 for the derivation of thermodynamics protocols.

2.3 . Experimental setup

From the simulation of the optical forces presented in section 2.1, we concluded that we needed to use a strongly focused and powerful laser beam. Moreover, to study non-equilibrium physics as introduced in chapter 1, we need to be able to finely control the coupling of a levitated particle to its environment. The linear response introduced in subsection 2.2.2 allows characterizing two regimes of coupling, namely the overdamped and underdamped regimes, which depends on the relative values of Γ and Ω_0 , the latter being directly related to the stiffness of the trapping potential k_{trap} .

Of these two knobs, we use Γ to control the coupling, and keep k_{trap} as our parameter to define a thermal state. Indeed, we introduced in subsection 2.2.3 the tools of statistical physics, and saw that an equilibrium state is linked through the Maxwell-Boltzmann distribution to the trapping potential. If we want to study state-to-state transformations, we thus need to be able to control the shape of the potential.

We first show how we control the trapping laser position and power through an acousto-optic modulator, before presenting our experimental setup in more details.

2.3.1 . Control of the trapping potential

In our experiments, we control the trapping beam with an acousto-optic modulator (AOM). As described in figure 2.7, we first generate a sinusoidal RF signal (around 110 MHz) from an arbitrary waveform generator (AWG). This signal is then amplified through a high RF power amplifier.

This drives a piezoelectric transducer which in turn generates an acoustic wave in a TeO_2 crystalline lattice. The interaction between this acoustic wave and a laser beam can be described as a photon-phonon scattering process. Through the conservation of energy and momentum, the scattered photon frequency and wave vector is given by:

$$\begin{aligned}\omega_s &= \omega_i + \Omega_a \\ k_s &= k_i + K_a\end{aligned}\tag{2.40}$$

where Ω_a and K_a are the frequency and wave vector of the acoustic wave, ω_i and k_i those of the incident beam, and ω_s and k_s those of the scattered beam. The Bragg's condition then gives:

$$\theta_{\text{Bragg}} \approx \sin(\theta_{\text{Bragg}}) = l \frac{K_a}{2k_i} = l \frac{\lambda}{2n\Lambda_a}\tag{2.41}$$

where λ is the wavelength of the laser beam, n the refractive index of the crystal, $\Lambda_a = v/f_{\text{AWG}}$ is the acoustic wave wavelength, v is the velocity of sound in the crystal (for TeO_2 , $v = 4200 \text{ m}\cdot\text{s}^{-1}$), and l is the diffraction order. In our experiment, we use the +1 order.

An acousto-optic modulator enables to control the intensity of the diffracted beam as well, by tuning the power of the driving acoustic wave, which is done by changing the amplitude V_{AWG} of the RF signal. The diffraction efficiency relates the power diffracted in the first order to the power of the incident beam, and is given by [98] :

$$\frac{P_{\text{las},1}}{P_{\text{las}}} = \sin^2(\sqrt{\eta(V_{\text{AWG}})})\tag{2.42}$$

where η is a function of the acoustic power in the AOM and thus depends quadratically on V_{AWG} , and on the piezoelectric transducer and crystal geometries.

For a given orientation, by slightly changing f_{AWG} , it is possible to control the angle of deflection of the beam. From the supplier data, a variation $\delta f_{\text{AWG}} =$

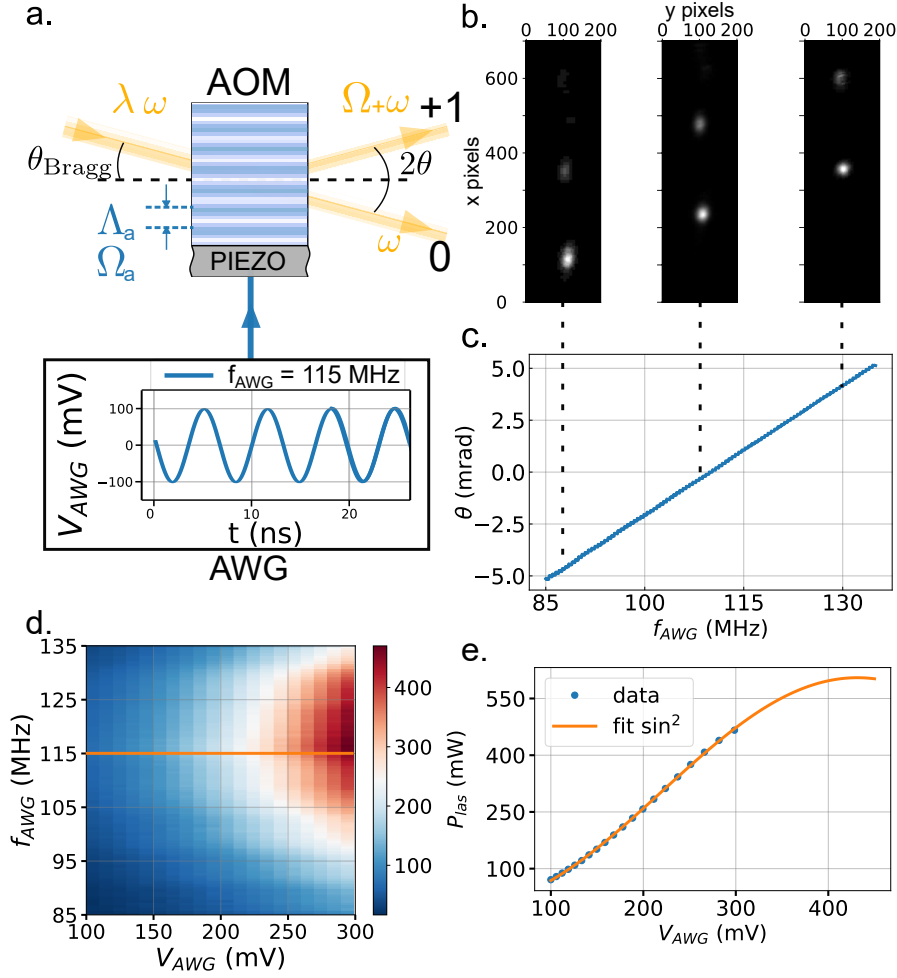


Figure 2.7: a. Bragg diffraction of an incident laser beam of wavelength λ and frequency ω by an AOM. The AOM is driven by a sinusoidal waveform of amplitude V_{AWG} and frequency f_{AWG} using an arbitrary waveform generator (AWG). The incident beam is diffracted, the 1st order (+1) being frequency (blue) shifted by $\Omega_a = 2\pi \times f_{AWG}$, and deflected by an angle $2\theta_{\text{Bragg}}$ from the non-diffracted zero order.

b. The deflection angle can be steered by slightly varying the driving frequency f_{AWG} . This is observed by beam sampling a fraction of the diffracted beam and imaging its motion on a camera (b.). On these frames, one can remark the presence of a bright spot corresponding to the first order, and another corresponding to the second order. On each frame, we fit the brightest spot by a 2D Gaussian to extract the position and intensity of the beam.

c. From its position on the camera, we deduce the deviation angle θ of the beam. As expected from Bragg's law 2.41, θ depends linearly on the driving frequency f_{AWG} , with $\delta\theta \approx 200 \mu\text{rad}$ for 1 MHz.

d. The heat map resulting from the fitting procedure, showing the variations of the diffraction efficiency with f_{AWG} and V_{AWG} , with a maximum located around 117 MHz.

e. A cut of the heat map for $f_{AWG} = 115$ MHz, showing the typical $\sin^2(\frac{V_{AWG}}{\sqrt{\eta_0}} + \phi_0)$ dependency to the driving amplitude V_{AWG} , where η_0 accounts for the other parameters in the definition of $\eta(V_{AWG})$ used in equation 2.42. While we can remark that we could in theory have driven at higher amplitudes to reach the plateau in efficiency at 400 mV, the limits on driving power settled by the supplier of the AOM did not recommend it.

1 MHz corresponds to a change $\delta\theta \approx 200 \mu\text{rad}$. We use this to control the position of a beam along x , which can be directly monitored with a camera, as presented in figure 2.7 b. In turn, it also modifies the diffraction efficiency described by equation 2.42, as can be observed on figure 2.7 d. The modified expression can be found in [98].

From this first characterization, we decided to align our setup to work by default with the first order beam diffracted for $f_{\text{AWG}} = 115 \text{ MHz}$.

2.3.2 . General description

The AOM is thus integrated in the complete setup we use to perform optical trapping, and that is presented in figure 2.8.

With it, we can :

- Control the damping Γ of the levitated particle, by controlling the pressure in the *vacuum chamber* containing the trapping apparatus, Γ being linearly dependant of p_{gas} , as shown in figure 2.9 a. and supported by equation (2.28). We conducted experiments from atmospheric pressure (1 bar, where $\Gamma \gg \Omega_0$) to moderate vacuum (a few millibars, where $\Gamma \ll \Omega_0$), thus exploring both the overdamped and underdamped regimes.
- Control the trap stiffness k_{trap} of the trapping potential, by controlling the power of the trapping beam through the (AOM), as explained in the previous subsection. Once a particle is trapped, we can performed a more thorough characterization of the dependency of k_{trap} with P_{las} . In figure 2.9 b., we verify its linear dependency, as expected from the derivations obtained in section 2.1.
- Control the trap position, as explained in the previous subsection, and eventually generate combinations of trapping beams, by changing the waveform driving the AOM (see chapter 4).

Throughout our experiments, in particular for the realisation of arbitrarily shaped potentials detailed in chapter 4, we need to be able to move a trap over the focus of the microscope objective. Two conditions should be ensured :

- The displacement of the trap in the focal plane of the objective should be controlled only by a variation of the angle of incidence of the beam on its back aperture.
- The back aperture of the objective should always be equally overfilled, so as not to generate unwanted variations of intensity (typically created by lateral displacements of the beam).

These conditions are satisfied by using a 4f-telecentric telescope made of two lenses L1 and L2, as detailed in figure 2.10.

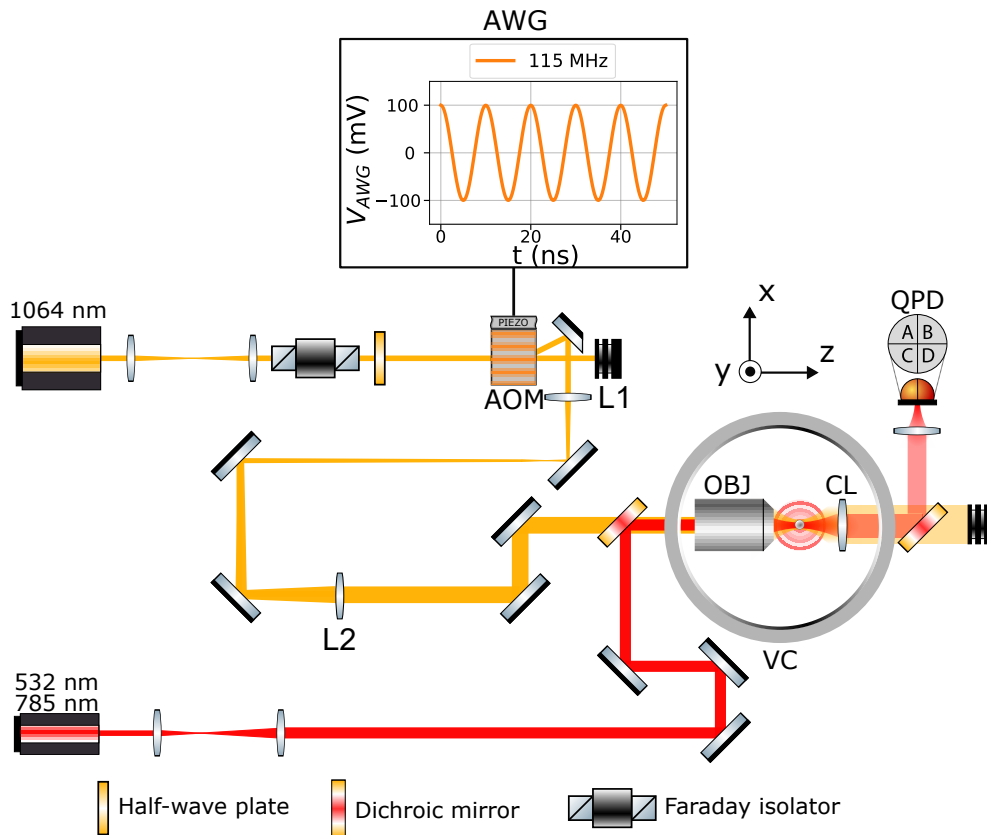


Figure 2.8: Nanoparticle levitation setup.

Trapping : A strong IR laser (Coherent Mephisto MOPA 8W in chapter 3, Azurlight 10 W in chapter 4) is first collimated, then directed to an acousto-optic modulator (AOM, AAOpto MT110-A1.5-IR). The AOM is driven by sine-waves at frequencies f_{AWG} (centered around 115 MHz, which is the frequency of maximal diffraction efficiency of the AOM) and amplitudes V_{AWG} (comprised between 0 and 300 mV) generated by an arbitrary waveform generator (AWG, Spectrum M4i.6621-x8) and amplified (not pictured, Mini-Circuits ZHL-03-5WF+). The first order diffracted beam then passes through a double-telecentric system, used to magnify the beam by a factor 3.75 and most importantly to conjugate the diffraction plane of the AOM to the back focal plane of the microscope objective (OBJ, plan achromat Olympus LCPLN100XIR, NA=0.85). The objective and the particle are placed in a vacuum chamber, which allows to control the surrounding gas pressure.

Measurement : A weak visible laser (Novanta Photonics gem $\lambda_{meas} = 532$ nm for chapter 3, Toptica iBeam Smart $\lambda_{meas} = 785$ nm for chapter 4) is used to measure the dynamics of the particle. The superposition of the field scattered by the particle and the unaffected part of the beam are then collimated by an aspheric collection lens (CL, Thorlabs AL1210, NA=0.55) and directed towards a quadrant photodiode (QPD, Hamamatsu S4349), whose signal is then sent to a digital oscilloscope (not pictured, Picoscope 4824A).

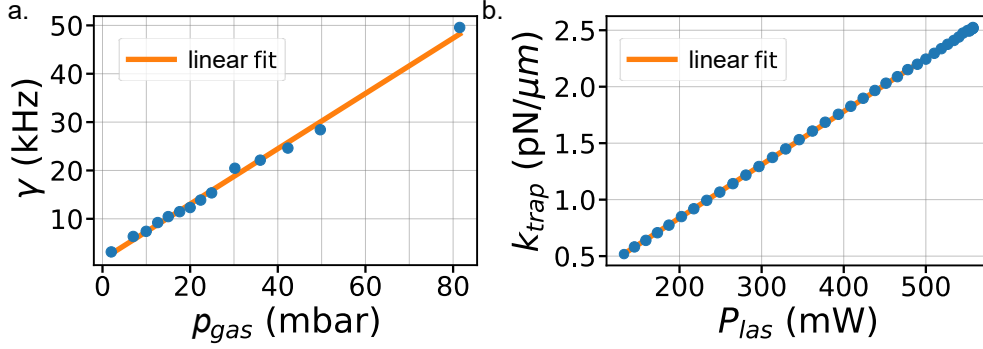


Figure 2.9: Calibrations of our system for $\gamma = \Gamma/2\pi$ (a.) and $k_{\text{trap}} = m\Omega_0^2$ (b.), obtained by acquiring time traces and fitting their PSD with the formula 2.33. In our case, Γ depends linearly on p_{gas} , which is valid as long as we are over the mbar. For high vacuum, nonlinearities and photon recoil must be taken into account as explained in [80, 88], and a better way to measure γ is to perform relaxation experiments [99, 87], as we will show in chapter 3.

The system is first aligned along the 1st order beam diffracted by the AOM driven at $f_{\text{AWG},0} = 115$ MHz. From this reference, the angle of deflection θ_1 is generated by driving the AOM at different frequencies, mostly within a ± 5 MHz range from the reference. From Bragg's law (2.41), we obtained the following relation between the driving frequency f_{AWG} and the deflection angle θ_1 :

$$\theta_1 = \frac{(f_{\text{AWG}} - f_{\text{AWG},0})\lambda}{2nv} \quad (2.43)$$

where v is the acoustic velocity in the AOM crystal ($4200 \text{ m}\cdot\text{s}^{-1}$ for TeO_2), and $n(\lambda)$ is the refractive index of TeO_2). After passing through the telescope, the beam diameter is magnified by a factor f_{L2}/f_{L1} , while its angle to the optical axis is given by :

$$\theta'_1 = \theta_1 \frac{f_{L1}}{f_{L2}} \quad (2.44)$$

Finally, the displacement in the microscope objective focal plane is given by the sine law :

$$x_1 = \theta'_1 f_{\text{obj}} = \theta_1 \frac{f_{L1}}{f_{L2}} f_{\text{obj}} \quad (2.45)$$

with f_{L1} and f_{L2} the focal lengths of the double telecentric system used to conjugate the diffracting plane of the AOM to the pupil of the objective.

From the experimental parameters given in figure 2.10, we expect a steering of the trap displacement by

$$\frac{\Delta x_{\text{trap}}}{\Delta f_{\text{AWG}}} \approx 96 \text{ nm} \cdot \text{MHz}^{-1}. \quad (2.46)$$

Thus, the range of motion of the trap over the whole frequency range of the AOM is around $5 \mu\text{m}$. In practice, we mostly limit our experiment to $\pm 0.5 \mu\text{m}$ on each

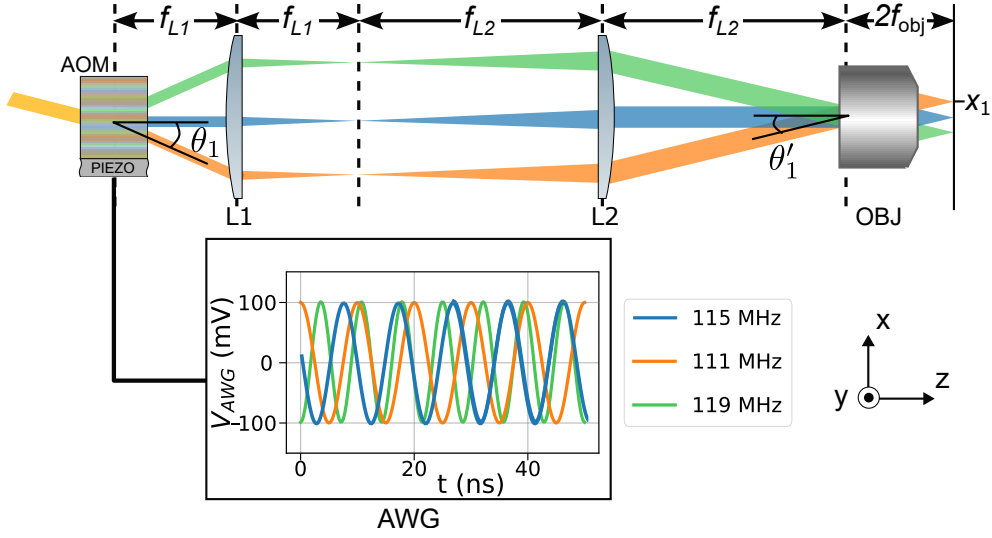


Figure 2.10: Beam steering through a telecentric 4f telescope. The diffracting plane of the AOM is placed at the focus of the first lens L1, which is separated from L2 by $f_{L1} + f_{L2}$, and the objective back aperture is then placed at the focus of the second lens L2. The beam impinging on the AOM being only 0.9 mm in diameter, it needs to be expanded to overfill the microscope objective aperture (insufficient overfilling leading to bad trapping). The pupil diameter of the objective being $2N.A. \cdot f_{obj}$, with $f_{obj} = 1.8$ mm, we obtain a diameter of 3 mm, which means that we must at least expand the beam by a factor 3. This is done by a 4f-telescope, with $f_{L1} = 200$ mm and $f_{L2} = 750$ mm. The telecentricity of this setup is needed to assure that by changing the driving frequency of the AOM and thus its deflecting angle by θ_1 , we linearly displace the trapping beam by x_1 in the focal plane of the objective, without impacting the trapping power. Moreover, whatever its position along the x axis, the trapping beam should always fall perpendicularly to the objective focal plane, so as not to develop asymmetries in the trapping potential.

side of the central position corresponding to $f_{AWG} = 115 \pm 5$ MHz, since we cannot detect the particle beyond this with the static measurement beam.

Beyond the calibration of the AOM presented in figure 2.7, what we are interested in is the exact laser power at the focus, and its position. We thus compute the calibration map presented in figure 2.11.a. It represents the evolution of the frequency of oscillation along x of a particle trapped in a potential generated by (f_{AWG}, V_{AWG}) , which is far more accurate than the camera measurement. As in this previous calibration, a maximum efficiency of diffraction by the AOM is observed at 115 MHz, and decreases while moving to the edges. The calibration is performed in a range $V_{AWG} \in [80, 210]$ mV, the lower limit being set by the frequent lost of particles below this, and the upper limit by the maximum admissible power of the AOM.

With it, we can estimate the real displacement of the trap. For each trace acquired for a given driving f_{AWG} , we compute the calibration factor $c_{xx} = \frac{\partial S_x}{\partial x}$

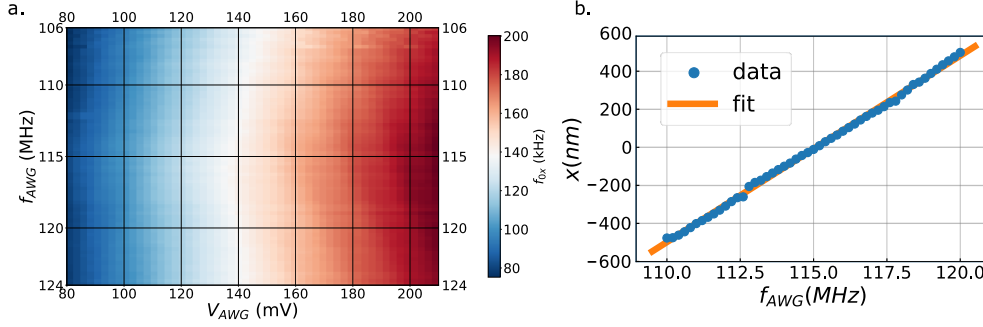


Figure 2.11: Calibration procedure. a. We record the dynamics of the trapped particle while moving the trap position through changing f_{AWG} , as well as its stiffness through V_{AWG} . From the PSD obtained from each measurement, we obtain f_{0x} , as well as c_{xx} . b. We use c_{xx} to estimate the displacement of the trap for a given f_{AWG} . A linear fit gives a mean displacement of 98 nm for an increase of f_{AWG} by 1 MHz, which is close to the 100 nm computed from the system parameters $\delta\theta, f_{L1}, f_{L2}$ and f_{obj} .

that links the measured signal S_x to the actual particle displacement x ⁷, as well as the mean value of the signal $\langle S_x \rangle$.

Thus, for a small change in the driving frequency df_{AWG} , the change in the particle position can then be deduced as:

$$dx = \frac{1}{c_{xx}(f_{\text{AWG}})} \frac{\partial \langle S_x \rangle (f_{\text{AWG}})}{\partial f_{\text{AWG}}} df_{\text{AWG}} \quad (2.47)$$

All values from the right member are computable from the calibration. By taking the cumulative sum of these values, we can then plot the position x as a function of f_{AWG} , as presented in figure 2.11.b. We finally found that experimentally

$$\left(\frac{\Delta x_{\text{trap}}}{\Delta f_{\text{AWG}}} \right)_{\text{exp}} \approx 98 \text{ nm} \cdot \text{MHz}^{-1}, \quad (2.48)$$

in excellent agreement with the expectation from equation (2.46).

A last remark on the use of AOM concerns the experimental issues encountered when changing quickly the driving amplitude V_{AWG} . Under such a sudden change we may observe a time dependent variation in the trapping beam divergence, that lead to a change on the trap position mostly along the z optical axis. This effect is underlined in figure 2.12, where we performed measurements of the beam divergence and steady state particle displacement along the z axis for different RF powers. We ascribe this effect to thermal lensing, induced in the TeO_2 crystal of

⁷details on the procedure to compute this calibration factor c_{xx} is given in section 2.4.2

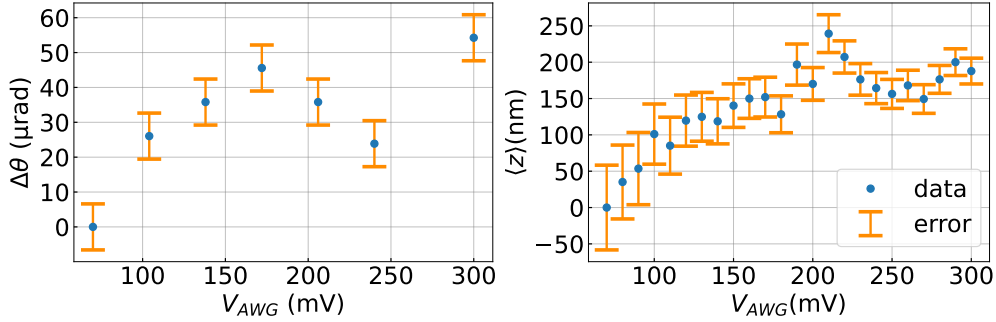


Figure 2.12: Left : Variations of the divergence θ of a laser beam diffracted by an AOM for different RF powers. Right : the corresponding effect on the position along the z axis of a levitated particle. The behaviour is broadly the same, the variation of the divergence translating in a displacement of the waist after the microscope objective.

the AOM by a variation of the gradient of temperature generated by the ramping of RF power ⁸.

This effect especially impacted the first experiments done in the context of the study of the particle relaxation to equilibrium after a change in the trapping stiffness (see. chapter 3). Indeed, our measurements being done with an auxiliary beam, which is not affected by this motion, the measured distributions were biased, making the interpretation of data complex.

Note that similar effects have been observed in other systems [101, 102], and solved by thermal control [103] or by performing a double-pass in the AOM [104]. While being very attractive, this last solution appeared to be not reasonably practicable with many diffracted beams.

Fortunately, we manage to solve this issue by a careful alignment of the trapping and measuring beams, limiting the impact on our measurements by one order of magnitude, which was sufficient to not bias the measured distributions.

2.4 . Measurements and (linear) calibration

To detect the position of the particle, we use an interferometric measurement. The particle is illuminated by a fixed measuring laser, producing a scattered field E_s that interferes with the incident field E_i . Here, we only consider the field scattered in the forward direction due to the simplicity of a common path interferometer, when a more efficient detection procedure (especially along the z axis) would use the backward scattered field [105]. Figure 2.13 illustrates our experimental configuration. The intensity of the interference pattern created on a detector

⁸The poor thermal conductivity and anisotropic thermal expansion of TeO_2 spur the research for other acousto-optic materials such as TiTe_3O_8 [100]

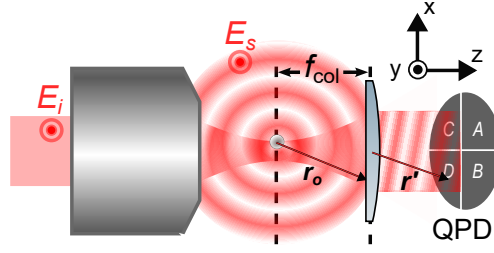


Figure 2.13: Position detection of a scattering dipole in a focused beam. Placed in the incident field E_i , polarized along y , the particle acquires a dipole moment $p = \alpha E_i$ and radiates the field E_s , whose far field component $\mathbf{G}(R)\mathbf{p}$ has a spherical geometry. These two fields are then recollimated by the collection lens L_{col} . Crucially, a transverse displacement of the particle induces a tilt of E_s after the collection lens. The resulting phase difference between the two fields is then measured by the QPD, by combining the signal on its four quadrants: $A+C-(B+D)$ for S_x , $A+B-(C+D)$ for S_y , and all quadrants for S_z (minus a reference taken before the microscope objective).

placed at r' by a particle located in q is given by :

$$\begin{aligned} I(r', q) &= \frac{c\epsilon_0}{2} |E_i(r') + E_s(r', q)|^2 \\ &= \frac{c\epsilon_0}{2} |E_i(r')|^2 + 2\text{Re}(E_i(r')E_s^*(r', q)) + |E_s(r', q)|^2 \end{aligned} \quad (2.49)$$

The first term of this expression is independent of the particle's position, while the last is much weaker than the others. The second term is then the principal contribution to the position dependence of the signal.

Based on similar interferometric principles, with the help of a Fabry-Perot cavity, accuracies beyond the attometer (10^{-18} m) have been demonstrated [106, 107], a technique now routinely used in gravity interferometers [108]. Figure 2.14 shows how the phase change related to the displacement of a mirror is transduced into a variation of the output intensity, which is (up to a cavity) the principle of our measurement.

Thus, by measuring $I(r', q)$ on a quadrant photodiode, we can (in theory) measure the 3D position of the particle, with a spatial precision of the order of 0.1 nm along x and y , ultimately limited by instrumental noise and the analog-to-digital conversion operated by the acquisition oscilloscope (PicoScope 4824A) and a temporal resolution down to 0.05 μs , related to the bandwidth of the QPD (Hamamatsu S4349).

We first present the derivation of the signal in the paraxial approximation. We then present how the detection is calibrated in the linear range, so that we can associate a signal (S_x, S_y, S_z) to a position (x, y, z) . We finally use the correction proposed in [109] to go beyond, since we will need it for characterizing large nonlinear potentials in chapter 4.

2.4.1 . Detection in the paraxial approximation

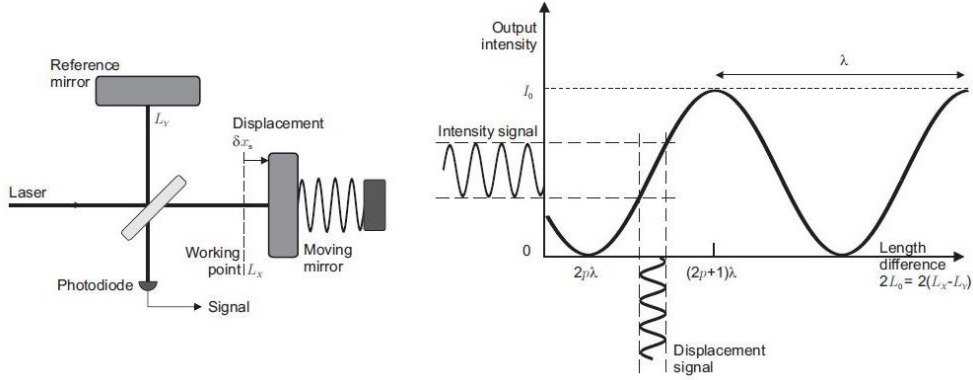


Figure 2.14: Principle of interferometric displacement sensing. In a Michelson interferometer configuration, the wave reflected by the moving mirror interferes with the one reflected by the fixed reference mirror to create an interference pattern on the photodiode. By varying the path difference, any displacement δx_s is then transduced into a measurable variation of intensity. The amplitude of the intensity signal is ultimately defined by the slope of the interference fringe. A great achievement of the optomechanics community was to take advantage of a high-finesse Fabry-Perot cavity to increase this slope and improve the sensitivity of such measurement up to the fundamental quantum limit. Reproduced from PF Cohadon lectures at The New Mechanics Les Houches Summer School 2022.

To measure the position of a particle, we look back at it as a radiating dipole. This time though, we are not interested in the force resulting from the interaction between this dipole and the field, but by the field scattered from the dipole to the detection.

The field scattered by a dipole to a position \mathbf{r} , with \mathbf{q} the position of the particle and $\mathbf{R} = \mathbf{r} - \mathbf{q}$ (with $R = |\mathbf{R}|$ and $\mathbf{n}_R = \mathbf{R}/R$), is given by :

$$\begin{aligned}
 \mathbf{E}_s(\mathbf{r}) &= \omega_i^2 \mu_0 \mathbf{G}(R) \mathbf{p} \\
 &= \omega_i^2 \mu_0 \left[\mathbf{G}_{NF}(R) + \mathbf{G}_{IF}(R) + \mathbf{G}_{FF}(R) \right] \mathbf{p} \\
 &= \omega_i^2 \mu_0 \frac{e^{ikR}}{4\pi R} \left[\frac{1}{k^2 R^2} \left[-\mathbf{I} + 3\mathbf{R}\mathbf{R}^T/R^2 \right] + \frac{i}{kR} \left[\mathbf{I} - 3\mathbf{R}\mathbf{R}^T/R^2 \right] + \left[\mathbf{I} - \mathbf{R}\mathbf{R}^T/R^2 \right] \right] \mathbf{p}
 \end{aligned} \tag{2.50}$$

with ω_i the optical frequency of the measuring laser beam, μ_0 the vacuum magnetic permeability, \mathbf{p} the dipole moment of the particle, \mathbf{I} the identity matrix and \mathbf{G} the Green function. Following [76], its expression can be decomposed into a near-field term \mathbf{G}_{NF} for $R \ll \lambda$, an intermediate-field term \mathbf{G}_{IF} for $R \approx \lambda$ and a far-field term \mathbf{G}_{FF} for $R \gg \lambda$. The two first components are relevant when computing optical binding forces between close particles [110, 111]. In the following, we only consider the last component, which is the most significant for our observations.

To compute the field diffracted by the dipole, we now need to specify the value of \mathbf{p} . As in the first section of this chapter, $\mathbf{p} = \alpha(\omega_i) \mathbf{E}_i(q)$ (note that here the

dipole is oscillating at the optical frequency of the measuring laser field, contrarily to the first section where it was to the frequency of the trapping laser).

For this subsection, we use the Gaussian approximation to describes the measuring laser field. We assume the laser to be linearly polarized along \mathbf{n}_y :

$$\mathbf{E}_i(\mathbf{q}) = E_{i,0} \frac{w_{0z}}{w(q_z)} e^{-\left(\frac{q_x^2}{w_{0x}^2} + \frac{q_y^2}{w_{0y}^2}\right) \frac{w_{0z}^2}{w(q_z)^2} + i\phi(q_x, q_y, q_z)} \mathbf{n}_y \quad (2.51)$$

where

$$\phi(q_x, q_y, q_z) = kq_z - \arctan(q_z/w_{0z}) + \frac{k(q_x^2 + q_y^2)}{2q_z(1 + \frac{w_0^2}{q_z^2})} \quad (2.52)$$

We can now compute the field scattered on the detector, starting with the expression of $\mathbf{G}_{FF}(R) = \frac{e^{ikR}}{4\pi R} [\mathbf{I} - \mathbf{R}\mathbf{R}/R^2] \mathbf{p}$ and making the following assumptions:

- For small observation angles, *i.e.* in the paraxial approximation for the collection lens, $\mathbf{n}_R \cdot \mathbf{n}_y \ll 1$, and thus $\mathbf{R}\mathbf{R}\mathbf{n}_y/R^2 = (\mathbf{n}_R \cdot \mathbf{n}_y)\mathbf{n}_R/R$ can be neglected.
- For small displacements around the focus, the *Fraunhofer approximation* implies to consider that for the amplitude of the scattered field, $R \approx r$, and for the phase, $R = \sqrt{r^2 + q^2} - 2\mathbf{r} \cdot \mathbf{q} \approx r - (\mathbf{r} \cdot \mathbf{q})/r$.

We then obtain :

$$\begin{aligned} \mathbf{E}_s(\mathbf{r}) &= \frac{\omega_i^2 \mu_0}{4\pi r} e^{ik(r-\mathbf{r} \cdot \mathbf{q}/r)} \alpha(\omega_i) \mathbf{E}_i(\mathbf{q}) \\ &= \frac{\omega_i^2 \mu_0}{4\pi r} e^{ik(r-\mathbf{r} \cdot \mathbf{q}/r)} \alpha(\omega_i) E_{i,0} \frac{w_{0z}}{w(q_z)} e^{-\left(\frac{q_x^2}{w_{0x}^2} + \frac{q_y^2}{w_{0y}^2}\right) \frac{w_{0z}^2}{w(q_z)^2} + i\phi(\mathbf{q})} \mathbf{n}_y \\ &\approx \frac{\omega_i^2 \mu_0}{4\pi r} e^{ik(r-\mathbf{r} \cdot \mathbf{q}/r)} \alpha(\omega_i) E_{i,0} e^{i(kq_z - q_z/w_{0z})} \mathbf{n}_y \end{aligned} \quad (2.53)$$

where we consider in the last line that the variations in amplitude of the measuring beam are negligible.

Finally, the scattered field is collimated by the collection lens located at $z = f_{\text{col}}$, meaning that the scattered spherical wavefronts on a reference sphere $\mathbf{r}_o = (x, y, z_o)^T$ with $r_o = f_{\text{col}}$ are transformed into plane waves by an ideal lens of transfer function $e^{-ikf_{\text{col}}} e^{ikz'}$. At $\mathbf{r}' = (x, y, z')^T$ after the lens, the scattered field is thus :

$$\begin{aligned} \mathbf{E}_s(\mathbf{r}') &= \frac{\omega_i^2 \mu_0 \alpha(\omega_i) E_{i,0}}{4\pi r_o} e^{ik(f_{\text{col}} - \mathbf{r}_o \cdot \mathbf{q}/f_{\text{col}})} e^{-ikf_{\text{col}}} e^{ikz'} e^{i(kq_z - q_z/w_{0z})} \mathbf{n}_y \\ &= \frac{\omega_i^2 \mu_0 \alpha(\omega_i) E_{i,0}}{4\pi f_{\text{col}}} e^{ik/\mathbf{r}' - ikq_z \left(1 - \frac{x^2 + y^2}{2f_{\text{col}}^2}\right)} e^{i(kq_z - q_z/w_{0z})} \mathbf{n}_y \\ &= \frac{\omega_i^2 \mu_0 \alpha(\omega_i) E_{i,0}}{4\pi f_{\text{col}}} e^{i(k/\mathbf{r}' + q_z \left(k \frac{x^2 + y^2}{2f_{\text{col}}^2} - 1/w_{0z}\right))} \mathbf{n}_y \end{aligned} \quad (2.54)$$

where $\mathbf{k}_/ = (-kq_x/f_{\text{col}}, -kq_y/f_{\text{col}}, k)^T$ is the wave vector of a tilted plane wave, and where we used $z_o = \sqrt{f_{\text{col}}^2 - (x^2 + y^2)} \approx f_{\text{col}} - \frac{x^2 + y^2}{2f_{\text{col}}}$.

With respect to the forward propagated field, neglecting again the amplitude spatial dependence, we obtain :

$$\begin{aligned} \mathbf{E}_i(\mathbf{r}') &= \frac{E_{i,0}}{f_{\text{col}}/w_{0z}} e^{i(k(f_{\text{col}} - \frac{x^2+y^2}{2f_{\text{col}}}) + k\frac{x^2+y^2}{2f_{\text{col}}} + \phi_{\text{Gouy}})} e^{-ikf_{\text{col}}} e^{ikz'} \mathbf{n}_y \\ &= \frac{E_{i,0}}{f_{\text{col}}/w_{0z}} e^{i(kz' + \phi_{\text{Gouy}})} \mathbf{n}_y \end{aligned} \quad (2.55)$$

with $\phi_{\text{Gouy}} = -\frac{\pi}{2}$ the Gouy phase acquired by the plane wave as it crosses the focus [112].

We can now compute the interference term $2\text{Re}(E_i(r')E_s^*(r', q))$ of $I(r', q)$:

$$\begin{aligned} I(r', q) &= \frac{c\epsilon_0}{2} 2\text{Re}\left(\frac{E_{i,0}}{f_{\text{col}}/w_{0z}} e^{i(kz' + \phi_{\text{Gouy}})} \frac{\omega_i^2 \mu_0 \alpha^*(\omega_i) E_{i,0}^*}{4\pi f_{\text{col}}} e^{-i(k \cdot \mathbf{r}' + q_z (k\frac{x^2+y^2}{2f_{\text{col}}^2} - 1/w_{0z}))}\right) \\ &= \frac{\omega_i^2 \alpha'(\omega_i) w_{0z} |E_{i,0}|^2}{4\pi c f_{\text{col}}^2} \cos\left(\frac{kq_x x}{f_{\text{col}}} + \frac{kq_y y}{f_{\text{col}}} - q_z \left(\frac{k(x^2 + y^2)}{2f_{\text{col}}^2} - \frac{1}{w_{0z}}\right) + \phi_{\text{Gouy}}\right) \end{aligned} \quad (2.56)$$

From this expression, we can deduce that to have a sensitive position detection, we should try to minimize f_{col} or w_{0z} . In our setup, we use a Thorlabs AL1210 aspheric lens, with $f_{\text{col}} = 10$ mm.

The signals measured by the QPD along the 3 axes, noted S_x , S_y and S_z , can then be computed by integrating $I(r', q)$ over their respective domains in cylindrical coordinates :

$$S_x(\mathbf{q}) = \int_0^{\rho_{\text{max}}} \int_{-\pi/2}^{\pi/2} I(\rho, \phi, \mathbf{q}) d\rho d\phi - \int_0^{\rho_{\text{max}}} \int_{\pi/2}^{3\pi/2} I(\rho, \phi, \mathbf{q}) d\rho d\phi \quad (2.57)$$

$$S_y(\mathbf{q}) = \int_0^{\rho_{\text{max}}} \int_0^{\pi} I(\rho, \phi, \mathbf{q}) d\rho d\phi - \int_0^{\rho_{\text{max}}} \int_{\pi}^{2\pi} I(\rho, \phi, \mathbf{q}) d\rho d\phi \quad (2.58)$$

$$S_z(\mathbf{q}) = \int_0^{\rho_{\text{max}}} \int_0^{2\pi} I(\rho, \phi, \mathbf{q}) d\rho d\phi \quad (2.59)$$

with $\rho_{\text{max}} = \text{N.A.} \cdot f_{\text{col}}$ the maximal integration radius given by the collection lens numerical aperture and focal length. The angular domains defined for the respective axes are simply related to the 4 angular domains of the QPD, noted A, B, C and D in figure 2.8.

We can now use these expressions to simulate S_x , S_y and S_z , and gain some insights of their expected behaviour. Figure 2.15 presents iso-contours of S_x and S_z in the $y = 0$ plane. Clearly, one given signal S_x can correspond to many positions, and even a pair (S_x, S_z) is not sufficient to deal with ambiguous measurements. We shall come back to this question in chapter 4.

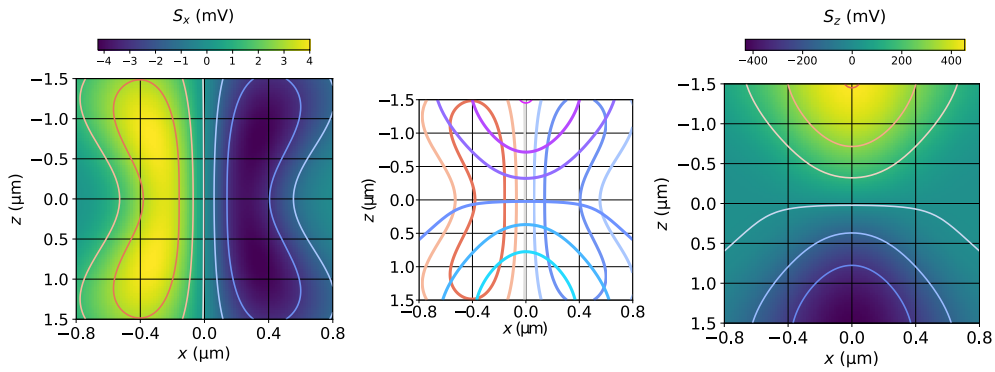


Figure 2.15: Simulated signals S_x and S_z in the plane $y = 0$. A vertical contour in S_x (resp. horizontal contour in S_z) indicates that the measurement does not depend on z (resp. of x). Conversely, a curved contour indicates cross-coupling between the two measurements, a feature we will try to take advantage of in chapter 4.

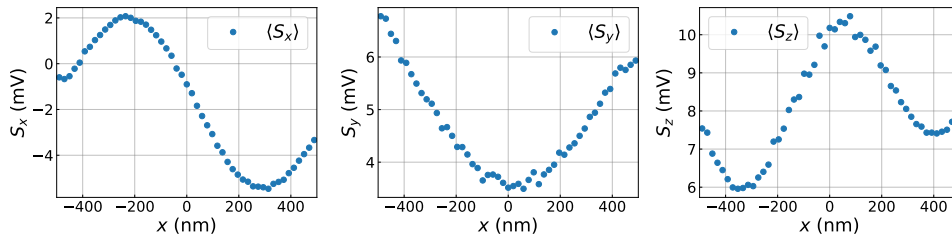


Figure 2.16: Experimental average values of S_x , S_y and S_z while moving a particle over $1 \mu\text{m}$ range along the x axis. While S_x corresponds broadly to what is expected, S_y (which should be zero) and S_z differ markedly, which indicates that the approximations used in computing it are not valid when the displacement is beyond the paraxial range.

Figure 2.16 presents the mean values of S_x , S_y and S_z obtained while moving a trap along the x axis. While S_x look similar to what was presented in the simulation, S_z differs significantly. Also, the width of the linear range of S_x is significantly smaller than the one expected from the model. This is not entirely surprising, since we made a lot of assumptions. The paraxial approximation is difficult to meet with the high N.A. of the collection lens used. Also, our model accounts mostly for phase change, and not intensity change, when the particle moves through the focus. This does not hold when the particle moves at distances comparable to the wavelength of the measuring beam ($\lambda_{\text{meas}} = 785 \text{ nm}$). Moreover, the measured S_z present some asymmetry, while S_y is not constant as would be expected for a perfect displacement along the x axis. Corrections are thus in order to account for the experimental reality of our measurements.

Before moving to this subject, we present here how we can calibrate the motion of the particle that stays close to the center of the measuring beam (*i.e.* in the measurement linear range). This is the case while trapping a particle with a single trapping beam centered on the measurement beam.

2.4.2 . Calibration in the linear range

All our experiments rely on the acquisition of a time trace of signals (S_x, S_y, S_z) from which we infer the real position of the particle (x, y, z) . In the linear range described in the previous subsection, we can thus make the assumption that $S_x = c_{xx}x$ (resp $S_y = c_{yy}y$, $S_z = c_{zz}z$), with c_{ii} the sensitivity of our measurement of i along the i -axis (the necessity of precising both variable and axis of measurement will become clearer in the next subsection). We now clarify how we derive these sensitivities.

The calibration procedure is inspired by E. Heberstreit thesis [81], where more details can be found. As mentioned in section 2.2.2, an efficient way to process the raw signals is to study their PSD.

The equation (2.33), which defines the PSD of a variable x , can readily be applied to a linear transformation of it, such as S_x . The PSD of S_x is thus :

$$\text{PSD}_{S_x S_x}(\Omega) = \frac{A'}{\pi} \frac{\Gamma \Omega_0^2}{(\Omega_0^2 - \Omega^2)^2 + \Gamma^2 \Omega^2} \quad (2.60)$$

where $A' = \langle S_x^2(t) \rangle = \langle (c_{xx}x)^2(t) \rangle = c_{xx}^2 A$

The calibration factor is then simply :

$$c_{xx} = \sqrt{\frac{A'}{A}} = \sqrt{\frac{A' m \Omega_{0x}^2}{k_B T}} \quad (2.61)$$

where we used the expression of A derived in section 2.2.2. In this last equation, all parameters can be computed from a PSD of a time trace of S_x , except m .

This last unknown can be determined by studying more precisely the link between damping and mass. From equation 2.28 in the limit $\text{Kn} \gg 1$, we obtained a

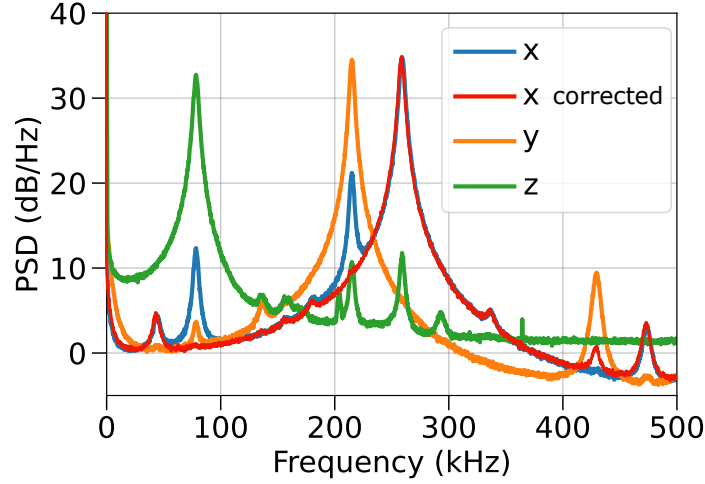


Figure 2.17: Procedure to correct the PSD of signals affected by cross-talk between axes. The initial PSD of S_x , S_y and S_z are fitted to compute c_{xx} , c_{yy} and c_{zz} . Then, we also fit peaks at f_{0y} and f_{0z} on the PSD of S_x , and compute c_{xy} and c_{xz} . We can then compute a corrected signal $S_{x,\text{corrected}} = S_x - \frac{c_{xy}}{c_{yy}} S_y - \frac{c_{xz}}{c_{zz}} S_z$, whose PSD does not present auxiliary peaks.

simple relation between Γ and the Knudsen number $\text{Kn} = l/r_{\text{part}}$. The mean free path is related to the pressure p_{gas} through :

$$l = \frac{\eta}{p_{\text{gas}}} \sqrt{\frac{\pi N_A k_B T}{2M}} \quad (2.62)$$

with $M = 28.97 \times 10^{-3} \text{ kg}\cdot\text{mol}^{-1}$ the molar mass of dry air, and $N_A = 6.022 \times 10^{23} \text{ mol}^{-1}$ the Avogadro number. By injecting this expression in 2.28, we obtain :

$$r_{\text{part}} = 0.619 \frac{9}{\sqrt{2\pi\rho_{\text{part}}}} \sqrt{\frac{M}{N_A k_B T}} \frac{p_{\text{gas}}}{\Gamma_{\text{gas}}} \quad (2.63)$$

where $\rho_{\text{part}} = 2200 \text{ kg}/\text{m}^3$ is the density of the silica particle. This expression tells us that the ratio $p_{\text{gas}}/\Gamma_{\text{gas}}$ is proportional to r_{part} . By fitting PSDs of time traces acquired at different pressures (over the mbar), we can thus establish the variation of Γ as a function of p_{gas} , as was shown in the calibration figure 2.9 a. A linear fit of this curve directly leads to r_{part} , which is equal to 88 nm in this case, significantly bigger than the value expected from the manufacturer (for our experiments, microParticles GmbH, which indicates $r_{\text{part}} = 75.5 \pm 2.5 \text{ nm}$).

We can thus determine the mass of the particle, and consequently c_{xx} , as well as c_{yy} and c_{zz} .

Moreover, sensitivities c_{ij} of the j -axis measurement to motion along the i -axis can also be obtained by fitting the peak located at the frequency f_i in a PSD of S_j . From an experimental point of view, it is indeed frequent to observe cross-talk in measurement, due to misalignment of the measuring beam respectively to the

trapping beam, as can be seen on figure 2.17, where peaks at f_{0y} and f_{0z} are visible on the PSD of S_x . Under certain conditions, it is possible to correct raw time traces to remove this cross-talk. Let's consider that we observe two peaks in the PSD of the signal along the i -axis, which are related to motion along the i -axis and along the j -axis. A simple procedure can be described as follow:

- Compute the sensitivities c_{ij} of the multi-peaked PSD along i we want to correct.
- For singled-peaked PSD along j , compute c_{jj} .
- Subtract to the time trace S_i the renormalized time traces $S_j \frac{c_{ij}}{c_{jj}}$. This is legitimate as long as the measurement is linear and the variables i and j are statistically independent.

This way, the resulting PSD should only have one peak corresponding to the true displacement. This procedure can be extended to remove higher order combinations of the true oscillation frequencies, which are frequent in levitation experiments [113].

2.4.3 . Realistic model of extended measurement

The assumptions from the previous subsection are not valid anymore when the particle is moved far from the measuring beam, which is the case during the calibration procedure and will be at the center of chapter 4.

A more thorough characterization of our measurement beam is thus necessary to make the best use of the large nonlinear potentials we seek to obtain.

To deal with this, we look again at the spectral domain. The PSDs of time traces recorded while moving a trapped particle over 1 μm range are presented in figure 2.18

We observe two things :

- For each axes, variations of the intensity of the main peaks.
- Secondary peaks appearing for certain positions, an effect already noticed for large potentials such as double-wells [57].

From each peaks of these PSD signals, we can compute the c_{ij} , pictured in figure 2.19 b..

Some corrections to the simple linear model presented in the previous section are thus necessary :

- The paraxial approximation is no more valid over a range bigger than the waist of the measurement laser (estimated at 260 nm).
- The sources of shifts and asymmetries should be better accounted in the model, by taking inspiration of what is observed in other interferometric systems [114, 115].

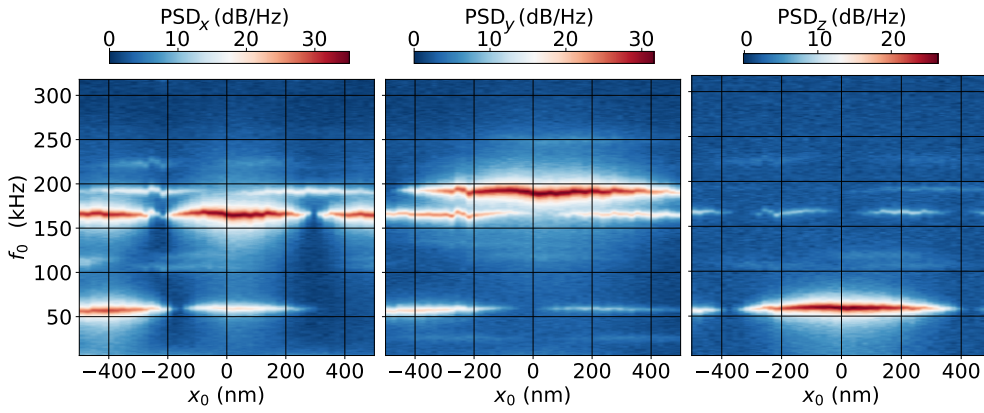


Figure 2.18: PSD recorded along the x , y and z axes while moving the trap along x over $1\ \mu\text{m}$. While at the origin the three PSD present distinct peaks at f_{0x} , f_{0y} and f_{0z} , their intensity fluctuates while moving the trap, and cross-coupling appears, underscoring the complex nature of the field detected by the QPD. Note that the trapping frequencies variations as a function of x_0 are just related to the position-dependent efficiency of the AOM discussed previously.

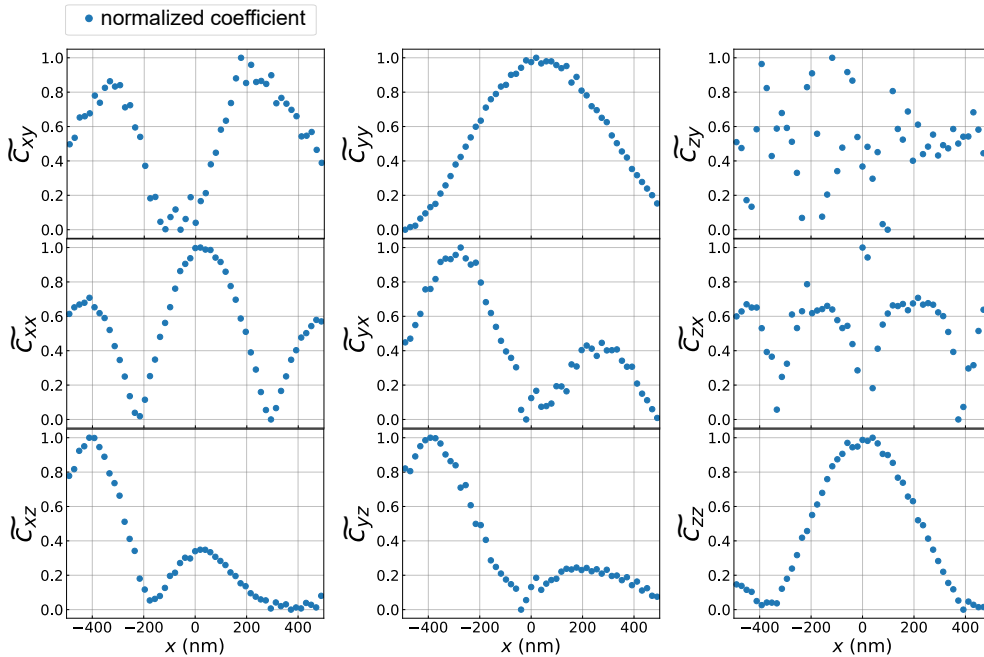


Figure 2.19: Normalized \tilde{c}_{ij} , computed from the PSD shown in figure 2.18. As can be observed, these curves are not symmetric, which indicates that the simple model presented in the previous subsection will not hold for real measurements.

We first present how the expression should be modified, and then our current understanding of how different sources of displacements affect the c_{ij} over the whole range of measurement.

2.4.3.1 . Detection beyond the paraxial approximation

Here, we present a modified expression of $I(q, r')$ based on corrections to the paraxial approximation of a Gaussian beam proposed in [116, 109].

First, we consider that the field, supposed to be linearly polarized along \mathbf{n}_y , has a non-zero component along the z axis. The correction is then based on an expansion in powers of the divergence angle $s = \lambda/(2\pi w_0)$:

$$\begin{aligned} \mathbf{E}_i(\mathbf{q}) = & (E_{i,y,0}(\mathbf{q}) + s^2 E_{i,y,2}(\mathbf{q}) + s^4 E_{i,y,4}(\mathbf{q}))\mathbf{n}_y \\ & + (s(E_{i,z,1}(\mathbf{q}) + s^3(E_{i,z,3}(\mathbf{q}))\mathbf{n}_z + \mathcal{O}(s^5)) \end{aligned} \quad (2.64)$$

with

$$E_{i,y,0}(\mathbf{q}) = \frac{e^{ikz}}{1 + iz/(2w_0z)} e^{-\frac{x^2+y^2}{2w_0^2(1+iz/(2w_0z))}} \quad (2.65)$$

$$E_{i,y,2}(\mathbf{q}) = -\frac{iz/w_0}{(1 + iz/(2w_0z))^2} L_2 \left[\frac{x^2 + y^2}{2w_0^2(1 + iz/(2w_0z))} \right] E_{i,y,0}(\mathbf{q}) \quad (2.66)$$

$$\begin{aligned} E_{i,y,4}(\mathbf{q}) = & -\frac{3iz/(2w_0z)}{(1 + iz/(2w_0z))^4} \left[L_4 \left[\frac{x^2 + y^2}{2w_0^2(1 + iz/(2w_0z))} \right] \right. \\ & \left. + \frac{x^2 + y^2}{8w_0} L_3 \left[\frac{x^2 + y^2}{2w_0^2(1 + iz/(2w_0z))} \right] \right] E_{i,y,0}(\mathbf{q}) \end{aligned} \quad (2.67)$$

$$E_{i,z,1}(\mathbf{q}) = -\frac{iy}{w_0} \frac{e^{ikz}}{(1 + iz/(2w_0z))^2} \exp -\frac{x^2 + y^2}{2w_0^2(1 + iz/(2w_0z))} \quad (2.68)$$

$$\begin{aligned} E_{i,z,3}(\mathbf{q}) = & \left[\frac{1}{(1 + iz/(2w_0z))} L_1 \left[\frac{x^2 + y^2}{2w_0^2(1 + iz/(2w_0z))} \right] \right. \\ & \left. - \frac{iz/(2w_0z)}{(1 + iz/(2w_0z))^2} L_2 \left[\frac{x^2 + y^2}{2w_0^2(1 + iz/(2w_0z))} \right] \right] E_{i,z,1}(\mathbf{q}) \end{aligned} \quad (2.69)$$

where $L_a^b(x)$ is a generalized Laguerre polynomial.

Now, to the difference of the paraxial case, we see that we have a non-negligible contribution along \mathbf{n}_z . In the expression of $\mathbf{G}_{FF}(R) = \frac{e^{ikR}}{4\pi R} [\mathbf{I} - \mathbf{R}\mathbf{R}/R^2] \mathbf{p}$, this implies :

- In the $\mathbf{R}\mathbf{R}/R^2 \mathbf{p}$ term, the most important contribution is along the z axis and gives $\frac{R_z^2 p_z / \alpha}{R^2} \approx \frac{p_z}{\alpha} \mathbf{n}_z$
- This simplifies with \mathbf{I} to fall back to $\frac{p_y}{\alpha} \mathbf{n}_y$. Thus, we find that the far field scattered by the dipole is still aligned along the polarization direction of the incident field, whatever the refinement in its definition.

- We still use the Fraunhofer approximation in the phase and amplitude definitions.

We then obtain :

$$\mathbf{E}_s(\mathbf{r}) = \frac{\omega_i^2 \mu_0}{4\pi r} e^{ik(r-\mathbf{r}\cdot\mathbf{q}/r)} \alpha(\omega_i) (E_{i,y,0}(\mathbf{q}) + s^2 E_{i,y,2}(\mathbf{q}) + s^4 E_{i,y,4}(\mathbf{q})) \mathbf{n}_y \quad (2.70)$$

Compared with the paraxial approximation, the scattered field is thus only modified by the corrective terms along y .

With respect to the forward propagated field, we reuse :

$$\mathbf{E}_i(\mathbf{r}') = \frac{E_{i,0}}{f_{\text{col}}/w_{0z}} e^{i(kz' + \phi_{\text{Gouy}})} \mathbf{n}_y \quad (2.71)$$

We can now compute the interference term $2\text{Re}(E_i(r')E_s^*(r', q))$ of $I(r', q)$:

$$I(r', q) = \frac{c\epsilon_0}{2} 2\text{Re} \left(\frac{E_{i,0}}{f_{\text{col}}/w_{0z}} e^{i(kz' + \phi_{\text{Gouy}})} \frac{\omega_i^2 \mu_0 \alpha^*(\omega_i) E_{i,0}^*}{4\pi f_{\text{col}}} e^{-i(k/\cdot\mathbf{r}' + kqz \left(\frac{x^2 + y^2}{2f_{\text{col}}^2} - 1\right))} (E_{i,y,0}(\mathbf{q}) + s^2 E_{i,y,2}(\mathbf{q}) + s^4 E_{i,y,4}(\mathbf{q})) \right) \quad (2.72)$$

There is no easy way to simplify this expression. We thus rely on the *SymPy* library to compute the complete expression (as well as their derivatives along q_x , q_y and q_z , which are used to compute the theoretical sensitivities c_{ij}).

2.4.3.2 . Identification of sources of bias in interferometric measurement

The previous refinement does not account for the asymmetries observed in figure 2.19. As shown previously on figure 2.16, the fact that $\langle S_y \rangle$ is not zero indicates that while moving the trap linearly along x , it moves along curved trajectories in y and z . This, plus the imperfect position and orientation of the measuring beam, generates additional optical path lengths differences. Phenomenons related to such imperfections are well characterized in the field of precision interferometry under the name of *Tilt-to-length coupling* [114, 115].

Thus, a few more modifications of equation 2.72 should be taken into account, which are represented on figure 2.20.

- First, the fact that the measuring beam is not perfectly superposed with the trapping beam in initial position (*i.e.* the position at which we aligned our system, noted $x = 0$ in figures) is represented by a 3D shift R_0 .
- Second, the fact that the trap follows a curved trajectory in y and z while the trapping beam is moved along x is captured by considering second order

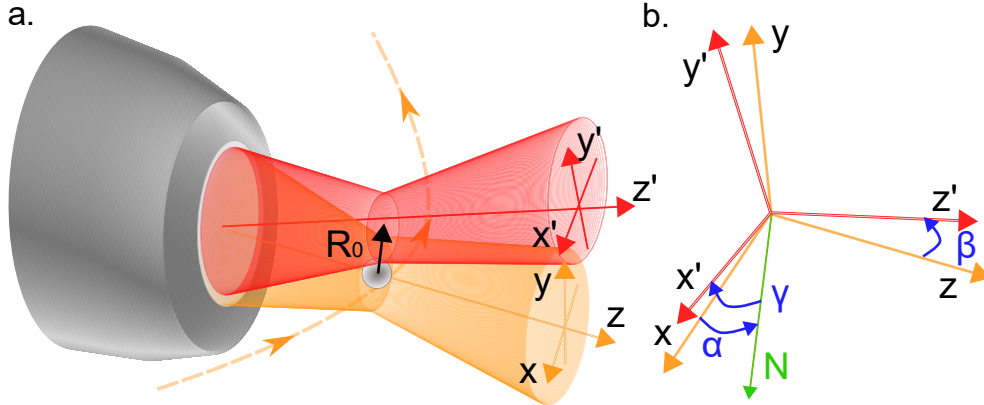


Figure 2.20: a. Representation of the position of misaligned trapping (orange) and measuring (red) beams. The two beams do not overlap perfectly, creating a 3D offset R_0 . Moreover, while the measuring beam is static, the trapping beam is moved along the x axis. While this should not affect its position along y and z (which should remain at R_{0y} and R_{0z}), in reality the trap follows the orange curved trajectory. Finally, the angular misalignment of the beams can be interpreted as a change of frame, represented on b. by Euler angles α, β and γ in the (ZXZ) convention.

polynomials in x for the coordinates. We thus have :

$$\begin{aligned} q'_x &= q_x - R_{0x} \\ q'_y &= a_y q_x + b_y q_x^2 - R_{0y} \\ q'_z &= a_z q_x + b_z q_x^2 - R_{0z} \end{aligned}$$

- Third, we propose to take into account the angular misalignment of the two beams. Indeed, while the particle oscillates along the 3 axes defined by the trapping beam, the scattered field is in the frame of the measurement laser. By using Euler angles, we thus convert the coordinates of the particle in the frame of the trapping beam to the frame of the measuring beam :

$$\begin{pmatrix} q''_x \\ q''_y \\ q''_z \end{pmatrix} = \begin{pmatrix} c_\alpha c_\gamma - s_\alpha c_\beta s_\gamma & -c_\alpha s_\gamma - s_\alpha c_\beta c_\gamma & s_\alpha s_\beta \\ s_\alpha c_\gamma + c_\alpha c_\beta s_\gamma & c_\alpha c_\beta c_\gamma - s_\alpha s_\gamma & -c_\alpha s_\beta \\ s_\beta s_\gamma & s_\beta c_\gamma & c_\beta \end{pmatrix} \begin{pmatrix} q'_x \\ q'_y \\ q'_z \end{pmatrix} \quad (2.73)$$

where c_α and s_α hold for $\cos \alpha$ and $\sin \alpha$ respectively.

We can then compute more realistically the values of S_x, S_y and S_z for a given position, as well as the c_{ij} , since :

$$c_{ij} = \frac{\partial S_i}{\partial q_j} \quad (2.74)$$

Conversely, we could use these expressions to better characterize our system. Indeed, by running a minimization procedure (simulated annealing) over the ensemble of distances between normalized measured and theoretical $\langle S_i \rangle$ and c_{ij} for

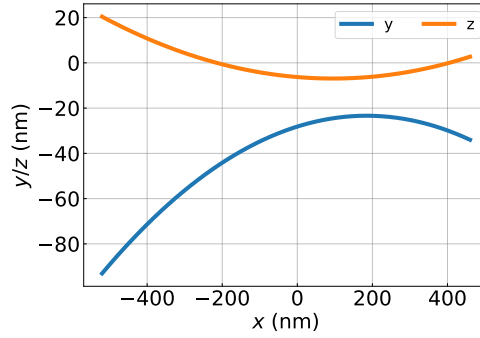


Figure 2.21: Real displacement of the trapping beam along y and z when moved along the x axis, estimated from the fits presented in figure 2.22.

all positions, we gain information on the waist, position and tilt of the measuring beam, as well as the real 3D path of the trapping beam while moving along x .

As can be seen on figure 2.22, the results of the fitting procedure are satisfying, except along the z axis. The observed asymmetries are taken into account, although the fitting procedure do not converge on the whole set. From a computing perspective, our choice of parameters could probably be improved by reducing the number of variables, or determining if a smaller set of S_i and c_{ij} is sufficient to determine unambiguously all the parameters.

The values obtained from the theoretical fits in figure 2.22 are yet a good first indicator :

- $w_0 = 266$ nm
- $R_0 = (30, 29, 6)$ nm
- $(\alpha, \beta, \gamma) = (-1, -23, -48)$ mrad
- $a_y = 0.06$, $a_z = -0.018$ and $b_y = -0.14 \mu\text{m}^{-1}$, $b_z = 0.072 \mu\text{m}^{-1}$, the corresponding curves being shown in figure 2.21

As underlined in chapter 4, a perfect alignment of the trapping and measuring laser is paramount to avoid unwanted perturbations of large potentials. To obtain better alignments, the use of piezoelectric adjusters, combined with an automation of this 3D calibration procedure, would probably be beneficial.

More work is thus needed to confirm the pertinence of this approach, and when testing the Unscented Kalman Filter in chapter 4, we will mainly rely on a linearized expression of S_x , S_y and S_z , of the form :

$$S_i(q_x, q_y, q_z) = \langle S_i(q_x, q_y, q_z) \rangle + \sum_j c_{ij} q_j \quad (2.75)$$

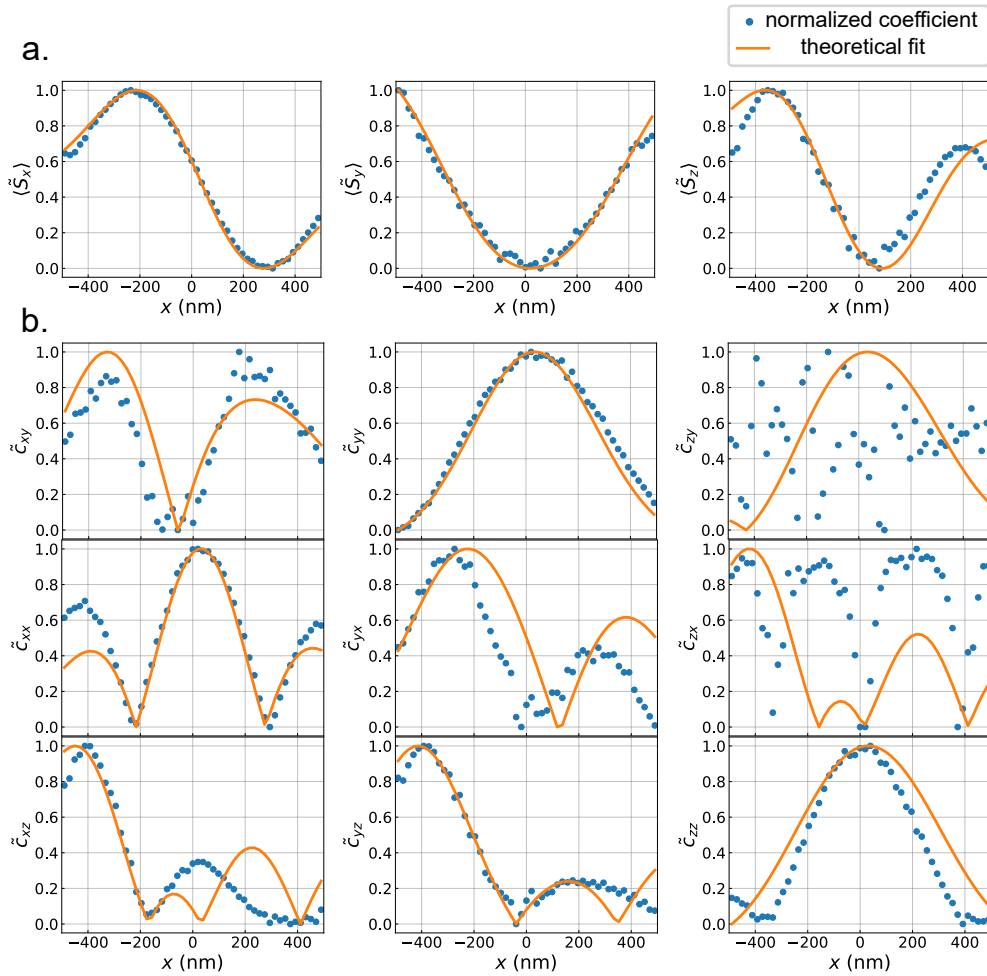


Figure 2.22: Results of the fitting procedure of normalized S_i (a.) and c_{ij} (b.) used to determine the geometric characteristics of the measurement beam. The procedure is computationally intensive, but produces encouraging results along the x and y axes.

3 - Shortcuts to equilibrium in the underdamped regime

Et la troisième fois fut quand Gilberte me dit : « Si vous voulez, nous pourrons tout de même sortir un après-midi et nous pourrons aller à Guermantes, en prenant par Méséglise, c'est la plus jolie façon », — phrase qui, en bouleversant toutes les idées de mon enfance, m'apprit que les deux côtés n'étaient pas aussi inconciliables que j'avais cru.

— Marcel Proust, ALBERTINE DISPARUE (1925)

The development of stochastic energetics, presented in chapter 1, led to a renewed interest in the temporal description of thermodynamic transformation at the mesoscale. Indeed, when a stochastic system initially at thermal equilibrium is perturbed by an external force, it undergoes a transient regime before reaching a new equilibrium. During this regime, the system is out of equilibrium for a characteristic relaxation time, which depends on its physical properties and its coupling to the environment. An understanding of how evolves the dynamics of the system then offers different venues to improve state-to-state transformations, for instance:

- Try to minimize the heat dissipated in the environment during the transformation, and simultaneously try to maximize the heat taken from it.
- Try to shorten as much as possible the transient regime.

While these questions arise naturally when considering classical heat engines, they take on a subtler meaning when dealing with their nanoscale versions, where heat and work are by definition fluctuating quantities.

Regarding the first question, different protocols have been designed to improve the efficiency of stochastic heat engines, respectively, in the overdamped [117, 47, 118] and underdamped [119] regimes. Although these protocols allow to theoretically operate at the thermodynamic limit, they do so through slow, quasi-static processes.

This justifies to look more closely at the second question. Shortening return to equilibrium has been at the centre of intense theoretical and experimental work in the last decade. Interestingly, these efforts stem from quantum physics, where the manipulation of quantum states must happen at times shorter than their decoherence rate. The field of shortcuts to adiabaticity (STA) is thus motivated by finding protocols to steer a quantum system from an initial eigenstate of an initial Hamiltonian to a final eigenstate in a finite time t_f shorter than an existing adiabatic transition [120].

This approach was first transposed to overdamped thermal systems, with the design of the so-called *Engineered Swift equilibrium* (ESE) protocol, which allows accelerating by two orders of magnitude the equilibration time [121]. Along similar lines, the Shortcut-to-Isothermal protocol was developed [122] and applied [123] to perform fast isothermal compressions/expansions.

Due to inertia, the derivation and implementation of shortcuts to equilibrium in the underdamped regime is more complex. It is indeed necessary to control not only the evolution of the position distribution $\rho(x)$ but also the velocity distribution $\rho(v)$. A first protocol in the underdamped regime was designed to control the motion of the cantilever of an atomic force microscope (AFM) [124]. This effectively reduced the time necessary for the cantilever to equilibrate after a displacement by two orders of magnitude, allowing to perform faster measurements. Nevertheless, such protocols addressing particle transport are oblivious to fluctuations, since only the averaged particle position are accounted for. More subtle protocols are then required to control, in a general case, the system's position and velocity simultaneously.

In this chapter, we thus study the dynamics of transient regimes at the nano-scale, with a levitated particle. This latter constitutes an ideal system for such study, since we can finely control the coupling to the environment by controlling the gas pressure. We first describe the main relaxation regimes. On one hand, the overdamped regime is encountered in situations in which the inertia of the system can be neglected. In contrast to this, inertial effects have to be taken into account in the underdamped regime. Next, we demonstrate a first application of the Engineered Swift Equilibrium protocols derived by Chupeau et al. to an underdamped system [125]. We conclude by discussing the robustness of these protocols against parameters variations.

3.1 . Relaxations in the overdamped and underdamped regimes

3.1.1 . STEP protocols

In this section, we consider the situation pictured in figure 3.1, which represents a STEP protocol for an expansion :

- A Brownian particle is trapped in a harmonic potential of initial stiffness k_i , at thermal equilibrium with its environment, made of gas particles which affect the particle through the damping rate Γ introduced in chapter 2. Its equilibrium distribution is thus given as stated by $\rho_{eq,i}(x) = \rho_{x,0} e^{-\frac{U(x)}{k_B T}} = \rho_{x,0} e^{-\frac{k_i x^2}{2k_B T}}$
- The stiffness of the potential is abruptly changed to $k_f < k_i$, and the particle undergoes a transient regime, during which it is out-of-equilibrium.
- Finally, it reaches a new equilibrium after a time t_{relax} , characterize by a new

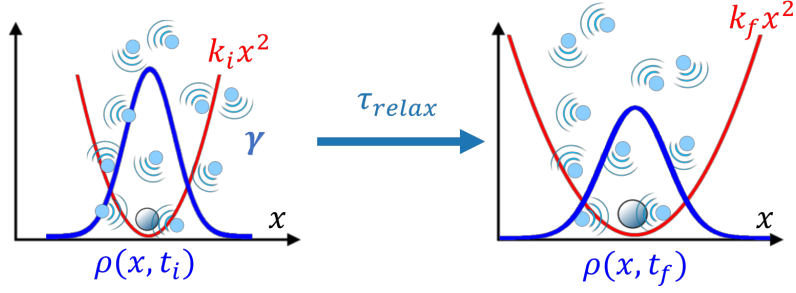


Figure 3.1: Principle of isothermal expansions. A Brownian particle is trapped in a harmonic potential of initial stiffness k_i , and damped by stochastic shocks with the surrounding molecules of gas (pale blue dots), accounted for by a damping term Γ . Upon a change in stiffness to k_f , the probability density function $\rho(x)$ relaxes from its initial shape $\rho(x, t_i)$ into a new equilibrium distribution $\rho(x, t_f)$, in a finite time t_{relax} .

equilibrium distribution $\rho_{eq,f}(x) = \rho_{x,0} e^{-\frac{k_f x^2}{2k_B T}}$, which is thus broader than $\rho_{eq,i}(x)$.

To observe experimentally the relaxation rate of a levitated nanoparticle, we control the stiffness of the trapping potential through the AOM as described in chapter 2. The response time of the AOM being of the order of 160 ns, *i.e.* a lot faster than the characteristic frequency of the particle (in the hundreds of kHz), the change can be considered as instantaneous from the perspective of the particle. By repeating this process $2 \cdot 10^4$ times, and acquiring time traces of the positions of the particle, it is then possible to compute for each time a histogram, which allows to approximate the evolution of $\rho(x, t)$. To counteract drifts of the laser beam (due to external disturbances such as air turbulence), each time trace was re-centered to $x = 0$ by subtracting its mean value at equilibrium.

3.1.2 . Theoretical model of relaxation

Throughout this chapter, we consider that the trapping potential is always harmonic. Consequently, the distributions $\rho(x, t)$ and $\rho(v, t)$ are supposed to be Gaussian at all times. As outlined in chapter 2, Gaussian distributions are entirely characterized by their mean and variances. This allows us to derive a simple theoretical model of the expected evolution of these distributions, by considering only the variances in position σ_{xx} and velocity σ_{vv} (respectively related to the potential and the kinetic energy of the system), as well as $\sigma_{xv} = \langle xv \rangle - \langle x \rangle \langle v \rangle$ (which represents the degree of correlations between x and v). We introduce here the angular frequency $\omega = \sqrt{k(t)/m}$, with $\omega_i = \sqrt{k_i/m}$ and $\omega_f = \sqrt{k_f/m}$.

To first order, these quantities are coupled through the linear system [126]:

$$\frac{d}{dt} \begin{pmatrix} \sigma_{xx} \\ \sigma_{xv} \\ \sigma_{vv} \end{pmatrix} = \begin{pmatrix} 0 & 2 & 0 \\ -\omega^2 & -\Gamma & 1 \\ 0 & -2\omega^2 & -2\Gamma \end{pmatrix} \begin{pmatrix} \sigma_{xx} \\ \sigma_{xv} \\ \sigma_{vv} \end{pmatrix} + \begin{pmatrix} 0 \\ 0 \\ \frac{2k_B T_0 \Gamma}{m} \end{pmatrix} \quad (3.1)$$

Solving this set of equations for the initial conditions $\sigma_{xx}(0) = \sigma_i = \sqrt{\frac{k_B T}{m\omega_i^2}}$ and $\sigma_{vv}(0) = \sigma_i \omega_i^2 = \sqrt{\frac{k_B T}{m}}$ leads to :

$$\sigma_{xx}(t) = \sigma_i \frac{\chi - 1}{\chi} \left[\frac{2\omega_f^2}{\tilde{\Omega}^2} + \frac{2\omega_f^2 - \Gamma^2}{\tilde{\Omega}^2} \cos \tilde{\Omega}(t) + \frac{\Gamma}{\tilde{\Omega}} \sin \tilde{\Omega}(t) \right] e^{-\Gamma(t)} + \frac{\sigma_i}{\chi} \quad (3.2)$$

with $\tilde{\Omega} = \sqrt{4\omega_f^2 - \Gamma^2}$.

From this solution, one can thus differentiate between two characteristic regimes of relaxation :

- When $\Gamma \gg \omega_f$, 3.2 simplifies into

$$\sigma_{xx}(t) = \frac{\sigma_i}{\chi} \left[1 + (\chi - 1)e^{-\Gamma(t-t_0)} \right] \quad (3.3)$$

This defines the overdamped regime of relaxation, where the characteristic time is given by $t_x = \Gamma/\omega_f^2$. This can be understood as the time necessary for the particle to diffuse and explore the new potential, which is slowed down by the surrounding viscous environment.

- On the contrary, when $\Gamma \ll \omega_f$, the solution becomes :

$$\sigma_{xx}(t) = \sigma_i \frac{\chi - 1}{2\chi} [1 + \cos(2\omega_f t)] e^{-\Gamma t} + \frac{\sigma_i}{\chi} \quad (3.4)$$

Here, the characteristic time is $t_v = 1/\Gamma$, which is characteristic of the underdamped regime. The behaviour is markedly different from the overdamped regime : the particle swiftly explores the new potential, but needs time to thermalize and diffuse its kinetic energy to the environment.

3.1.3 . Experimental results

Underdamped regime

We first present results obtained in the underdamped regime. The evolution of $\rho(x, t)$ is plotted in figure 3.2 for an expansion STEP protocol with a compression factor $\chi = \frac{k_f}{k_i} = 0.6$ performed at a pressure $P_{\text{gas}} = 5$ mbar. Figure 3.2 a. shows that the particle, initially strongly confined in a range of ± 20 nm relaxes after the change to a broader distribution. This is confirmed by observing ρ_i and ρ_f (blue and orange lines in a., separately plotted in b.). As aforementioned, ρ_{eq} is of Gaussian shape, with 0 mean, skewness and excess kurtosis.

To better understand the energetics of our system, the time evolution of σ_x , σ_{v_x} and $\langle xv \rangle$ during the protocol are plotted on figure 3.3.

First, we observe steady values $\sigma_{x,i,f}^{\text{eq}} = \sqrt{k_B T/k_{i,f}}$ and $\sigma_{v_x,i,f}^{\text{eq}} = \sqrt{k_B T/m}$, as expected from the equipartition theorem. In particular, we verify that $\left(\frac{\sigma_{x,i}^{\text{eq}}}{\sigma_{x,f}^{\text{eq}}} \right)^2 = \chi = 0.6$.

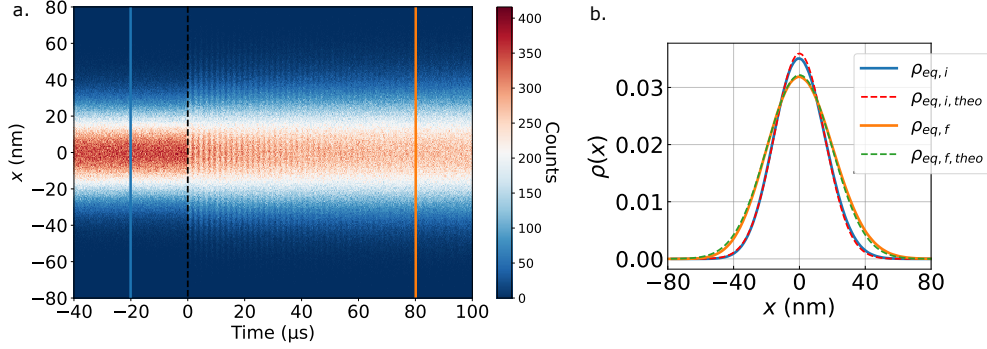


Figure 3.2: a. Time evolution of ρ during a STEP protocol performed in the underdamped regime, obtained by computing for each time t an histogram from the $2 \cdot 10^4$ positions $x(t)$ (each time trace being re-centered by subtracting its mean value). After an abrupt change of k_x at $t = 0$ (dotted black line), ρ oscillates before reaching $\rho_{eq,f}$. b. Two cuts of ρ at equilibrium before (blue) and after (orange) the STEP protocol, corresponding to the vertical lines in a. . Dotted lines corresponds to fits demonstrating their Gaussian nature. We verified that $(\sigma_{x,i}^{eq}/\sigma_{x,f}^{eq})^2 = \chi = 0.6$

Second, these quantities undergo a transient regime from one equilibrium state to another, characterized by damped oscillations in phase opposition between σ_x and σ_{v_x} . These oscillations correspond to a coherent exchange between the system's average potential and kinetic energies.

Third, the cross-correlation $\langle xv \rangle$ is initially very high, and follows like σ_x and σ_{v_x} an oscillating exponential decay.

Finally, from a fit of σ_x to the analytical solution presented below, we verify that in the strongly underdamped regime achieved here ($\Gamma \ll \omega_f$), the oscillation frequency is twice the natural trap frequency, $\omega_{relax} = 2\omega_{x,f} = 2\pi \times 519$ kHz. From the fit, we also obtain the system characteristic relaxation time $t_{relax} \approx 51$ μ s, which leads to a STEP total equilibration time close to $3t_v = 153$ μ s¹.

As a last remark, we note that the measure of t_{relax} provides a better estimation of the system damping Γ than the measure of the PSD. Below a few millibars, the value of Γ estimated from the relaxation experiment differs from the linewidth of the PSD Γ_{PSD} , as shown in figure 3.4. This effect can be attributed to the Duffing non-linearities of the optical potential, which artificially broaden the PSD [80]. A simple model to account for this effect is to consider that

$$\Gamma_{PSD} = \sqrt{\Gamma^2 + \Gamma_{NL}^2}, \quad (3.5)$$

where Γ is the natural system damping, and Γ_{NL} the broadening induced by the potential non-linearities. For our optical trap, at frequency ω_0 , based on a Gaussian

¹Given the exponential decay of the STEP relaxation we assume that equilibrium is reached after about three times the measured relaxation time, when σ_x as reached 95% of its final value.

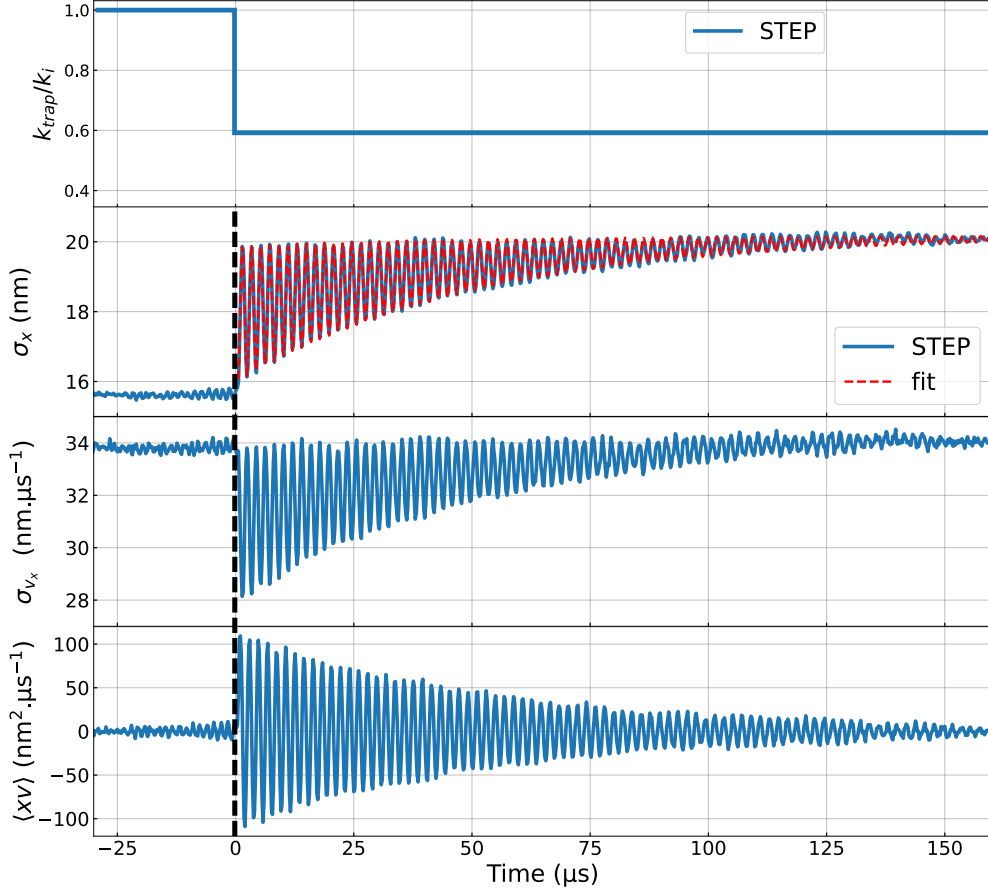


Figure 3.3: Time evolution of k_{trap}/k_i , σ_x , σ_{v_x} and $\langle xv \rangle$ in the case of an underdamped expansion STEP protocol performed at $p_{\text{gas}} = 5$ mbar with $\chi = 0.6$. The initial value of σ_x is $\sigma_{x,i}^{\text{eq}} = 15.5$ nm, while the final value is $\sigma_{x,f}^{\text{eq}} = 20$ nm, hence verifying $(\sigma_{x,i}^{\text{eq}}/\sigma_{x,f}^{\text{eq}})^2 = 0.6 = \chi$. After the abrupt change in stiffness performed at $t = 0$, a transient regime is characterized by σ_x and σ_{v_x} oscillating in phase oppositions at $2\omega_{x,f}$. The correlations between x and v_x are visible on $\langle xv \rangle$. These observations illustrate that the relaxation time in the underdamped regime is mainly due to the relaxation of the velocities, $t_v = 1/\Gamma$, which is the time needed for the particle to thermalize in the new trapping potential.

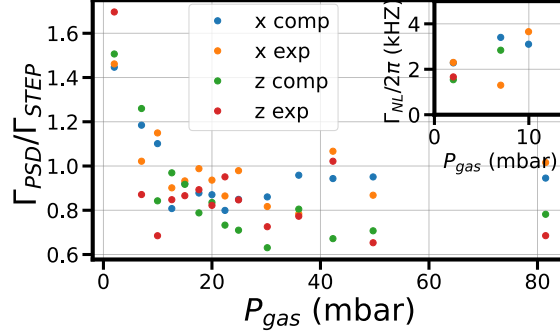


Figure 3.4: Ratios of the linewidth of the PSDs to the damping measured from a fit to the transient regime of compression and expansion STEP protocols at different pressures, over x and z axes. Inset : the nonlinear damping Γ_{NL} computed from equation (3.5), which is in good agreement with the value expected from the nonlinear broadening (equation (3.6)).

beam of waist w_0 , we expect [87]:

$$\Gamma_{\text{NL}} \approx \frac{3}{2} \frac{k_B T}{m w_0^2 \omega} \approx 2\pi \times 2.6 \text{ kHz}. \quad (3.6)$$

This value agrees well with the value we found in the experiment (see inset of figure 3.4). Thus, STEP relaxation measurements are a simple alternative to the standard relaxation approach used to measure the levitated particle damping at low pressure [62] and that require to feedback cool the particle.

Overdamped regime

The behaviour is markedly different in the overdamped regime. At atmospheric pressure $p_{\text{gas}} = 1 \text{ bar}$, we perform a compression of the trap by a factor of $\chi = 1.4$, with $\omega_{x,f} = 2\pi \times 269 \text{ kHz}$ and $\omega_{z,f} = 2\pi \times 105 \text{ kHz}$. The resulting evolution of σ_x , σ_z and $\langle z \rangle$ are shown in figure 3.5. Here, the limiting timescale is given by $t_i = \Gamma/\omega_i^2$ with $i \in \{x, y, z\}$. In agreement with these values, a fit of σ_x and σ_z gives $t_x = 1.5 \mu\text{s}$ and $t_z = 12 \mu\text{s}$. These differences, which were not observed in the underdamped regime, are a direct consequence of the different oscillation frequencies, and suggest that in the overdamped regime, it will be advantageous to perform shortcuts to equilibrium along the z -axis, which is the slowest one. Moreover, due to experimental issues that were not solved at the time of this experience (the thermal lensing of the AOM mentioned in section 2.3.2), the trap was moving along the z -axis during the STEP protocols, which allows observing the relaxation in mean position $\langle z \rangle$. A fit of the transient regime, with a relaxation time equal to t_z , shows that the relaxation is here happening in position.

To summarize, figure 3.6 gives a representation in log-scale of the two domains of relaxation. While the overdamped and the deeply underdamped domains

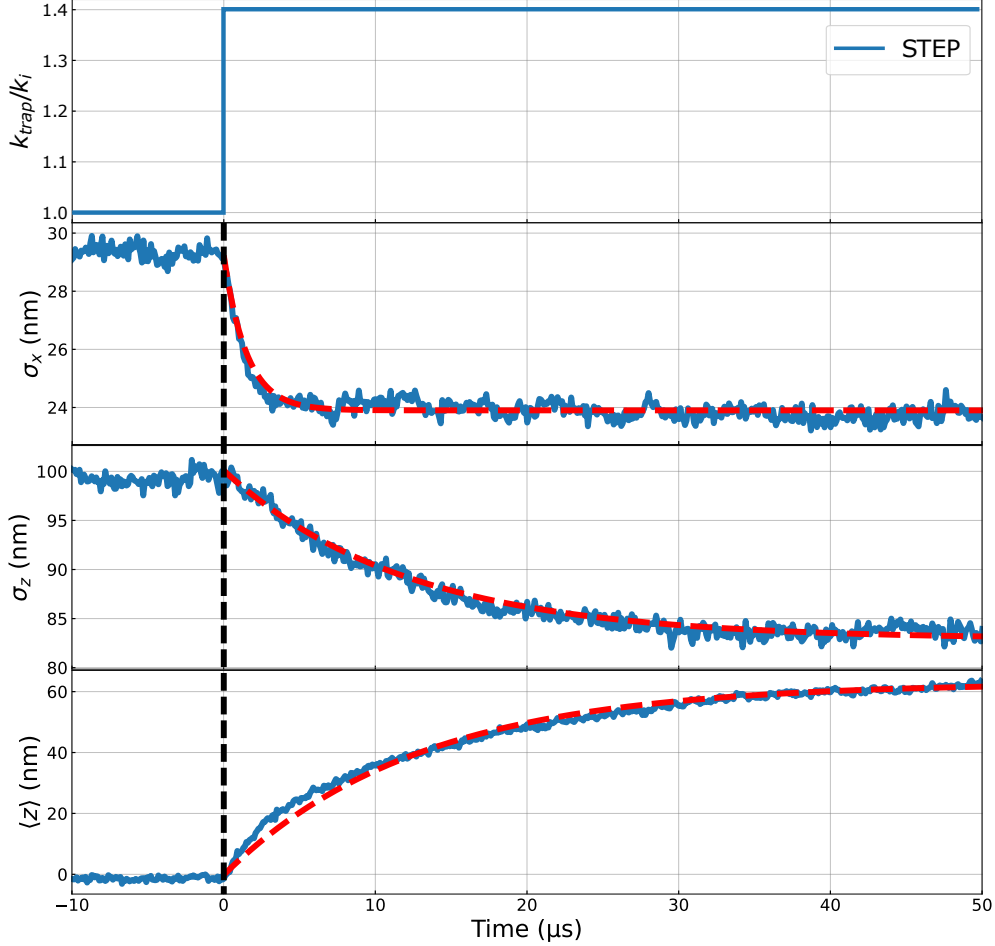


Figure 3.5: Time evolution of k_{trap}/k_i , σ_x , σ_z and $\langle z \rangle$ in the case of an overdamped compression STEP protocol performed at $p_{\text{gas}} = 1$ bar with $\chi = 1.4$. $(\sigma_{z,i}^{\text{eq}}/\sigma_{z,f}^{\text{eq}})^2 = (\sigma_{x,i}^{\text{eq}}/\sigma_{x,f}^{\text{eq}})^2 = 1.4 = \chi$, which shows that the trapping potential is changed by χ along the 3 axes. The transient regime is here characterized by exponential decays with characteristic times Γ/ω_x^2 (respectively Γ/ω_z^2). Due to thermal lensing, the trap is also moved from 60 nm along z -axis. The evolution $\langle z \rangle$ illustrates that relaxation time in the overdamped regime is due to the relaxation in position of our system, t_z being the characteristic timescale needed for $\rho(z)$ to move to the new centre of the trap located at $z = 60$ nm.

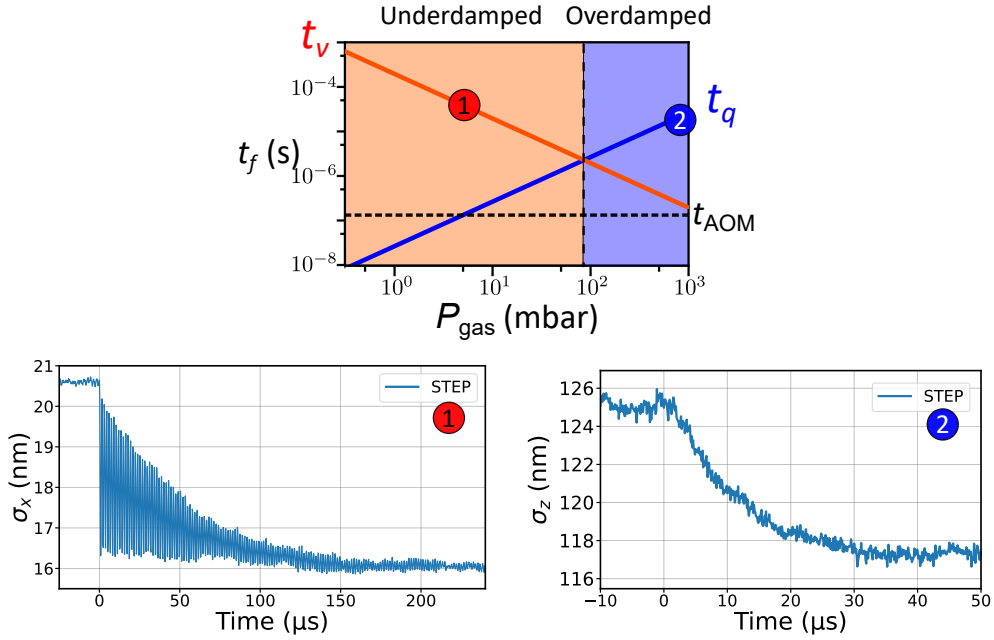


Figure 3.6: Top : domains of underdamped and overdamped regimes for a nanoparticle in a gas. The damping Γ being proportional to p_{gas} , the two characteristic relaxation time $t_q = \Gamma/\omega_q^2$ with $q \in \{x, y, z\}$ and $t_v = 1/\Gamma$ are straight lines in logarithmic scale. Bottom : Experimental realization of relaxations in the two regimes (respectively at 5 mbar and 1 bar), in the case of a compression, highlighting the similarities, with an exponential decay law, and the differences, with the oscillatory evolution in the underdamped regime. The response time of the AOM, $t_{\text{AOM}} \approx 160$ ns, is the characteristic time at which the trapping potential is changed in a STEP protocol.

are clearly defined, at the boundary $t_x \approx t_v$, the interplay between two different timescales leads to original behaviours such as memory effects [127].

The study of these two relaxation regimes underlines the need for protocols allowing to perform states transformation faster than the natural relaxation time of the system, especially for experiments conducted in high vacuum, the relaxation time being inversely proportional to the gas pressure.

3.2 . Shortcuts to equilibrium

In this section, we describe the procedure by which a system can be engineered to reach a new equilibrium state faster than its natural relaxation time. After a short introduction on the theory of Engineered Swift Equilibrium, we look closer at the implementation. We then present our experimental results.

3.2.1 . Principle of ESE protocol

First demonstrated for a trapped particle in the overdamped regime [121], the framework of Engineered Shortcuts to Equilibrium (ESE) has been theoretically extended to the underdamped regime in [125]. We outline here the main elements of this theoretical work.

One should note here that this protocol is designed for a 1D system, while we are working on a 3D system. This aspect will be developed in section 3.3.

An ESE protocol is defined by the compression factor $\chi = k_f/k_i$ introduced previously for the STEP protocol, and a final time t_f at which the system should be at equilibrium in its final targeted state. Without going into the details outlined in [125], the protocol's main idea is to find an appropriate solution for the particle distribution function $\rho(x, v_x, t)$ whose evolution is described by the Kramers equation (eq. (2.39)), a special case of the Fokker-Planck equation. To reach equilibrium at t_f , the evolution of $\rho(x, v_x, t)$ is then steered through the control parameter k_{trap} .

First, the authors propose to find a solution of the form :

$$\rho(x, v_x, t) = N(t) \exp(-(\alpha(t)x^2 + \beta(t)v_x^2 + \delta(t)xv_x)) \quad (3.7)$$

Injected in Kramers equation (2.39), for an isothermal transformation, this leads to a coupled system of equations :

$$\begin{cases} \dot{\tilde{\alpha}} &= 2N_\omega \tilde{\kappa} \tilde{\delta} - 2N_\Gamma \tilde{\delta}^2 \\ \dot{\tilde{\beta}} &= -2N_\omega \tilde{\delta} + 2N_\Gamma \tilde{\beta} - 2N_\Gamma \tilde{\beta}^2 \\ \dot{\tilde{\delta}} &= -N_\omega \tilde{\alpha} + N_\omega \tilde{\kappa} \tilde{\beta} + N_\Gamma \tilde{\delta} - 2N_\Gamma \tilde{\beta} \tilde{\delta} \end{cases}$$

where we introduce the rescaled quantities :

$$\begin{cases} \tilde{\alpha} &= \frac{2k_B T}{k_i} \alpha \\ \tilde{\beta} &= \frac{2k_B T}{k_i} \beta \\ \tilde{\delta} &= \frac{2k_B T}{k_i} \delta \\ N_\omega &= \omega_i t_f \\ N_\Gamma &= \Gamma t_f \\ s &= t/t_f \end{cases}$$

By introducing the auxiliary variable

$$\tilde{\Delta} = \left(\tilde{\alpha} - \frac{\tilde{\delta}^2}{\tilde{\beta}} \right) \tilde{\beta} \quad (3.8)$$

the authors are then able to express $\tilde{\alpha}, \tilde{\beta}$ and $\tilde{\delta}$ as functions of $\tilde{\Delta}$ and its derivative.

An ESE protocol is thus determined by the choice of $\tilde{\Delta}$ and boundary conditions, in particular $\tilde{\alpha}(1) = \tilde{\delta}(1) = \chi$. Moreover, the first two derivatives of $\tilde{\delta}$ are taken to be 0 in $s = 0$ and $s = 1$ to satisfy the continuity of k_{trap} .

The normalized control parameter evolution is then fully defined as :

$$\frac{k_{\text{trap}}}{k_i} = \frac{\dot{\tilde{\alpha}}}{2\omega_i\tilde{\delta}} + \frac{\Gamma}{\omega_i}\tilde{\delta}, \quad (3.9)$$

The authors then use the lower admissible polynomial :

$$\tilde{\Delta}(s) = 1 + (\chi - 1)(35s^4 - 84s^5 + 70s^6 - 20s^7). \quad (3.10)$$

In the rest of the text, we use this implementation. Note that other solutions are possible, for example, by the use of sinusoidal functions:

$$\tilde{\Delta}_{\text{sin}}(s) = \frac{1+\chi}{2} + 9\frac{1-\chi}{16}\cos(\pi s) - \frac{1-\chi}{16}\cos(3\pi s) \quad (3.11)$$

This leads to sensibly the same results in regard to the robustness of the protocol, as we will see in section 3.3.

To sum it up, by this definition, an ESE protocol can theoretically be designed for any positive compression factor χ and any target time t_f , given that we know the initial oscillation frequency ω_i and damping Γ ²

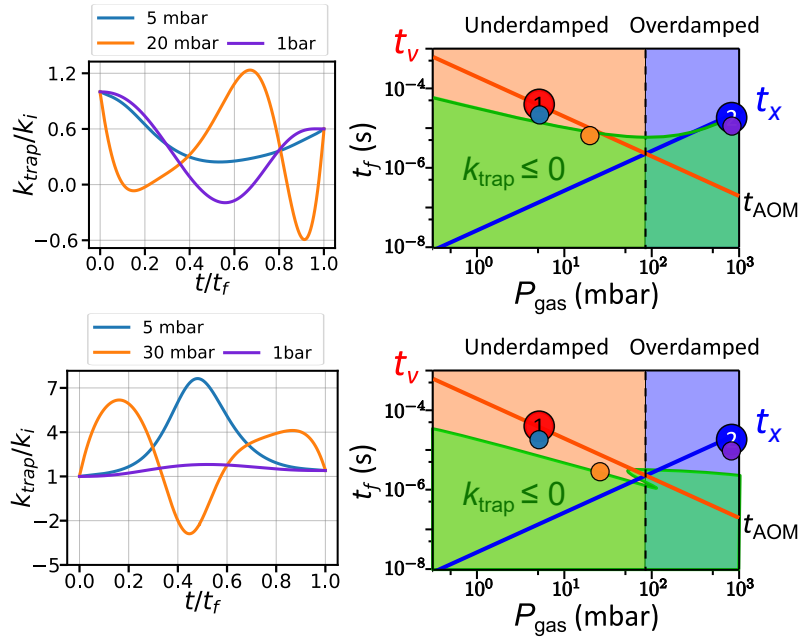


Figure 3.7: Domains of ESE for our system, with expansion protocols (a.) and compression protocols (b.), the green part representing ESE for which $k_{\text{trap}} \leq 0$ transiently. On the left are represented ESE protocols for different pressures.

²Note that, however, the existence of an ESE protocol requires an adequate choice of the Ansatz for the probability density function. For instance, the chosen Ansatz here is not valid in the case of very fast compression [125]. This regime will not be discussed here.

3.2.2 . Implementation

To perform ESE protocols on our system, we generate a time-varying trapping potential, whose stiffness k_{trap} follows the theoretical variation obtained from the previous computation to reach equilibrium at the chosen final time t_f . Due to the trade-off between maximal RF power admissible by the AOM and minimum stiffness necessary to keep the particle trapped, we are limited in the shortest time and the maximal compression/expansion we can perform.

Figure 3.7 summarizes typical ESE protocols that are expected for different damping (*i.e.* gas pressure p_{gas} in our experiment). One should note that for performing some protocols, both in expansion and in compression, the theoretical model leads to transient $k_{\text{trap}} \leq 0$, which poses interesting questions from the experimentalist's point of view. We will address this topic in the following chapter. For now, we will only consider the implementation of ESE protocols with $k_{\text{trap}} > 0$ at all times.

3.2.3 . Experimental results

Overdamped regime

As a first test of our system, we choose to reproduce ESE results in the overdamped regime, which was explored in colloidal systems in [121, 128].

Here, we performed the same compression as in the STEP protocol studied in the previous section, at $p_{\text{gas}} = 1$ bar of the same factor $\chi = 1.4$, but with an ESE protocol of target time $t_f = 8 \mu\text{s}$, shorter than the measured relaxation time along the z axis, $t_z = 11.5 \mu\text{s}$.

As can be seen in the top panel of figure 3.8, k_{trap} reaches far higher values than in the STEP protocol, before going down to the final level. Over the z -axis, σ_z is at equilibrium at t_f , which demonstrates the efficiency of the protocol. As previously observed, thermal lensing in the AOM generates a motion along the z -axis. This effect is seen when considering $\langle z \rangle$, where we observe that at the final time t_f the particle is slightly displaced from the trap centre and slowly relaxes towards its final position $\langle z \rangle = 60$ nm. An observation of σ_x , for which this protocol was not designed, shows that σ_x is forced to follow the variation of k_{trap} , k_x staying proportional to k_z (due to the intrinsic geometry of the beam). The dynamics along x being faster than along z by one order of magnitude (with $t_x = 1.5 \mu\text{s}$), σ_x is yet able to reach equilibrium at a time close to t_f .

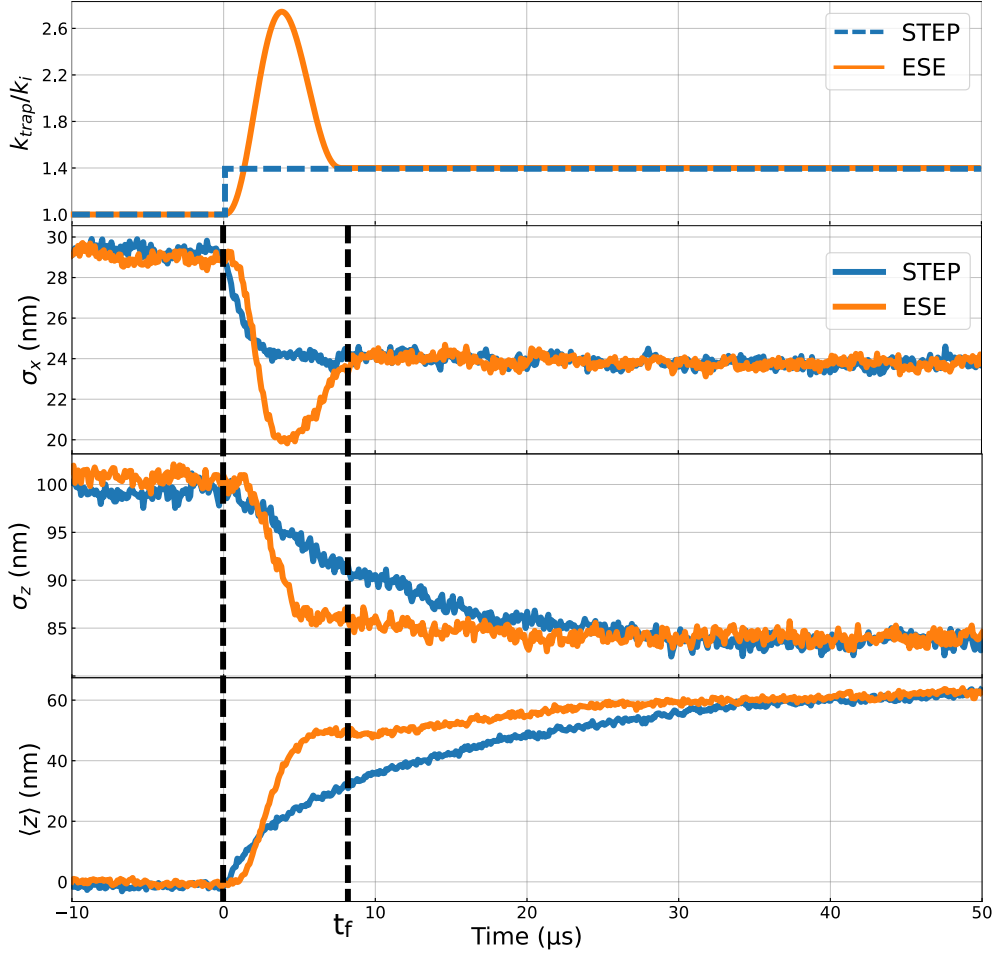


Figure 3.8: Time evolution of k_{trap}/k_i , σ_x , σ_z and $\langle z \rangle$ in the case of an overdamped compression ESE protocol performed at $P_{\text{gas}} = 1$ bar with $\chi = 1.4$. To achieve a faster equilibration at $t_f = 8 \mu\text{s}$ over the z -axis, k_{trap} follows a smoother variation than in the STEP protocol, and reaches at halfway a maximum value almost 3 times bigger than k_i . Over the z -axis, σ_z reaches equilibrium at t_f , proving the efficiency of the ESE protocol. Meanwhile, σ_x follows the variation of the stiffness k_x imposed by the protocol over the 3 axes, and is also at equilibrium at t_f . Considering $\langle z \rangle$, while a first position is reached at t_f at 50 nm, a slow drift is observed that moves the trap towards the equilibrium position observed in the STEP case, at 60 nm. As before, we ascribe this to the thermal lensing due to the AOM.

Underdamped regime

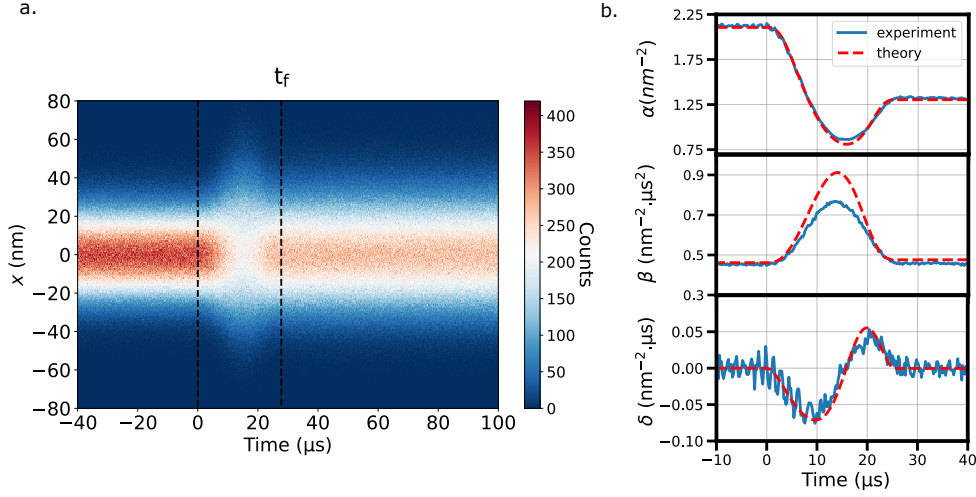


Figure 3.9: a. Time evolution of $\rho(x)$ during an ESE protocol in the underdamped regime, obtained by computing for each time t a histogram from the 2×10^4 positions $x(t)$ (each time trace being re-centered by subtracting its mean value). b. Evolution of the parameters α , β and δ , which are computed from equation (3.2.3) and characterize the full distribution $\rho(x, v_x, t)$. A good agreement between these values and the theoretical ones (red dotted lines) is observed, except for a small discrepancy in β .

Moving on to the underdamped regime, we perform an ESE protocol under the same conditions as for the STEP protocol ($p_{\text{gas}} = 5$ mbar, $\chi = 0.6$), and choose a target equilibration time $t_f = 26$ μs , corresponding to a five-times speed-up compared to the STEP total relaxation time $3t_v = 150$ μs .

Figure 3.9 a. shows the evolution of $\rho(x)$ during the protocol. In comparison with figure 3.2, no oscillations are observable, and the final density $\rho_{f,eq}(x)$ is reached at t_f .

Looking at the time evolution of σ_x , σ_{v_x} and $\langle xv_x \rangle$ pictured in figure 3.10, we confirm that equilibrium is reached in time t_f , and that the experimental curves follow the theoretical ones closely. While the ESE protocol involves the succession of an expansion and a compression in position space, it performs these operations in reverse in velocity space. Moreover, $\langle xv_x \rangle$ stays closer to zero than during the STEP protocol, which means that position and velocity are less correlated. This in turn allows the system to thermalize faster.

From the experimental data, it is also possible to compute the evolution of the parameters α , β and δ used in the definition of the ESE protocol, through the relations :

$$\alpha = \frac{\sigma_{vv}}{2(\sigma_{vv}\sigma_{xx} - \sigma_{xv})}, \quad \beta = \frac{\sigma_{xx}}{2(\sigma_{vv}\sigma_{xx} - \sigma_{xv})}$$

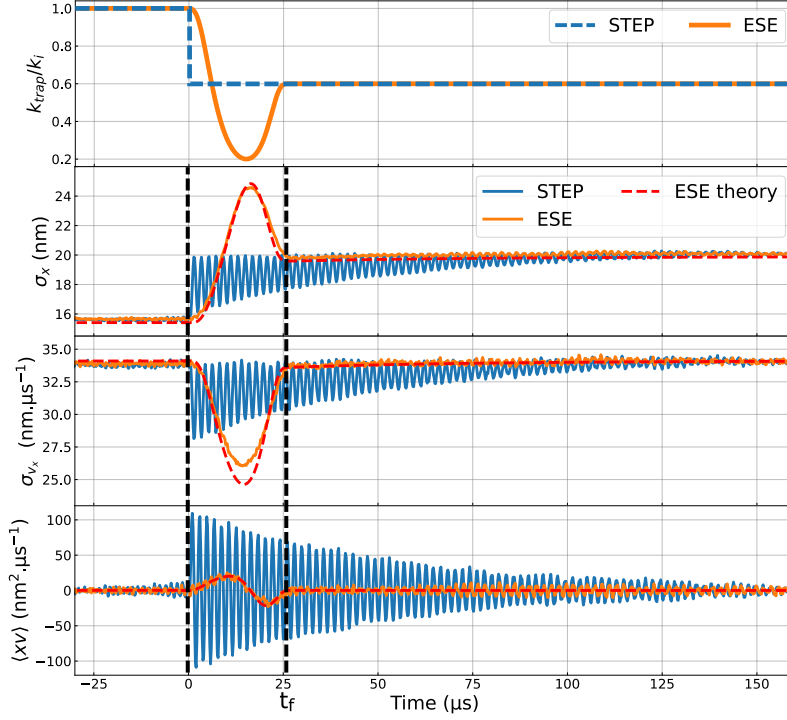


Figure 3.10: Time evolution of k_{trap}/k_i , σ_x , σ_{v_x} and $\langle xv_x \rangle$ in the case of an underdamped expansion ESE protocol performed at $P_{gas} = 5$ mbar with $\chi = 0.6$. To achieve a faster equilibration at $t_f = 26 \mu s$ over the x -axis, k_{trap} follows a smoother variation than in the STEP protocol, and reaches at halfway a minimum value 5 times smaller than k_i . At t_f , σ_x and σ_{v_x} are at equilibrium, in stark contrast with $3t_v \approx 150 \mu s$ with the STEP protocol. Plots of the theoretical evolution of σ_x , σ_{v_x} and $\langle xv_x \rangle$ (red dotted line) show an almost perfect agreement with the experimental data, except for a small discrepancy for σ_{v_x} . In particular, one observed that compared with the STEP protocol, $\langle xv_x \rangle$ stays close to zero, which means that position and velocity are less correlated than in the STEP protocol.

$$\delta = \frac{-\sigma_{xv}}{(\sigma_{vv}\sigma_{xx} - \sigma_{xv})}$$

Comparing these quantities with the theoretical ones (dotted red lines), we observe a very good agreement (except for a small discrepancy in β), which underlines our ability to control and measure the temporal evolution of the full probability distribution $\rho(x, v_x, t)$ defined in equation 3.7.

Finally, we also present in figure 3.11 the compared evolution of the kurtosis of $\rho(x)$ and $\rho(v_x)$ during the STEP and ESE protocols, and verify that they stay close to 3, which confirm that they stay Gaussian along the whole processes, which was a prerequisite for the derivation of the ESE protocol.

These results represent the first realization of ESE protocols in the underdamped regime.

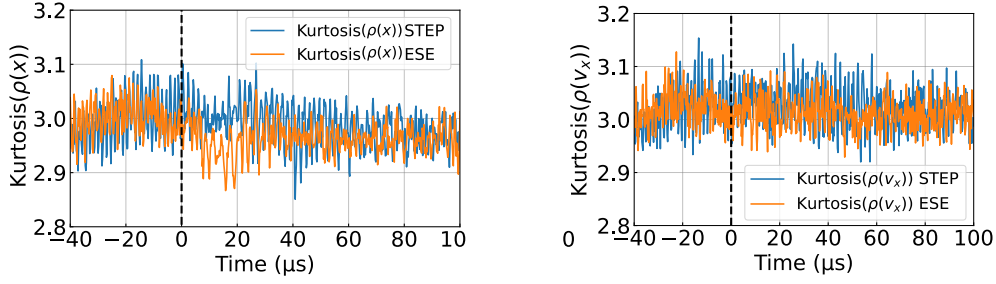


Figure 3.11: Particle probability density kurtosis in position (left) and velocity (right) for a STEP and an ESE protocol. The kurtosis staying close to three demonstrates that the probability density function remains Gaussian at all times.

3.2.4 . Energetics

As mentioned in the introduction, beyond optimizing the time of a state-to-state transformation, another important aspect of such transformations is their energetics, which plays a central role in the efficiency of the transformation. We show here that we can compute the related quantity of heat and work, an important step towards their optimization in the future.

These quantities are correctly treated through the formalism of stochastic energetics [20]. From the time traces of the STEP and ESE protocols in the underdamped regime presented in the precedent sections, it is possible to compute the cumulative heat,

$$\langle Q(t) \rangle = - \int_0^t k(t') \langle xv_x \rangle dt' - \left[\frac{1}{2} m \langle v_x^2 \rangle \right]_0^t = \langle Q_x(t) \rangle + \langle Q_v(t) \rangle, \quad (3.12)$$

and the cumulative work

$$\langle W(t) \rangle = \int_0^t \frac{1}{2} \dot{k}(t') \langle x^2 \rangle dt', \quad (3.13)$$

of our system. The results are shown in figure 3.12. For completeness, we also present the result of compression protocols, performed at the same pressure, for $\chi = 1.4$, in figure 3.13.

In the case of a STEP protocol, the cumulative work is estimated from its theoretical value

$$\langle W(t) \rangle = \frac{\chi - 1}{2} k_B T \quad (3.14)$$

for any positive time.

First, we observe that the ESE protocol is energetically more costly than the STEP protocol, which is the price to pay for accelerating the state-to-state transformation.

Second, in both protocols, we observe that the final heat Q and final W , although close, do not perfectly match. Interestingly, the decomposition of Q into Q_x and Q_v shows that this discrepancy arises from Q_v . It alludes to a few possible explanations :

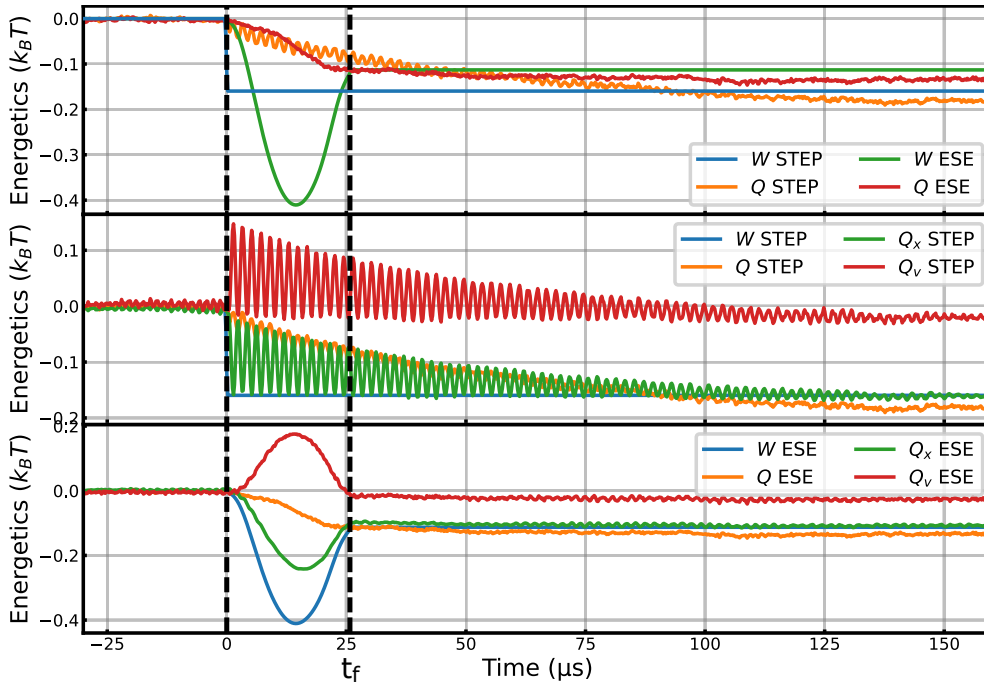


Figure 3.12: Top : Work W and heat Q computed for expansion STEP and ESE protocols in the underdamped regime ($p_{\text{gas}} = 5$ mbar). Middle and bottom : decomposition of Q into Q_x and Q_v for both protocols, stressing out the fact that the discrepancy between the final W and Q stems from Q_v .

- The velocity being obtained by differentiating noisy time traces, computing Q is more prone to errors, which accumulate over time.
- Our hypothesis that we perform an isothermal transformation is not valid, and by changing the power of the trapping laser, we could also influence the local environment of the particle, a situation reminiscent of hot Brownian motion [90].
- Some other process is at play and slightly modifies the dissipation of the system.

Finally, the ability to optimize fast isothermal expansions/compressions in the underdamped regime paves the way for the realization of nano heat engines. Indeed, the power generated by such a motor during a cycle of duration τ is $P = -W/\tau$. To realize efficient heat engines, it is thus necessary to minimize the time of each cycle, as well as maximize W [129, 130, 131].

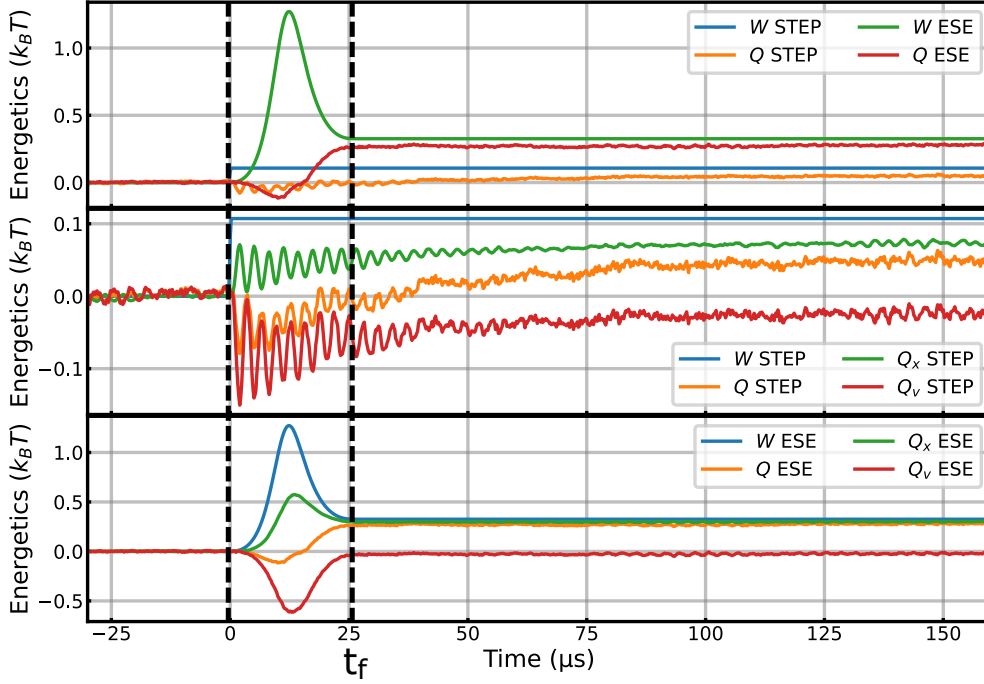


Figure 3.13: Top : Work W and heat Q computed for compression STEP and ESE protocols in the underdamped regime ($p_{\text{gas}} = 5$ mbar). Compared with the expansion protocol of figure 3.12, the discrepancy is much more important on Q .

3.3 . Robustness of ESE protocols

In control theory, it is of the essence to be able to define which tolerances are admissible for a given procedure to achieve the intended result. Until now, we studied ESE protocols designed for a given frequency and relaxation time. In this last section, we study how they fare under relaxed constraints. From another point of view, our work has until then been interested with protocols initially designed for 1D systems. A levitated particle has three degrees of freedom for its centre of mass, and there is a growing interest in the community to design protocols able to control multi-modes systems [132].

We thus propose to study the effect of ESE protocols designed for the x -axis on the z -axis. Figure 3.14 presents the evolution of σ_x and σ_z under two different ESE protocols in the underdamped regime at $p_{\text{gas}} = 5$ mbar :

- The first is the protocol studied until now, with $\chi = 0.6$ and $t_f = 26$ μs .
- The second being a faster protocol, with $t_f = 7.75$ μs , and a relaxed condition $\chi = 0.75$.

For these two protocols, the difference in angular frequencies between the x and z axes is such that $\omega_x/\omega_z \approx 3.4$. Yet, for the first protocol, we observe that applying the ESE protocol designed for ω_x performs surprisingly well over the

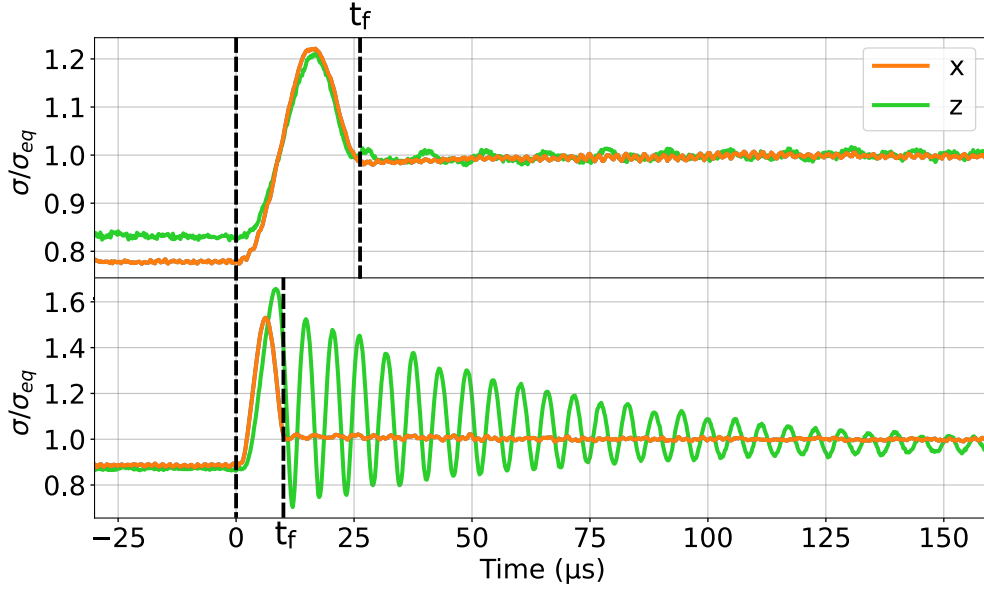


Figure 3.14: Comparison of the evolution of σ_x (orange) and σ_z (green) for two different ESE protocols performed at $P_{\text{gas}} = 5$ mbar. For both figures, $\omega_x/\omega_z \approx 3.4$. Top : ESE protocol with $\chi = 0.6$ and $t_f = 26$ μs . Bottom: ESE protocol with $\chi = 0.75$ and $t_f = 7.75$ μs . While the first protocol achieves equilibrium at t_f on both axes, the second protocol, faster, achieves equilibrium at t_f over the x -axis, hence producing a 17-fold reduction in equilibration time, but drives the z -axis out of equilibrium.

z -axis (due to a degraded SNR over z , a small offset is visible between the two initial states, but this does not affect the present discussion), bringing both axes to equilibrium at t_f (the same observation could be done for y , for which $\omega_x/\omega_y \approx 1.3$). In comparison, while the second protocol efficiently performs equilibration over the x -axis 17-times faster than the natural relaxation rate, it drives the system out-of-equilibrium over the z -axis. After t_f , the system relaxes to equilibrium, dissipating energy to the bath through damped oscillations at $2\omega_z$, as observed for the STEP protocol, with a characteristic relaxation time $t_v = 1/\Gamma$.

To address more quantitatively the robustness of a protocol defined for a reference system, we propose to characterize how close from equilibrium ends an arbitrary system submitted to this protocol.

To characterize this distance to equilibrium between the system distribution at the end of the protocol, $p(x, v)$ and the equilibrium distribution $q(x, v)$, we use the Kullback–Leibler divergence $D(p||q)$. This estimator is defined as

$$D(p||q) = \iint dx dv p(x, v) \ln \left(\frac{p(x, v)}{q(x, v)} \right), \quad (3.15)$$

and can be seen as a statistical distance between the two distributions p and q .

Here, we are interested in the efficiency of an ESE protocol defined for a system of natural frequency ω_{ref} applied to a system of frequency ω . We thus determine

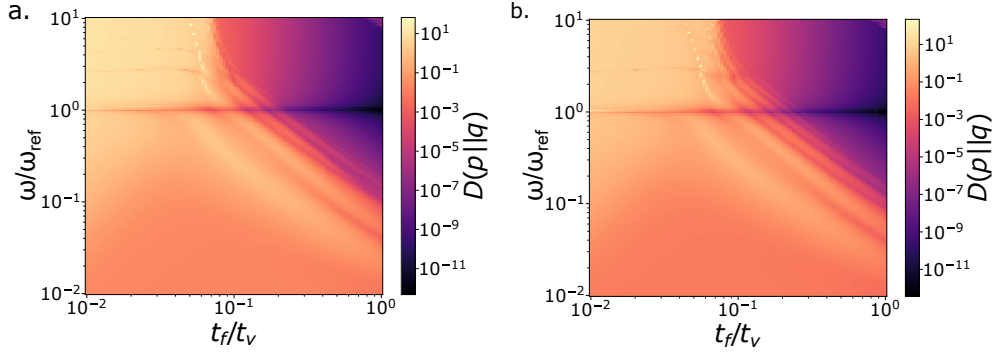


Figure 3.15: Kullback-Leibler divergence for the ESE protocols as a function of the final time t_f and the frequency difference $\omega/\omega_{\text{ref}}$
a. Computed for ESE protocols used in this chapter and defined with the polynomial 3.10.
b. Computed for ESE protocols with the alternative definition 3.11.

the ESE protocol corresponding to a system of natural frequency ω_{ref} and damping Γ , and for a final time t_f . From the set of coupled equations 3.2.1, we then numerically compute the evolution of the distribution

$$\rho(x, v_x, t) = \frac{\sqrt{4\alpha(t)\beta(t) - \delta(t)^2}}{2\pi} e^{-\alpha(t)x^2 - \beta(t)v^2 - \delta(t)xv} \quad (3.16)$$

of a system of frequency ω submitted to the protocol (with the same damping and the same final time). We thus compute the final value of the distribution $p(x, v) = \rho(x, v_x, t_f)$

By considering the equilibrium target distribution :

$$q(x, v) = \rho_{\text{eq}}(x, v_x, t_f) = \frac{m\omega\chi}{\pi k_B T} \exp\left(-\chi \frac{m\Omega_i^2}{k_b T} x^2 - \frac{m}{k_b T} v^2\right) \quad (3.17)$$

one can show that the Kullback-Leibler divergence writes:

$$D(p||q) = \frac{1}{2} \ln \left[\frac{4\alpha\beta - \delta^2}{4\alpha^{\text{eq}}\beta^{\text{eq}}} \right] - (\alpha - \alpha^{\text{eq}})\sigma_{xx}^f - (\beta - \beta^{\text{eq}})\sigma_{vv}^f - \delta\sigma_{xv}^f \quad (3.18)$$

where we can reverse the equations 3.2.3 to obtain

$$\begin{cases} \sigma_{xx} = \langle x^2 \rangle = \frac{2\beta}{4\alpha\beta - \delta^2} \\ \sigma_{vv} = \langle v^2 \rangle = \frac{2\alpha}{4\alpha\beta - \delta^2} \\ \sigma_{xv} = \langle xv \rangle = \frac{-\delta}{4\alpha\beta - \delta^2} \end{cases}$$

The Kullback-Leibler divergence for the ESE protocols as a function of the final time t_f and the frequency difference $\omega/\omega_{\text{ref}}$ is shown in figure 3.15-(a).

A couple of interesting features are observed. First, the protocols are more robust for moderate acceleration, as discussed for experimental data in the previous subsection. Then, the evolution of the Kullback-Leibler divergence is non-monotonic, and we observe a coupling between frequency and final time impacting protocol robustness. As a consequence, for a given system frequency ω , tuning the final time to reach a state closer to equilibrium could be interesting.

To discuss the universality of these features, we apply the same procedure for a protocol defined by using the sinusoidal decomposition for the Δ function (3.11) instead of the polynomial expression (3.10) we used for our experiments.

The results are presented in figure 3.15-b., demonstrating the same properties, with a worse protocol efficiency for decreasing final time and the non-monotonic behaviour of the Kullback-Liebler divergence.

Finally, we demonstrate that Kullback-Leibler divergence could be a strategy to characterize the robustness of state-to-state protocols. If the two proposed protocols share the same limitation to moderate speed-up, our strategy could be used to discuss other protocols, both for fast equilibration and work optimization.

3.4 . Conclusion

In this chapter, we have explored the temporal control of the dynamics of a levitated particle, by exploring first the natural relaxation timescales involved in the overdamped and underdamped regime. Then, we showed that Engineered Swift Equilibrium protocols makes it possible to perform fast transformations between arbitrary equilibrium states. We finally explored the robustness of these protocols and their application to multi-modes systems.

Coupled with recent advances in thermal bath engineering [55] and fine temperature control [64], this work opens up the possibility to implement nano-heat engines [119, 122], by allowing to optimize their power and efficiency through controlled yet swift transformations.

Three limits of this approach must be stressed :

- To achieve faster transformations in the underdamped regime, it is necessary to find a way to implement transiently locally null or negative stiffness, which is not possible as long as our approach is limited to one Gaussian trapping beam.
- The limiting factor in performing a fast compression is the maximal stiffness reached in the overshoot of the ESE protocol. This pleads to choose an initial equilibrium state with the smallest stiffness achievable to maximize this ratio.
- To perform more general transformations, and in particular to realize non-Gaussian states, it is necessary to generate non-harmonic potentials.

These three endeavours are the matter of the next chapter.

4 - Generation and characterization of arbitrary potentials

The climate system is a coupled non-linear chaotic system, and therefore the long-term prediction of future climate states is not possible. Rather the focus must be upon the prediction of the probability distribution of the system's future possible states by the generation of ensembles of model solutions.

— IPCC Working Group 1, CLIMATE CHANGE 2001: THE SCIENTIFIC BASIS (2003)

While Gaussian distributions are ubiquitous, other distributions are routinely encountered and contribute to the richness of physics. In the previous chapter, I addressed the essential topic of state-to-state transformations.

The extension of this work to non-harmonic cases, while challenging theoretically and experimentally, opens the way to intriguing questions on the evolution of distributions in arbitrary potentials and timings [133] or on optimal diffusion [134]. The control of distributions also offers unique opportunities to generate out-of-equilibrium states that could provide state erasure with power consumption below the Landauer limit [56] or toward tests of general stochastic thermodynamics theorems [135]. Beyond nano-thermodynamics, this question is also central in general for optomechanics, where the control of distributions beyond the Gaussian case is critical for the development of quantum optomechanics [136, 137, 138]. Finally, this could also serve as a resource to increase the sensitivity of levitated particle force sensors [139, 140]. Hence, while other approaches seek to precisely determine the influence of the Duffing terms introduced in chapter 2 section 2.1 for levitated optomechanics [83], our goal is here to use optical potentials with strong nonlinearities (*i.e.* anharmonicities) to generate arbitrary non-Gaussian distributions, in a way reminiscent of previous work in the field of numerical simulations [141, 142].

In this chapter, I first demonstrate the generation of arbitrary 1D optical potentials for levitated particles. I then discuss the characterization of these potentials and the related challenges induced by the measurement non-linearities of the particle dynamics detection (*i.e.* the detectors signals are not simply proportional to the particle positions). Finally, I show that the use of advanced statistics methods based on Kalman filters allows an improved reconstruction of the potentials.

4.1 . Generation of arbitrary potentials

4.1.1 . Beam shaping of focal fields

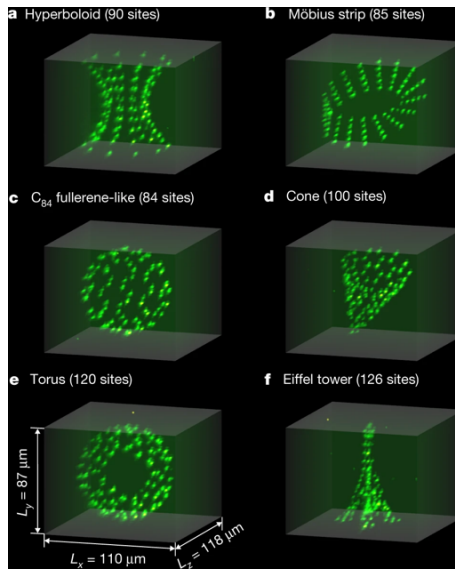


Figure 4.1: Arbitrary 3D arrays of neutral atoms generated by creating a phased-pattern beam by using the Gerchberg–Saxton algorithm with an SLM (from [144])

Many approaches have been proposed and demonstrated for the generation of complex focal fields. The ability to shape beams is indeed a requirement for many experiments, in particular in nanomechanics and in cold atoms. A recent review of techniques used in the latter can be found in [143].

First, a complete control of the incoming optical field can be achieved by using a spatial light modulator (SLM) to modulate the phase or the amplitude of the field. To do so, one usually compute a holographic mask, which encoded on the SLM will act as a diffractive optical element. A common application is the generation of arrays of optical tweezers, that have been used to trap hundreds of atoms in 2D [34] or 3D [144] (Figure 4.1). Such systems also allow to trap multiple particles to study optical binding forces, in colloids [110] and more recently in vacuum [111]. SLM also allows one to generate non-Gaussian beam profile, from continuous optical potentials [145], to various complex beams. For instance, recent works demonstrated the realization of Bessel beams [146], Airy beams [147], dark focus beams [148]. Along the same lines, in biophysics, inversion of the Debye-Wolf integral (equation 2.12) is performed to generate aberration-corrected illumination volumes [149, 150]. While allowing impressive feats such as pictured in figure 4.1, the use of SLM is limited in terms of temporal resolution, the highest frame rate achievable being of the order of 250 Hz. Another promising system, with very close applications, is the use of Digital Micromirror Devices (DMD), with frame rate up to a few tens of kHz [151, 152]. This represents a noticeable improvement over SLM, but is still at least one order of magnitude lower than our system dynamics. Besides, the unique control allowed by SLM or DMD comes at the cost that the generation of time-varying optical potentials requires advanced algorithms for the

computation of holograms. Also, spurious interference effects and speckle may make the generation of clean continuous optical potentials challenging [134].

A second approach to generate arbitrary potentials, known as optical painting or time-shared optical traps, consists in moving a single Gaussian beam faster than a characteristic time of the system, so that it is subjected to a force which derives from the time-averaged field intensity. Originally used for the manipulation of bacteria [153], and later used for colloids [154] this approach seems to gain recently more interest in the BEC community [155, 156]. One limitation is the trade-off between the scanning rate and the depth of the resulting time-averaged potential.

A third approach consists in generating a virtual potential. By monitoring in real time the position of the system, a feedback loop applies a force at each time step which emulates the existence of a real optical potential. This approach was successfully used in colloidal experiments [157, 158, 128]. Until recently, this technique was mostly used in overdamped systems, where the dynamics is slow enough to perform the necessary feedback at a sufficiently fast rate without being hindered by noise and drifts. These issues were overcome in [159] in the case of an underdamped cantilever to create a controllable double-well potential and investigate Landauer's bound. However, the dynamics of this system is of the order of the kHz, *i.e.* two orders of magnitude lower than ours. An alternative approach was recently demonstrated on levitated particles by controlling the effective system damping rather than the force applied to the particle [160]. Nevertheless, virtual potentials have several limitations. First, as any feedback approach, its quality is limited by the speed and the quality of particle position acquisition. Then, there is a risk that the continuously adapting feedback force biases the dynamics of the particle, by automatically erasing contributions that are not taken into account in the theoretical model used to derive it.

All these considerations justify the use of another approach, developed in the following section.

4.1.2 . 1D arbitrary potential from single beams superposition

We chose to follow the approach proposed in the reference [161] to generate an arbitrary potential as a combination of beams diffracted through the AOM by a sum of driving frequencies.

As discussed in chapter 2, the AOM allows to precisely position a single Gaussian trap at the objective focus by tuning the driving frequency f_{AWG} . By driving the AOM with a multi-frequency RF wave, it is thus possible to generate a 1D continuous potential from the superposition of individual Gaussian traps.

The idea behind this approach is then to first compute a decomposition of the targeted potential as a sum of overlapping Gaussian beams, which correspond to individual laser beams centred along different positions $x_{0,n}$ and with depth $U_{0,n}$.

The signal provided to the AOM is then

$$V_{\text{AWG}} = \sum_{n=1}^N V_n^0 \sin(2\pi f_{\text{AWG},n} t + \varphi_n). \quad (4.1)$$

In the focal plane of the trapping objective, the potential generated by the associated N beams is then :

$$U_{\text{opt,tot}}(x) = \sum_{n=1}^N U_{0,n} e^{-\frac{2(x-x_{0,n})^2}{w_0^2}}, \quad (4.2)$$

where the values $U_{0,n}$ are related to V_n^0 and $x_{0,n}$ to $f_{\text{AWG},n}$ by the calibration procedure described in the chapter 2 (section 2.3.2). We note that by construction, the AOM imposes a frequency shift of $f_{\text{AWG},n}$ to each of the N optical beams. So we will observe optical beating between these different beams at frequencies $\Delta f_{\text{AWG}} = f_{\text{AWG},i} - f_{\text{AWG},j}$. To keep the particle trapped, it is important that this beating remains at frequencies large compare to the particle dynamics. We thus impose $\Delta f_{\text{AWG}} > 500$ kHz, limiting the distance between two consecutive beams at the focus to 50 nm. Also, the phases φ_n may be chosen to limit the interferences between the N RF signals in the AOM [35]. However, this point is not relevant for $N = 2$ that will be discussed in the next section.

Figure 4.2 recapitulates the procedure. Here, the target potential (red dotted line) of negative stiffness is realized through the superposition of two laser beams, located at symmetric positions along the origin of the x -axis (which corresponds to a driving frequency of 115 MHz). To create them, we drive the AOM with two different frequencies generated by the AWG (here, 111 and 119 MHz). This in turn generates two diffracted beams at different angles θ_1 (resp. θ_2), which are related to x_1 (x_2) through the relation (2.45) detailed in chapter 2.

As a first proof of concept, figure 4.3 presents the realization of four optical potential with a 532 nm laser : a broad harmonic potential, a broader potential, a flat top potential and a large double-well potential. As discussed previously, we first compute the best set of Gaussian beams (dotted black) to match the target potential (dotted blue). The generated sum is then shown in red.

As mentioned earlier, to achieve this experimentally, it is then crucial to generate Gaussian beams with the right intensity and position. For that, we use the calibration procedure detailed in section 2.3.2 and presented in figure 2.11, that provides for each driving frequency f_{AWG} the efficiency of the AOM as well as the beam position.

The resulting potentials are then imaged with a camera, demonstrating the viability of the approach.

To go further, and verify that the optical potential seen by a trapped particle is the one expected, we conduct a simpler experiment using only two beams. Besides the technically simpler approach of using only two driving frequencies, this provides

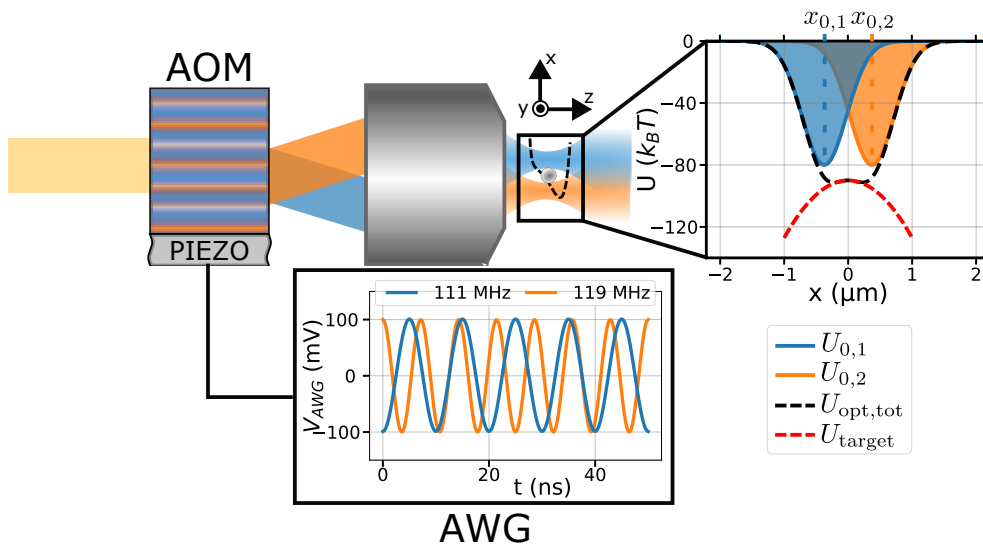


Figure 4.2: Principle of sum of Gaussian beam generation. To generate tailored potentials, an arbitrary waveform generator (AWG) is used to generate simultaneously a sum of sines at different frequencies around the central working frequency of the acousto-optic modulator (AOM). The AOM then deflects as many first order beams, which are then combined through a double telecentric system (not pictured) to the focus of the trapping microscope objective. The resulting sum of N beams allows for a great flexibility in the shape of the target potential, which can be locally negatively curved, periodic, asymmetric, depending on the intensity (controlled by the amplitude $V_{AWG,i}$ of the sine) and position (controlled by the frequency $f_{AWG,i}$). For clarity, we depicted here the case $N = 2$.

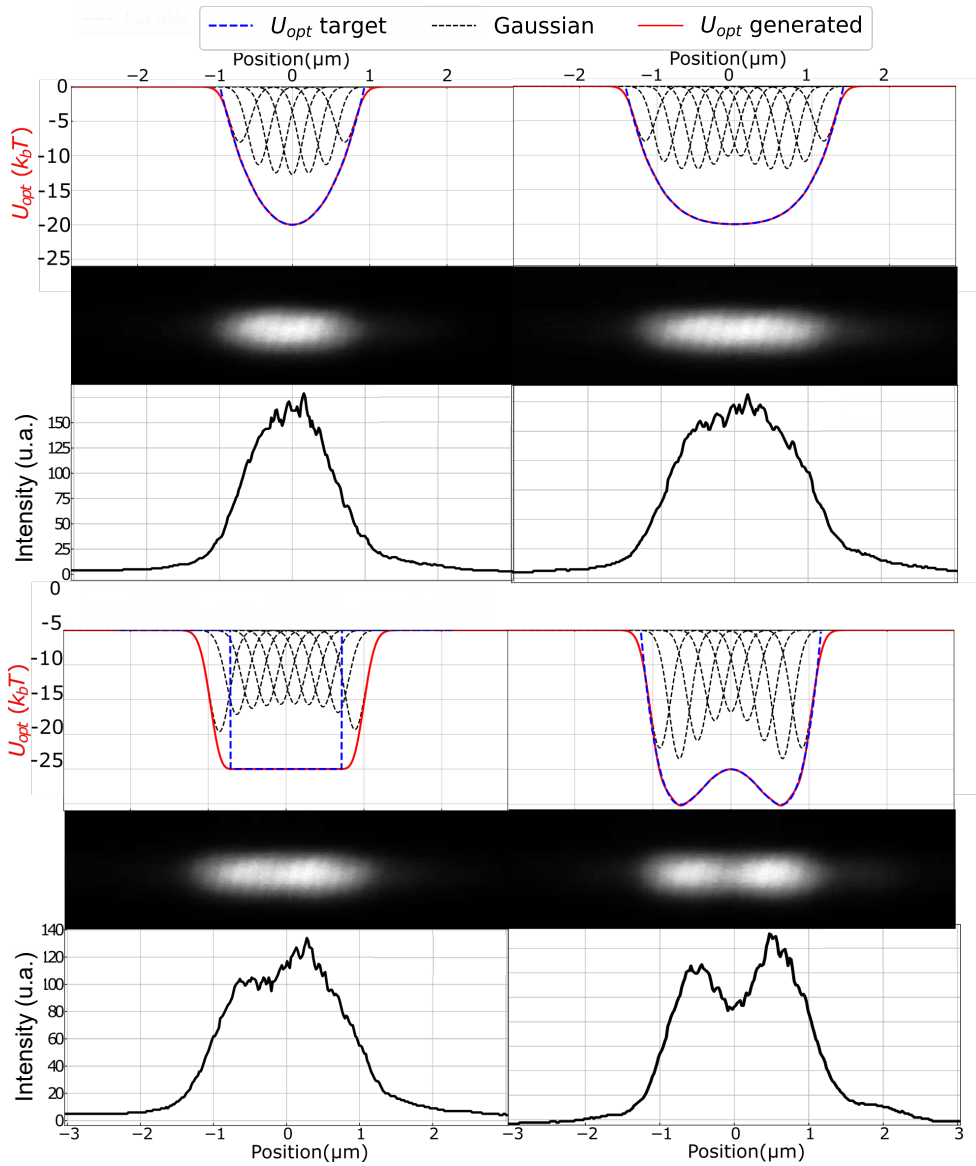


Figure 4.3: Generation of arbitrary potentials, with simulated potentials (top) and the resulting intensity imaged on a camera (bottom). The generated potentials follow approximately the expected shape.

a unique way to tune the potential from harmonic to bistable through a fully quartic potential, by controlling the distance between the two beams.

In the rest of this chapter, we thus demonstrate that our experimental approach allows such a control. We then identify some technological locks that have to be addressed to fully benefit from the high degree of control gained on the potential.

4.1.3 . Control of potential nonlinearities in a dual beams configuration

Assuming that the gradient force is the dominating force, we have shown in the chapter 2 that the optical potential is proportional to the optical field intensity at the objective focus. Consequently, a single beam potential, centred on position x_0 , writes:

$$U_{\text{single}}(x) = U_0 \left(1 - e^{-2\left(\frac{x-x_0}{w_{0x}}\right)^2} \right), \quad (4.3)$$

where w_{0x} is the focused Gaussian beam waist.

The sum of two such beams, located at x_0 and $-x_0$, is then given by :

$$U_{\text{opt}}(x) = U_{\text{single}}(x + x_0) + U_{\text{single}}(x - x_0) \quad (4.4)$$

$$= U_0 \left(2 - e^{-2\left(\frac{x-x_0}{w_{0x}}\right)^2} - e^{-2\left(\frac{x+x_0}{w_{0x}}\right)^2} \right) \quad (4.5)$$

$$= U_0 \left(2 - e^{-2\left(\frac{x}{w_{0x}}\right)^2} e^{-2\left(\frac{x_0}{w_{0x}}\right)^2} \left(e^{-2\frac{2xx_0}{w_{0x}^2}} + e^{2\frac{2xx_0}{w_{0x}^2}} \right) \right) \quad (4.6)$$

$$= U_0 \left(2 - e^{-q^2/2} e^{-q_0^2/2} (e^{-qq_0} + e^{qq_0}) \right) \quad (4.7)$$

where we introduced $q = 2\frac{x}{w_{0x}}$ and $q_0 = 2\frac{x_0}{w_{0x}}$.

From this expression, we can derive the leading terms of the potential curvature. By performing a Taylor expansion in q of this expression around local minima, we can write $U_{\text{opt}}(x)$ as

$$U_{\text{opt}}(x) = 2U_0 \left(1 - e^{-2\left(\frac{x_0}{w_{0x}}\right)^2} (1 + \alpha_x(q_0)x^2 + \beta_x(q_0)x^4) \right) \quad (4.8)$$

The terms α_x and β_x are respectively the quadratic and quartic (*i.e.* Duffing) terms of U_{opt} , defined by :

$$\alpha_x(q_0) = \left(\frac{q_0^2}{2} - \frac{1}{2} \right) \left(\frac{2}{w_{0x}} \right)^2 \quad (4.9)$$

and

$$\beta_x(q_0) = \left(\frac{q_0^4}{24} - \frac{q_0^2}{4} + \frac{1}{8} \right) \left(\frac{2}{w_{0x}} \right)^4 \quad (4.10)$$

with roots $x_0 = \frac{w_{0x}}{2}$ for α_x and $x_0 = \frac{\sqrt{3 \pm \sqrt{6}}}{2} w_{0x}$ for β . The variations of these expressions is presented on figure 4.4, as well as some selected potentials.

We can in the same way derive the values of α and β for y and z , which are:

$$\alpha_{y/z}(q_0) = -\frac{1}{2} \left(\frac{2}{w_{0y/z}} \right)^2 \quad (4.11)$$

and

$$\beta_{y/z}(q_0) = \frac{1}{8} \left(\frac{2}{w_{0y/z}} \right)^4 \quad (4.12)$$

For $q_0 > 1$, expressions can also be obtained numerically. For the following, assuming a harmonic approximation leads to:

$$k_i(q_0) = -4U_0 e^{-\frac{q_0^2}{2}} \alpha_i(q_0) \quad (4.13)$$

for $i \in \{x, y, z\}$. This expression allows us to determine approximates of the harmonic frequencies f_{0x} , f_{0y} and f_{0z} . Note that a complete derivation of the exact shape of the PSD for arbitrary nonlinearities, given by β_i and terms of higher orders, remains challenging [162, 81].

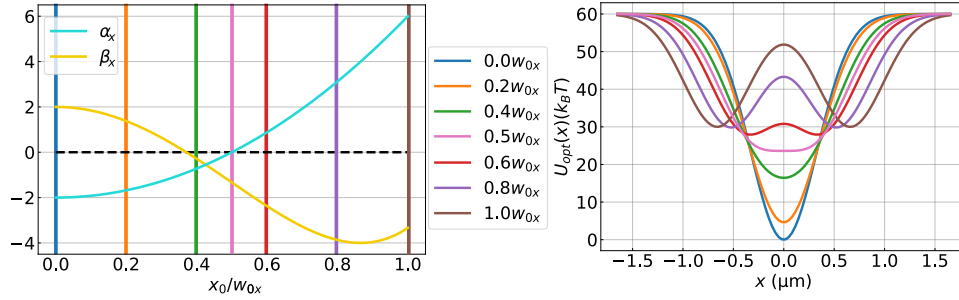


Figure 4.4: Evolution of the nonlinearities of dual beam potentials. For $x_0 = w_{0x}/2$, a perfectly quartic potential is generated (pink). Beyond this value, α becomes positive. In turn, the stiffness of the potential is locally negative, meaning that the potential is repulsive in its center.

By controlling the separation of the two beams, it is thus possible to control the nonlinearities of the potential up to the quartic terms, which makes our platform an ideal testbed for their study.

Experimental realization of this is presented in figure 4.5. We record the 3D dynamics of the particle for different separation between the two beams. We used the calibration data presented in figure 2.11 to ensure that the laser power delivered in two beams is identical, and that the beams are located symmetrically around the reference beam (which corresponds to an AOM driving frequency of 115 MHz). This is crucial, as any imbalance between the two beams will result in an asymmetric distribution, or equivalently in an optical potential with unwanted nonlinearities.

To get an estimate of the real displacement of the particle, the recorded time-traces are rescaled using a constant calibration factor $c_{xx,0}$ for all dataset. We

compute this calibration factor as the sensitivity of the measurement for a trap at the origin $x_0 = 0$, using the procedure described in the section 2.4.2. As we will see, this approximation is legitimate only as long as the particle stays close to the origin.

A natural solution to characterize the potential is to use its relation to the probability density of the particle (see section 2.2.3):

$$\rho(x) = \rho_{x,0} e^{-\frac{U(x)}{k_B T}}. \quad (4.14)$$

We estimate the particle probability density by histogramming the time traces associated with the x motion of the particle (Figure 4.5-b.), estimated in the linear approximation $\tilde{x} = S_x/c_{xx,0}$ as explained. The associated effective potentials are shown in figure 4.5-a. and c. The difficulty to characterize the experimental distributions is readily visible in this figure.

To make the reading easier, we separate the data in two categories : the first 10 acquisitions, where $\Delta x_0 = 2x_0$ varies between 50 and 500 nm, and the 10 last, where it goes from 550 to 1000 nm.

The first batch of distributions (panel a.) presents a clean variation from peaked Gaussian (with no noticeable change for the first ones) to broader ones. Accordingly, the related potentials seem close to harmonicity.

On the contrary, the distributions presented in panel c. differ significantly from one another. Starting with fat-tailed distributions, we reach for $\Delta x_0 = 650$ nm (red) an almost flat potential, whose distribution is quite asymmetric. Pushing the separation of the two beams further, they completely separate, resulting in a double-well potential. The first truly bistable potential (for $\Delta x_0 = 750$ nm, brown) is markedly asymmetric, with a distribution 5 times more peaked on the left side than on the right side. An important feature of this potential is its negative curvature. Alas, one can already observe that this negative curvature does not seem well defined or symmetric, which is a prerequisite for their use for ESE protocols. The next potential at $\Delta x_0 = 800$ nm (pink) fares a lot better in this regard, both sides of its distribution having similar weights. The two wells seem to be separated by around 250 nm, which is far less than Δx_0 .

While the inter-wells distance is physically expected to be slightly smaller than the distance between two overlapping Gaussian beams, this discrepancy hints at a limitation of our setup evoked in the section 2.4.3): the nonlinearity and non-bijectionality of S_x , which also explains why traps seem to be moving back to the centre.

Thus, our detection's non-linearities prevent appropriate calibration of the optical trapping potentials. Consequently, the potentials plotted in figure 4.5 are only effective and do not represent an actual physical situation (especially for large Δx_0). This approach does not allow us to validate our approach for generating non-linear potentials. To go further, we use an alternative characterization method and compute the PSD of the time traces of the particle dynamics,

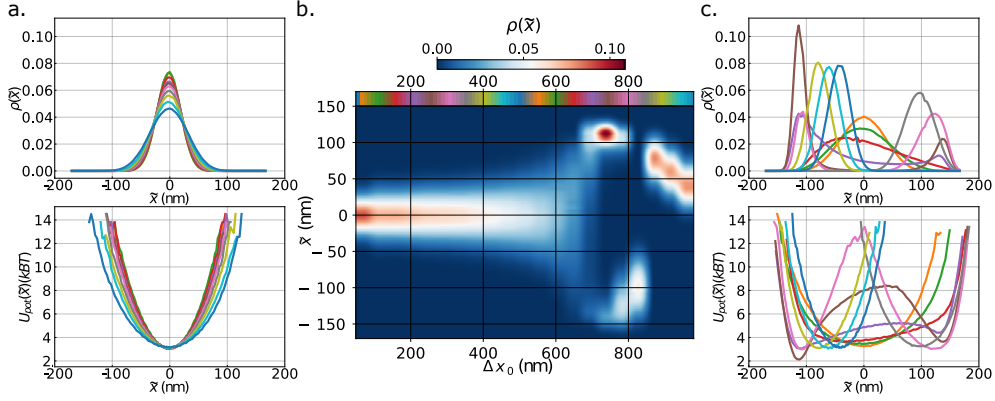


Figure 4.5: Experimental realization of arbitrary distribution, performed by moving two beams from a 50 nm separation to 1 μm by 50 nm steps, at $P_{gas} = 10$ mbar. Distributions and potentials are computed by using the linear approximation $\tilde{x} = S_x/c_{xx,0}$. The coloured top bar of the central figure indicates the position of the distributions plotted on the left and right sides, the separation between the two sides occurring at $\Delta x_0 = 500$ nm. We notice that for potentials defined over a large spatial range, distributions and potentials appears completely deformed, a consequence of the nonlinearity of the measure highlighted in chapter 2)

as shown in figure 4.6. If the PSDs are also affected by the detection's nonlinearities (deformation of the peaks, cross-coupling between the measurement axes, appearance of higher order harmonics), at least the natural frequencies are preserved. This allows us to compare the value of the frequencies f_{0x} , f_{0y} and f_{0z} obtained from the fits of the PSD to the theoretical predictions of equation 4.13. As shown in figure 4.6, an excellent agreement is obtained by fitting the model to the data, with as free parameters, the initial frequencies of the traps (at $x_0 = 0$) and the beam widths w_{0i} . A collapse of the x -frequency is observed around 700 nm (close to the purple distribution in figure 4.5 c.). This separation of beams corresponds thus to the waist w_{0x} , a value close to the one obtained from the simulation in section 2.1 (as a reminder, in figure 2.4, $w_{0x} = 660$ nm). After the separation, the particle oscillates in one of the two wells of the bistable potential, finally reaching $f_{0x}(\Delta x_0 = 1000 \text{ nm}) = 110 \text{ kHz}$, such that $f_{0x}(\Delta x_0 = 50 \text{ nm})/f_{0x}(\Delta x_0 = 1000 \text{ nm}) = \sqrt{2}$, which is expected since the trapping power is now divided between two far separated beams.

The excellent agreement observed with the model then proved that we could control the non-linearities of the optical trap. Nevertheless, using the PSD is relatively indirect in measuring the particle dynamics and could prevent advanced analysis of these dynamics. It is then of prime interest to extend the linear range of our measurement scheme.

4.2 . Characterization of nonlinear measurements and effects

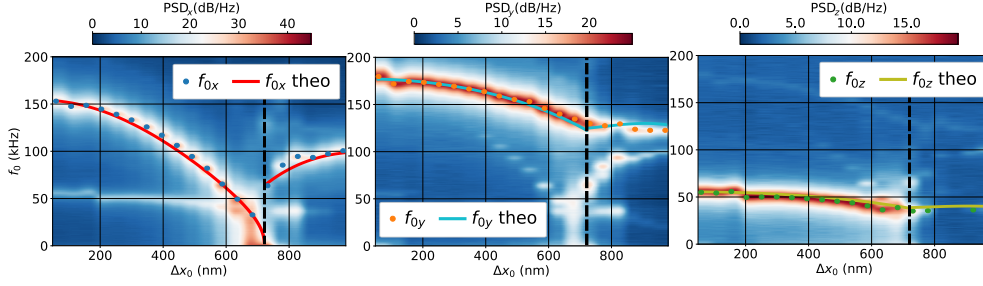


Figure 4.6: Observation of the evolution of f_{0x} , f_{0y} and f_{0z} while separating two beams from a distance Δx_0 , from 50 to 1000 nm. The evolution of the three frequencies are in good agreement with the theoretical predictions, with a noticeable bifurcation along the x-axis when the potential goes from a single to double-well configuration, around $\Delta x_0 = 700$ nm. We also observe cross-talk between axes.

on Gaussian distributions

4.2.1 . Study of displaced harmonic traps

As discussed in chapter 2, our detection scheme is nonlinear, and the measured signal is not directly proportional to the particle position. The previous section showed that this affect the determination of distributions created by dual beams as soon as they extend over a large spatial range. To better circumscribe the problem, we study how nonlinear measurements affect Gaussian distributions. To do so, we use a single trapping laser beam that we displaced from the centre by a distance x_0 . Thus, the trap is at first order harmonic, and the associated particle distribution density is a displaced Gaussian distribution. As in the previous section, we compute the particle distribution density, for different trap position x_0 . However, here the particle displacement is not calibrated and all the data are shown in detection signal unit (here mV). Similarly, we can compute an *effective potential*, corresponding to the log of the histogram of the measured signal, and that is just a convenient representation of the data. The resulting particle distribution densities and effective potentials are shown in figure 4.7. Further statistical studies on the recorded signals can then be done by computing their standard deviations, skewnesses and kurtoses, as shown in figure 4.8. Theses figures 4.7 and 4.8 clearly presents the limitations of the detection : while around the centre, the potentials are harmonic, as should be expected, they become skewed and their apparent stiffness increases when moving outside (equivalently, the standard deviation of the corresponding distributions decreases, hence their more peaked appearances). From now on, it should be clear that this is a strong limitation to the intended use of our system for the study of out-of-equilibrium thermodynamics in anharmonic potentials. Indeed, the fact that we cannot measure the true dynamics of the particle will affect the computation of the distributions and its moments, as well as thermodynamics quantities such as heat and work.

4.2.2 . Existing approaches

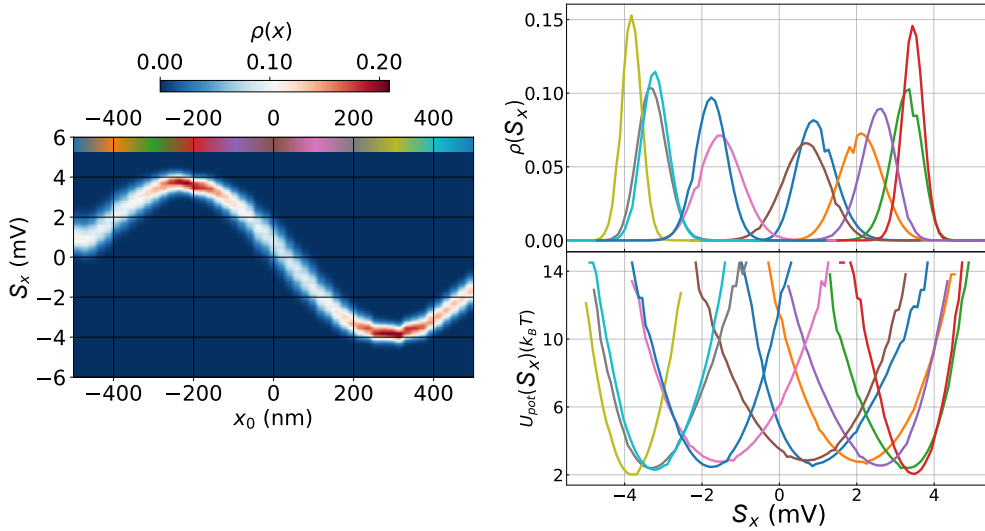


Figure 4.7: Evolution of the measured distributions and potentials while displacing the trap along the x-axis. The coloured top bar of the left figure indicates the position of the distributions plotted on the right. The nonlinear and non-bijective nature of the measurement is evident, and causes the observed issues for the estimation of the real potentials/distributions. After turning points located at ± 250 nm, which corresponds to minima of sensitivity, the mean values of the measurements move back to the centre. Thus, we find ourselves dealing with ambiguity, since multiple positions can lead to the same measured signal.

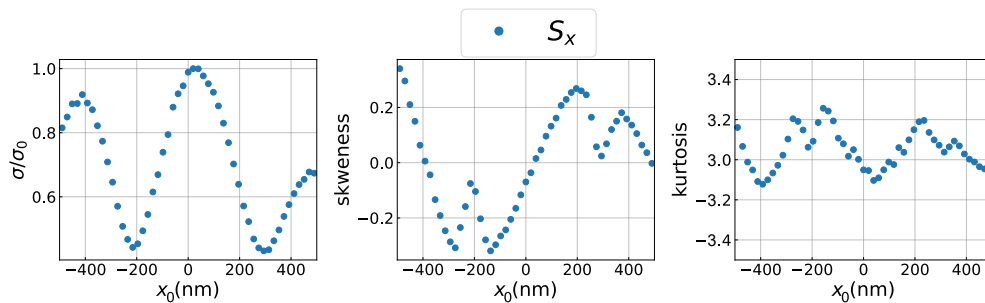


Figure 4.8: A look at the statistical quantities of the distributions presented in figure 4.7. Standard deviations / skewnesses are strongly affected as soon as the trap is moved away from the centre

From the previous subsection and the last of chapter 2, we have characterized the limits of our measurement procedure. Now that we are aware of its complexity, what can we do to recover the real 3D dynamics of a particle over a micrometer range?

From the existing literature, a few tracks could be followed :

- We could try to extend the linear range of our measurement, as suggested in [163]. There is however a trade-off between the extension of the linear range, which is a diminution of the SNR.
- We could resort to beam shaping techniques of the measuring beam itself, by using cylindrical lenses or an AOM/SLM to use other modes, such as TEM_{10} as in [164], to the price of added experimental complexity.
- We could use a fast camera such as a Phantom TMX Serie, or event base imaging such as the Prophesee camera presented in [165]. However, the particles used here are far bigger ($5 \mu\text{m}$) than ours.
- An interesting new approach presented in [166] proposes to use polarization measurements to extend the linear range of detection of QPD. Again, this work is performed with μm spheres.
- Finally, we could use the aforementioned cross-coupling, as in [167], to obtain a calibration curve (pictured in figure 4.9) used to compute a Maximum Likelihood Estimator (MLE) of the particle position for given signal coordinates (S_x, S_y, S_z) . Unfortunately, the signal standard deviation of our system is far bigger than the one of the system considered in [167], which makes the use of an MLE estimator difficult.

A last observation could be done in figure 4.9: a variation of the ellipsoid's obliquity is noticeable when moving the trap position. Is this a real physical effect, meaning that the beam diffracted by the AOM rotates depending on its position, or is it again just a measurement problem? Thankfully, we can discard the first alternative, by verifying that the transformations of simulated Gaussian data by the functions derived in chapter 2 (section 2.4.3) follow the same pattern. This is a real-life example of the effects mentioned in [115], which explains more generally the "peanut" shape of (S_x, S_y) or (S_x, S_z) plots.

Independently of the adopted method, a further constraint is that the measurement laser beam must remain as low as possible (typically 1 mW), to avoid that it contributes to the existing optical forces, and thus biases the particle dynamics characterisation.

From these elements, we conclude that to determine the real 3D position of a trapped particle in an extended range, one should at the same time fuse usable information along the 3 axes, as well as take into account the whole trajectory. This is the matter of the next section.

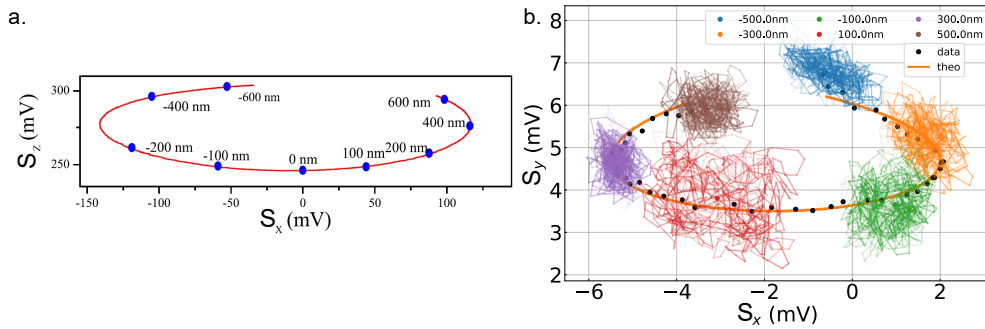


Figure 4.9: a. Comparison of (S_x, S_y) plots, taken in the overdamped regime (a.) [167] and in the underdamped regime (b.). While a simple MLE estimator was efficient in the overdamped regime, due to the standard deviation of the signal being 3 order of magnitude smaller than the range of measurement, such approach is not an option in the underdamped regime, where the particle explores a lot more signal space, as can be observed by plotting times traces at a few points. To deal with the inherent ambiguity of our measurements, an alternative solution is needed.

4.3 . Non-linear Kalman filter

Our objective is to determine the real particle trajectory from the measurement of its dynamics, which is biased by the nonlinearities of the measurement scheme. Kalman filtering is particularly adapted to address this question.

From its early use in the field of rocket science [168, 169] to modern use in climate science [170, 171], its purpose is to predict and eventually control the trajectory of a stochastic system, based on noisy observation data and a Bayesian transition model. While in optomechanics the Kalman filter has mainly been used to perform real-time Gaussian states estimations [172, 173, 65], it has to the best of our knowledge never been applied to fuse the 6D information (positions+velocities) available in underdamped experiments to access to the real dynamics of the particle in large potentials. This system nevertheless presents similarities with systems studied in robotics [174, 96, 175], and we can adapt previous examples to our experimental setup [176].

Ultimately, this work could be further developed by taking inspiration from the molecular dynamics community, where learning of complex potentials parameters is accelerated thanks to new neural networks libraries such as JaxMD [177, 178].

4.3.1 . Principle and state of the art

We start with a brief introduction to the linear Kalman filter, and then present its adapted version to nonlinear dynamics ¹. While multiple variants of this have been proposed, like the Extended Kalman filter or the Ensemble Kalman filter, we chose the Unscented Kalman filter due to its computational simplicity (which does not involve Monte Carlo methods), and the existence of readily adaptable

¹For details, the interested reader can refer to [179].

codes [176].

The dynamics of a linear stochastic system, described by its state vector x , without external inputs is given by:

$$x_{k+1} = Ax_k + v_k, \quad (4.15)$$

where k represents the time step, A is the matrix encoding the (linear) dynamics, and v_k is the system noise.

If one measures its dynamics, then the observation vector y is related to x by:

$$y_k = Cx_k + \xi_k, \quad (4.16)$$

with C the (linear) output coupling matrix, and ξ_k the output (measurement) noise.

The objective of the Kalman filter is then to predict the future state of the system, knowing its past dynamics. In this context, the predicted state and update estimate are written:

$$\begin{aligned} \hat{x}_{k+1}^- &= A\hat{x}_k && \text{(propagation)} \\ \hat{y}_{k+1} &= C\hat{x}_{k+1}^- \\ \hat{x}_{k+1} &= \hat{x}_{k+1}^- + L(y_{k+1} - \hat{y}_{k+1}) && \text{(update)} \end{aligned}$$

where L is the observer gain matrix.

These equations give the definitions of the *prediction*, \hat{x}_{k+1}^- , as the estimate of x_{k+1} obtained solely from the knowledge of the dynamics A and the prior estimate \hat{x}_k , and *before* the observation y_{k+1} . Equation (propagation) is thus called the *propagation* step. Then, the estimation of \hat{y}_{k+1} is computed from \hat{x}_{k+1}^- . Finally, the *estimate* \hat{x}_{k+1} is computed just *after* the observation y_{k+1} , and the discrepancy between the real and predicted observation \hat{y}_{k+1} is thus taken into account through the observer gain L . Equation (update) is then called the *update* step.

A similar set of equations can be derived for the estimation of the covariances matrices $P_k = \langle (x_k - \hat{x}_k)(x_k - \hat{x}_k)^T \rangle$, $P_k^- = \langle (x_k - \hat{x}_k^-)(x_k - \hat{x}_k^-)^T \rangle$.

The goal is then to find a strategy which will minimize this covariances, since this is equivalent to minimizing the error between the estimates and the real states.

Without delving into too much details, Kalman proved that for each step, the optimal observer gain matrix L^* is given by :

$$L_{k+1}^* = P_{k+1}^{xy} \left(P_{k+1}^y \right)^{-1} \quad (4.17)$$

where $P_{k+1}^{xy} = P_{k+1}^- C^T$ is the state-observation covariance matrix, and $P_{k+1}^y = CP_{k+1}^- C^T + Q_\xi$ is the observation covariance.

The update scheme thus derived is stable as long as the covariance matrix for state estimation errors P_k stays close to reality, i.e. does not vanish when the

actual error does not. While this is proven to be the case as long as the system follows linear dynamics, it is not when things become nonlinear.

In the case of nonlinear systems, the propagation and update equations are then turned into :

$$\hat{x}_{k+1}^- = f(\hat{x}_k) \quad (\text{propagation})$$

$$\hat{y}_{k+1} = h(\hat{x}_{k+1}^-)$$

$$\hat{x}_{k+1} = \hat{x}_{k+1}^- + L(y_{k+1} - \hat{y}_{k+1}) \quad (\text{update})$$

where f and h are now nonlinear functions. In our case, f would be a Langevin function with a given local stiffness and h would be the measurement vector (S_x, S_y, S_z) .

A first approach, called the Extended Kalman Filter, is then to fall back to linear equations for the evolution of the co-variances matrices, by taking the partial derivatives of f and h . While this performs well enough to guide a rocket to the moon or even for the Global Positioning System, this is not the case for strongly nonlinear systems such as ours.

The Unscented Kalman Filter (UKF) [174] provides a nice alternative, by making use of the Unscented Transform (UT). The main idea is summarized by the authors as :

it is easier to approximate a probability distribution than it is to approximate an arbitrary nonlinear function or transformation [175].

Thus, the problem is turned into the choice of a set of points forming an interpolation basis which captures the characteristics of the distribution $\rho(x)$ (i.e. its moments up to a given order). The transformed interpolation basis is then used to compute the mean and covariance matrices of the observation. We again refer the interested reader to the relevant literature, and resume the principle of the UKF in figure 4.10

For a symmetric distribution in a space of dimension n , [181] demonstrates that it is sufficient to have an interpolation basis of $2n$ points. Crucially, the interpolation basis can be efficiently computed at each steps of the UKF as the lines of a Cholesky decomposition of the covariance matrix P_k .

These advantages of the UKF filter encouraged us to use the implementation accessible in [176] on our system, to see if it could help to determine the real dynamics of the particle. Since we are able to determine the nonlinear observation function $h \equiv (S_x, S_y, S_z)$ from the aforementioned calibration procedure (see section 2.3), and we can do reasonable hypotheses regarding the propagation function f (which is a Langevin equation), we should be able to use the UKF to compute the original distribution $\rho(x)$ from our measurements, and hence access to the true shape of arbitrary potentials.

4.3.2 . Validation of UKF on simulated data

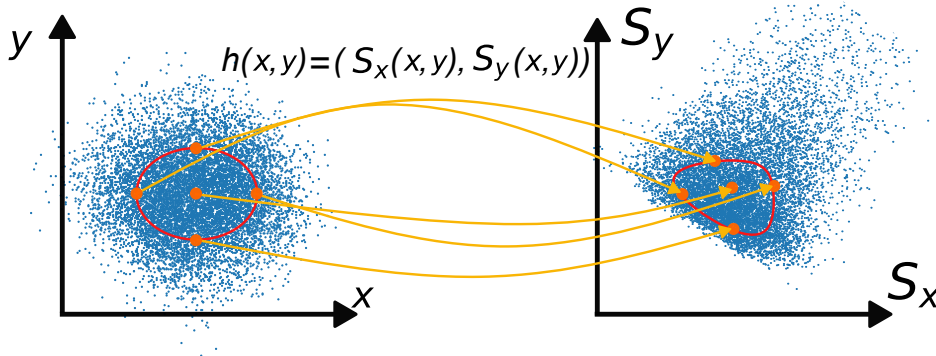


Figure 4.10: Principle of the Unscented Transform. The actual position of the particle in the (x, y) space is distributed as a Gaussian (blue points on the left). The application of the nonlinear observation function $h(x, y) = (S_x(x, y), S_y(x, y))$ provides the measured distribution (blue points on the right). A set of special points (orange) are chosen in (x, y) space so that they have the same mean and covariance than the real distribution of blue data points. The nonlinear observation function h is then applied, resulting in a set of transformed points that encodes the mean and variance of the data points in (S_x, S_y) space. By using this simple deterministic procedure, the UKF is computationally lighter than other approaches such as Monte Carlo techniques. Figure inspired from [180]. The h function corresponds to the actual measurement response of our experimental setup (S_x, S_y, S_z) .

To confirm the ability of the UKF to track the real dynamics of the particle, we start by testing it on simulated data. We model the experiment presented in section 4.2.1, in which a particle is trapped in a harmonic potential whose centre x_0 is displaced over $1 \mu\text{m}$.

From the Euler-Maruyama scheme, we generate time traces corresponding to the experimental conditions of the previous section, by computing a transition function f which is the Langevin equation of the system, with given stiffness k_{trap} and trap centre position x_0 . These "ground truth" traces are then passed through the measure function $h \equiv (S_x, S_y, S_z)$ to obtain traces emulating the real ones we would obtain through an experimental measurement.

Then, we apply the UKF algorithm to these *in silico* measurements to fall back to the real space dynamics. The results are then compared to the initial traces, to appreciate the UKF efficiency. Results of these simulations are presented in figure 4.11.

From these experiments, we demonstrate the efficiency of UKF to address our experiment issues in a model case. Also, it allows us to provide some important observations:

- Under the studied model conditions (total knowledge of the measurement function h and transition function f , the UKF is able to reconstruct with high fidelity the initial traces, except for a few positions.

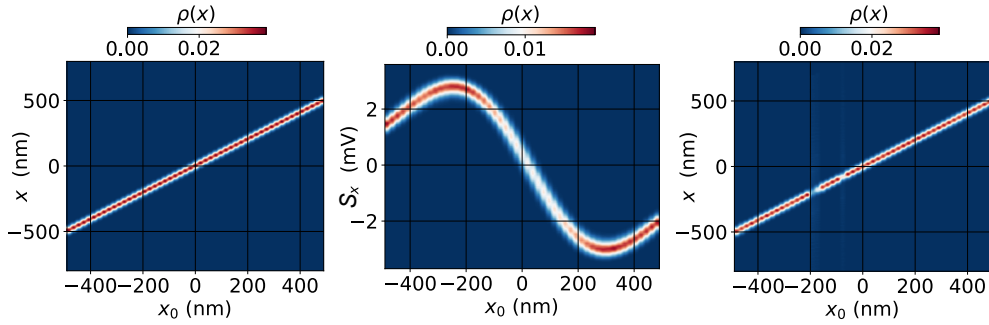


Figure 4.11: Applying the UKF to simulated data. Left panel : We simulate Gaussian distributions (each blur on the line) corresponding to a trap displaced along a $1 \mu\text{m}$ range, as in the experiments. Center : we apply the observation function $h \equiv (S_x(x, y, z), S_y(x, y, z), S_z(x, y, z))$ to the Gaussian distributions. The resulting shape well corresponds to experimental observation (Figure 4.7). Right : we feed the simulated measurements into the UKF. Here, we perfectly know f and g , and did not add measurement noise. We are then able in one run to recover almost all distributions, the missing ones being probably recoverable.

- An important parameter is the sampling rate. While the UKF performs well even in the strongly non-linear case when the sampling rate is above 10 times higher than the largest oscillation frequency of the particle, it deteriorates significantly when the sampling rate is lowered : divergent trajectories are then observed. While this is not a problem for simulated traces, it implies to analyze a huge amount of data, which will moreover increase if we use this to observe rare events.
- The computation, for each step, of the transform of each sigma points by h is computationally time-consuming. For allowing an efficient use of the UKF, it is necessary to optimize and parallelize as much as reasonably possible the code.

To quantify more precisely how much the initial distributions are reconstructed, we present on figure 4.12 the dependency in position of the standard deviation, the skewness, and the kurtosis, of the simulated traces of the particle dynamics, their associated measurements, and the UKF filtering of these measurements. Interestingly, the UKF allows us to recover the true mean, standard deviation and skewness (except for the failed traces) of the particle dynamics. Concerning, the kurtosis, our implementation of the UKF does not provide an important improvement over the measured data. Generalizations of the UKF developed to tackle this aspect could be implemented in our code to correct this [182].

4.3.3 . Experimental demonstration of UKF

To validate the efficiency of the UKF on real datasets, we then apply it to experimental time traces. We first focus on the case of a displaced harmonic beam, which has been experimentally studied in figure 4.7, and simulated in the

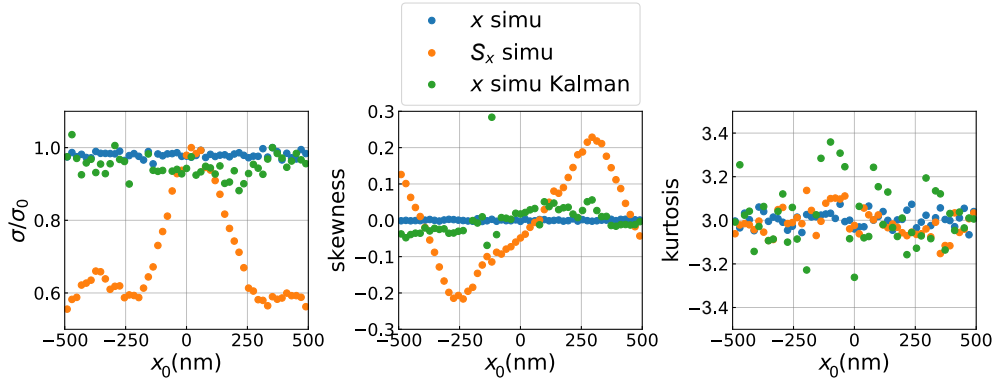


Figure 4.12: Second, third, and fourth statistical coefficient of traces simulated for traps centred at x_0 , their measurements, and the Kalman filtering of these measurements.

previous section. Given the time required to process the data with the UKF, we focus on two specific cases:

1. the harmonic trap is centred on the measurement beam, such that the observation function is linear,
2. the harmonic trap is displaced by 250 nm from the measurement beam, so the measurement sensitivity is the lowest, and the observation function is strongly non-linear.

Thus, these datasets represent the best and worst cases of the results that can be recorded on our experimental setup. The corresponding measured time traces and the associated predicted trajectory by the UKF are shown in figure 4.13.

As can be expected, the data being a lot noisier than the simulations, some extra care is needed. It is particularly important to define correctly the system and measurement noise matrices of the filter, Q and R .

As a sanity check, since we cannot compare the results with the real position of the particle, we show in figure 4.13 a comparison between the signal time trace and the signal computed from the positions found with the UKF.

We first note that the UKF provides estimated trajectories with increased signal-to-noise and significantly reduces the measurement cross-coupling between the axes. The good agreement between the measured time traces $S_i(x, y, z)$ and the estimates $S_i(\hat{x}, \hat{y}, \hat{z})$ is a good hint of the efficiency of the UKF. Interestingly, the UKF is able to recover a change in frequency along z , which is effectively observed in the PSD (shift from 39 kHz to 33 kHz), while the propagation function f is not changed and was set for an oscillation frequency of the z -axis of 39 kHz. This ability to discover signals without needing a precise spectral definition is a quality of the UKF for the study of nonlinear systems. However, this must be balanced with the fact that in some noisy situations, it can also create non-existent frequencies, as observed for the \hat{x} trajectory in 4.13-d. One could also notice that in the

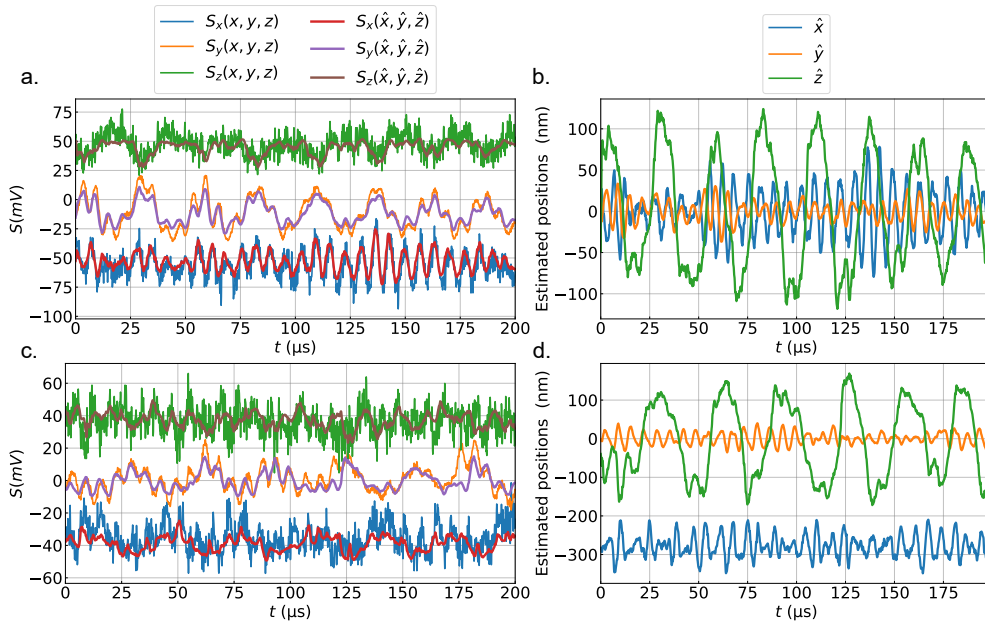


Figure 4.13: Comparison between original time traces $S_i(x, y, z)$, estimated positions \hat{x} , \hat{y} , \hat{z} computed with the UKF, and injected back into the observation function h to obtain signals of the estimates $S_i(\hat{x}, \hat{y}, \hat{z})$. This comparison is performed iteratively for each sigma points of the UKF, and guarantees that the underlying trajectories in real space stay consistent with the measurements. a and b : performed at the centre of the x-axis, with a strong cross-coupling between S_y and S_z , which is well decoupled by the UKF. c and d : performed at -250 nm from the centre of the measurement beam, where the sensitivity along x and z is minimal. While information along z is well recovered (even a change in f_{0z} , the result is less satisfying on x , with an oscillation that does not match existing frequencies).

case of z , the oscillations are non-smooth, which results from the linearization of h presented in equation (2.75).

Finally, despite these spurious effects in the case of worst measurement sensitivity, which calls for improvement in our UKF implementation, these results demonstrate the power of Kalman filtering to retrieve the true particle dynamics. These encouraging results thus call for a test of the UKF on broad optical potentials, which constitutes the goal of the presented work.

4.3.4 . Observation of the particle dynamics in a strongly nonlinear potential

Having tested the UKF on a displaced harmonic trap, we now go back to the initial intention of this work, which was to characterize nonlinear potentials.

In that context, we address the dynamics of a particle trapped in a bistable optical potential generated by two beams separated by $\Delta x_0 = 800$ nm at the focus of the objective. The particle dynamics is recorded on the three detectors for 1 s at a sampling rate of 10 MS/s providing the three measured signals $\{S_x, S_y, S_z\}$. Figure 4.14 represents the 2D histogram of the signals S_x, S_y . The shape of this histogram is completely dominated by the measurement non-linearities, and does not reproduce faithfully the particle probability density.

To provide a better estimate of the actual particle probability density, we thus apply the UKF to the recorded time traces.

The histogram resulting from this filtering is presented in figure 4.15. It shows a clear separation between the two wells, which are of almost equal depth, contrary to the unfiltered raw measurement (figure 4.14) or to the examples shown at the beginning of this chapter (figure 4.5-c.).

First, we note that the UKF retrieve a distance between the two traps of 500 nm, which match the one expected for the sum of two trapping beams shifted by $\Delta x_0 = 800$ nm (green curve in figure 4.15). This is particularly interesting given that the centres of the wells are located right at the minimum of sensitivity of the x -measurement as shown by the figure 4.2.1.

Going more into the details of the reconstructed potential, we notice that its shape along x is still slightly asymmetric, and is not like the inverted harmonic potential one would expect from a simple dual beam configuration. While it could possibly be an artefact of the UKF reconstruction (performed only on a tenth of the whole dataset, which could mean that we undersample rare configuration at higher $k_B T$), we would like to explore another hypothesis.

The potential along x , completed by symmetry for the missing part, can be fitted by an order 4 polynomial. To explain the "flat top" geometry of it, we suppose that in the middle of the double well potential, the dynamic of the particle is actually affected by the measurement laser, which acts as a third (faintly) trapping beam. By doing another fit with the potential energy of the IR beams $U_{0,\text{trap}}$ and of the measurement beam $U_{0,\text{meas}}$ as free parameters, we find $U_{0,\text{trap}}/U_{0,\text{meas}} \approx 120$, which is in line with experimental conditions ($P_{\text{meas}} \approx 1$ mW at $\lambda_{\text{meas}} = 785$ nm,

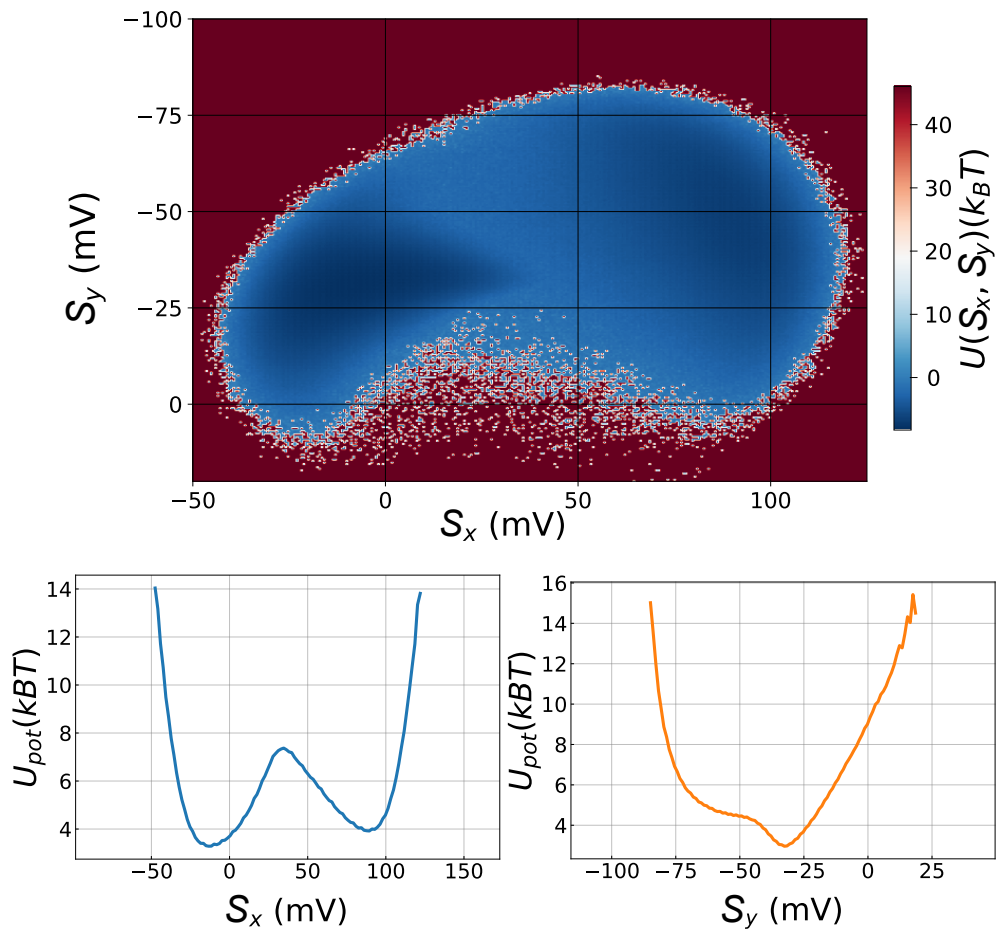


Figure 4.14: 2D histogram of (S_x, S_y) data acquired in a double-well potential, with beam separated by 800 nm. The nonlinear measurement distorts the potential along all axes, making it impossible to recover trustworthy information about its real shape, in particular its local stiffness.

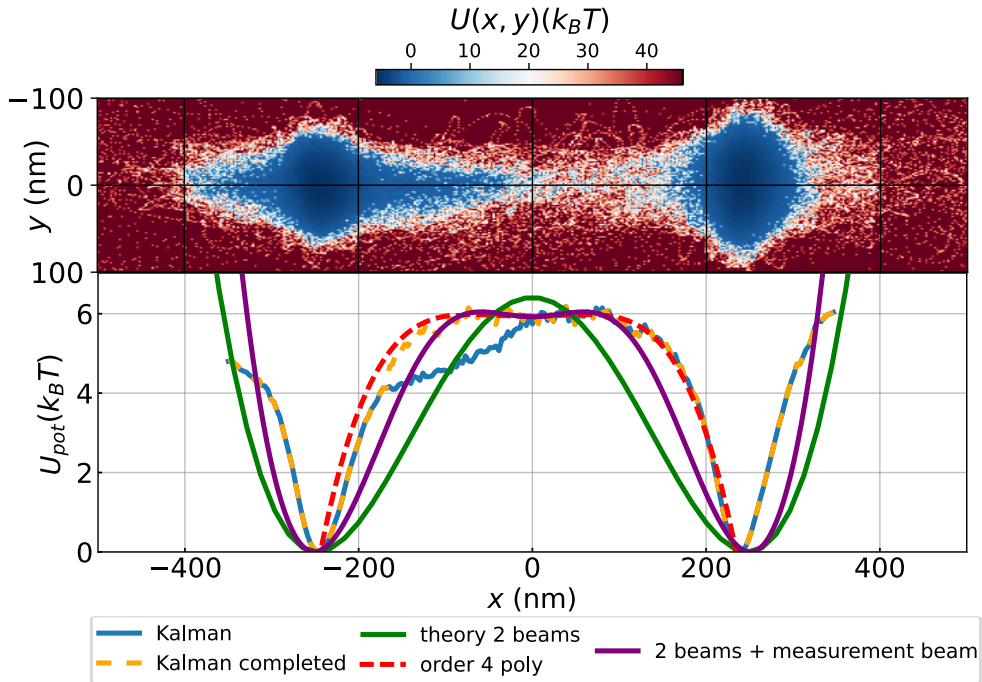


Figure 4.15: (Top) 2D histogram resulting from the processing of the data pictured in figure 4.14 thanks to the UKF. Starting from a propagation function f with arbitrary spaced centres, the filter shows that the true wells are located at ± 250 nm around the origin, which is expected from theory. What is not is the almost flat (and skewed) top at the centre, visible on the histogram along x (bottom). We hypothesize that this is not an artefact of our filter, but a real indication that the measurement beam is weakly perturbing the behaviour of the particle, requiring further investigation. To confirm that, we plot a symmetrization (yellow dotted line) of the result of the UKF (blue line). We see that this does not match the expected profile with two beams (green), but more a fourth order polynomial (dotted red). Considering that the flat centre is due to the gradient force of the measurement beam, we fit the symmetrized curve with a model with free parameters the potential energies of each individual traps. The results of this procedure are coherent with the measured power values. Another notable discrepancy between the Kalman filtered result and all other models lies in the width of each well, which could be due to an error in the definition of the stiffness in f .

vs $P_{\text{las}} \approx 250$ mW at $\lambda_{\text{trap}} = 1064$ nm). The asymmetry could also be attributed to the misalignment of the measurement beam, which slightly deforms the left part of the double well through the scattering force \mathbf{F}_{scat} , thus pushing the particle preferentially to the left well. This hypothesis should be confirmed by further tests, but is to take into account if we want to finely control nonlinear traps.

4.3.5 . Conclusion

In this chapter, we demonstrated our ability to generate arbitrary tailored potential. The difficult part is to define a strategy to characterize them unambiguously, the interferometric measurement being linear only in a range of ≈ 200 nm. To this end, we presented a solution based on a version of the Kalman filter adapted to nonlinear problems. While computationally heavy-handed, this approach extends the linear range more than a $1 \mu\text{m}$, which is sufficient to start working with large potentials. A first example of a reconstructed double-well potential highlights the capacity of our setup to explore with a high level of detail complex nonlinear dynamics, as well as their exquisite sensitivity to small perturbations.

5 - General Conclusion

*Σὰ βγεῖς σὸν πηγαῖμὸ γιὰ τὴν Ἰθάκη,
νὰ εὐχέσαι νᾶναι μακρὺς ὁ δρόμος,
γεμάτος περιπέτειες, γεμάτος γνώσεις.*

— Constantin Cavafis, *ΙΘΑΚΗ* (1911)

At the close of this dissertation, I recapitulate the main results of my thesis and discuss possible future directions and open questions.

The initial motivation of my work was to study the dynamics of stochastic systems and more specifically their out-of-equilibrium behaviour. As presented in chapter 1, this subject is of historical significance, appearing in many research endeavours of the 20th century, amongst which condensed matter [183], biology [184] or cosmology [185].

A major challenge in most of these fascinating topics is to gain fine control of the characteristic parameters of the system under consideration, with the intent of performing or probing state-to-state transformations.

In the scope of this thesis, I thus considered a simple but iconic system, presented in chapter 2: a dielectric nanoparticle levitated in an original optical tweezers experiment.

Indeed, our setup advantages are two-fold :

- An easy control of the coupling of the nanoparticle to the environment by simply tuning its damping, a quantity that depends linearly of the pressure of gas.
- By controlling in time and space the trapping potential through an acousto-optic modulator, we can thus define the thermal state of the particle through its distribution.

In chapter 3, I first explored the thermodynamics at the nanoscale, by studying relaxations between thermal equilibrium states in the strong (overdamped) or weak (underdamped) coupling regimes. Experiments were performed by changing abruptly the stiffness of harmonic potentials. The study highlighted the existence of two different relaxation timescales :

- In the overdamped regime, the limiting factor is the relaxation in position of the particle, corresponding to the time necessary to explore a new phase space.
- Conversely, in the underdamped regime relaxation happens through the coherent exchange of potential and kinetic energy, thus being limited by the velocity relaxation.

To beat these limits and reach equilibrium faster, I then implemented shortcuts to equilibrium protocols designed in the theoretical article [125], and proved for the first time that they work in the underdamped regime. This opens the possibility to improve the efficiency of nano-heat engines, by enabling fast compression / expansion cycles.

The extension of this study beyond simple thermal states defined by Gaussian distributions called for the generation of more complex, nonlinear potentials, a work presented in chapter 4. After developing a procedure to generate arbitrarily shaped potentials, I presented a first realization of tunable nonlinearities, by using dual beams of variable spacing. The control of nonlinearities was proved by a confirmation that the measured power spectral densities of these potentials were in good agreement with a simple theoretical model.

To perform thermodynamic studies in such potential, one challenge is then to determine unambiguously the dynamics of the particle in real space, since our measurements are nonlinear and non-bijective themselves. I thus developed a new approach based on the Unscented Kalman Filter to recover the true positions, which lead to promising results, in particular for imaging a large double-well potential.

With respect to the perspectives and future directions of study that this work opens, we mention the following :

- The ability to realize dynamical variations of nonlinear potentials offers a way to study dissipative dynamics from arbitrary initial and final distributions [186]¹. In the same line of thinking, the development of protocols optimal in time and generated power remains an active domain of research [187, 188], that would certainly benefit from further experimental proof of concepts.
- As noted in [189], nonlinearities can be used to enhance the sensitivity of a macroscopic resonator to perform measurements. Our platform thus provides an ideal test-bed to explore weak forces sensing. In particular, it is well-adapted to tackle stochastic resonance [190], which is a potent way to enhance weak signals detection [191]. With controllable double-well potentials or triple-wells potentials [192], we could further explore the effects of tuning the wells depths and widths [193], or their asymmetries [194].
- Reflecting on other subjects raised in chapter 1, these experiments could represent a stepping stone to study the thermodynamics of computation, by implementing more complex operations than the erasure of a bit performed

¹Note that in this work, the Kullback-Leibler divergence is used to compare the amount of dissipation during a given nonequilibrium process for arbitrary distributions, reminiscent of the approach developed to test the robustness of ESE protocols.

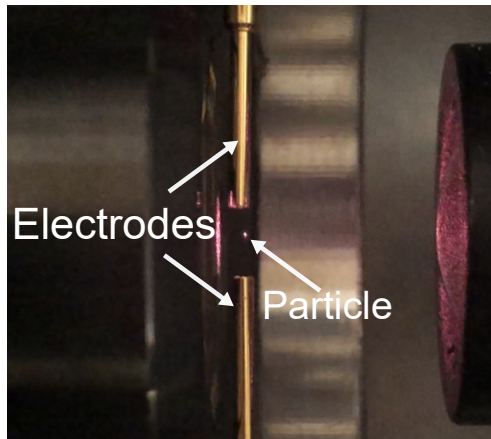


Figure 5.1: Picture showing two gold electrodes, used to generate a controllable electric field. By interacting with the charges generated on the surface of the particle through a plasma discharge, this adds another degree of freedom to perform thermodynamics studies.

in Landauer's bound like XOR [195]. Studying the energetic cost of computation appears as a timely question, and could probably also take advantage of the work performed on shortcuts to equilibrium.

- By adding electrodes (pictured on figure 5.1) as presented in [196], it is possible to use the charges at the surface of a particle to act on it via Coulomb force. Through this, we could add feedback to cool the particle [63], or conversely, add some noise to emulate an effective temperature. This adds a new degree of freedom for the realization of shortcuts to equilibrium protocols, as presented in [197], and allows to consider non-isothermal transformations, necessary to experiment on nano-heat engines. Furthermore, it allows to generate Levy flights, for which shortcuts to equilibrium have also recently been theoretically derived [198].
- On a more exploratory note, a timely subject is the study of martingales, proposed in [199, 200] as an encompassing framework for stopping times problems.
- Finally, mastering such nonlinear potentials for thermal states is a first step towards their use for more challenging applications, such as controlling quantum states through shortcut protocols [201].

On a last note, the excellent control of the systems I demonstrated can be an essential asset to probe subtle nanophysics phenomena. The presence of scattering and curl forces, which are non-conservative, and that we have neglected in most of this thesis, may generate non-trivial particle dynamics, with the emergence of loops in the particle dynamics [202, 84]. These effects may significantly affect

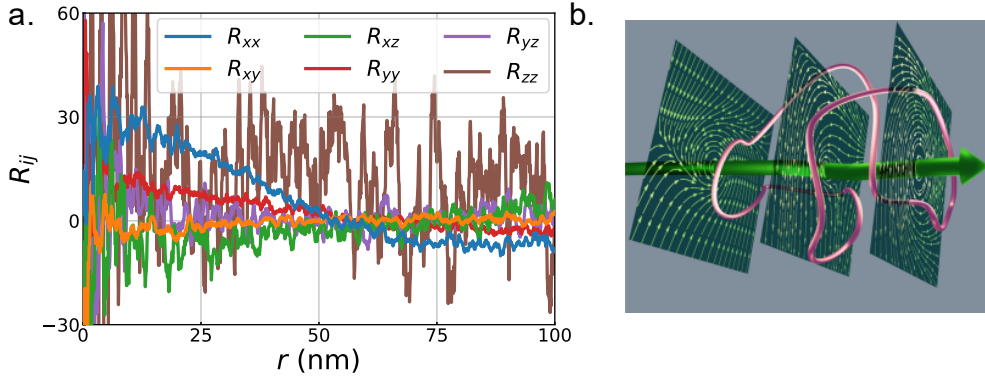


Figure 5.2: a. Two points velocity correlations $R_{ij}(r) = \langle v_i(r_0)v_j(r_0 + r) \rangle$ computed at $t = 5 \mu\text{s}$ after the start of a compression STEP protocol. The presence of correlations is surprising, but suggestive of collective motion such as vortices. b. A Brownian particle undergoing diffusion in the presence of a non-conservative force-field, adapted from [203]. The authors consider the winding number of the trajectories to derive a topological fluctuation theorem.

particle stochastic dynamics and the related energetics quantities, such as heat. Their study may allow the test of adapted fluctuation theorems [203].

As a very preliminary work toward the observation of such effects, we propose to compute the two-points velocity correlations $R_{ij}(r) = \langle v_i(r_0)v_j(r_0 + r) \rangle$ between the 2×10^4 time traces of the STEP protocol presented in chapter 3. The result of such computation, estimated at a time $t = 5 \mu\text{s}$ after a compression STEP, is shown in figure 5.2 a. It indicates that the velocities of individual realizations of trajectories are correlated, at least for this time step, in particular for the R_{xx} component (we note that at the same time step after an expansion STEP, R_{yy} and R_{zz} dominate). In fluid dynamics, these correlations usually indicate the presence of loops or vortices, and are also studied in the context of magneto-optical traps [204]. Despite the preliminary nature of these results, which would require studying the evolution of these correlations in time, it demonstrates the power of our experimental setup to analyze fine effects for a wide variety of nanophysics situations.

Bibliography

- [1] A. Einstein. Über die von der molekularkinetischen theorie der wärme geforderte bewegung von in ruhenden flüssigkeiten suspendierten teilchen. *Annalen der Physik*, 322(8):549–560, 1905.
- [2] M. von Smoluchowski. Zur kinetischen theorie der brownschen molekularbewegung und der suspensionen. *Annalen der Physik*, 326(14):756–780, 1906.
- [3] Jean Perrin. Mouvement brownien et grandeurs moléculaires. *Radium (Paris)*, 6(12):353–360, 1909.
- [4] Benoit B. Mandelbrot and John W. Van Ness. Fractional brownian motions, fractional noises and applications. *SIAM Review*, 10(4):422–437, 1968.
- [5] Devlin M. Gualtieri. File:Brownian ratchet.svg - Wikimedia Commons — commons.wikimedia.org. https://commons.wikimedia.org/wiki/File:Brownian_ratchet.svg, 2018. [Accessed 24-Jul-2023].
- [6] Jeongmin Hong, Brian Lambson, Scott Dhuey, and Jeffrey Bokor. Experimental test of landauer’s principle in single-bit operations on nanomagnetic memory bits. *Science Advances*, 2(3):e1501492, 2016.
- [7] H. Nyquist. Thermal agitation of electric charge in conductors. *Phys. Rev.*, 32:110–113, Jul 1928.
- [8] G.S Agarwal. Fluctuation-dissipation theorems for systems in non-thermal equilibrium and application to laser light. *Physics Letters A*, 38(2):93–95, 1972.
- [9] Lars Onsager. Reciprocal relations in irreversible processes. i. *Phys. Rev.*, 37:405–426, Feb 1931.
- [10] Herbert B. Callen and Theodore A. Welton. Irreversibility and generalized noise. *Phys. Rev.*, 83:34–40, Jul 1951.
- [11] Ryogo Kubo. Statistical-mechanical theory of irreversible processes. i. general theory and simple applications to magnetic and conduction problems. *Journal of the Physical Society of Japan*, 12(6):570–586, 1957.
- [12] R Kubo. The fluctuation-dissipation theorem. *Reports on Progress in Physics*, 29(1):255, Jan 1966.
- [13] N. Pottier. *Nonequilibrium Statistical Physics: Linear Irreversible Processes*. Oxford Graduate Texts. OUP Oxford, 2010.

- [14] Dana Z. Anderson, Josef C. Frisch, and Carl S. Masser. Mirror reflectometer based on optical cavity decay time. *Appl. Opt.*, 23(8):1238–1245, Apr 1984.
- [15] G. Rempe, R. J. Thompson, H. J. Kimble, and R. Lalezari. Measurement of ultralow losses in an optical interferometer. *Opt. Lett.*, 17(5):363–365, Mar 1992.
- [16] Denis J. Evans, E. G. D. Cohen, and G. P. Morriss. Probability of second law violations in shearing steady states. *Phys. Rev. Lett.*, 71:2401–2404, Oct 1993.
- [17] C. Jarzynski. Nonequilibrium equality for free energy differences. *Phys. Rev. Lett.*, 78:2690–2693, Apr 1997.
- [18] C. Jarzynski. Equilibrium free-energy differences from nonequilibrium measurements: A master-equation approach. *Phys. Rev. E*, 56:5018–5035, Nov 1997.
- [19] Gavin E. Crooks. Entropy production fluctuation theorem and the nonequilibrium work relation for free energy differences. *Phys. Rev. E*, 60:2721–2726, Sep 1999.
- [20] K. Sekimoto. *Stochastic Energetics*. Lecture Notes in Physics. Springer Berlin Heidelberg, 2010.
- [21] Udo Seifert. Entropy production along a stochastic trajectory and an integral fluctuation theorem. *Phys. Rev. Lett.*, 95:040602, Jul 2005.
- [22] David H Wolpert. The stochastic thermodynamics of computation. *Journal of Physics A: Mathematical and Theoretical*, 52(19):193001, Apr 2019.
- [23] J. Kepler. *De cometis libelli tres ...* De cometis libelli tres. Typis Andreae Apergeri, sumptibus Sebastiani Mylii bibliopolæ Augustani, 1619.
- [24] Thony Christie. The emergence of modern astronomy – a complex mosaic: Part XXV — thonyc.wordpress.com. <https://thonyc.wordpress.com/2019/12/11/the-emergence-of-modern-astronomy-a-complex-mosaic-part-xxv/>. [Accessed 26-Jun-2023].
- [25] James Clerk Maxwell. *A treatise on electricity and magnetism*, volume 1. Oxford: Clarendon Press, 1873.
- [26] T. H. Maiman. Stimulated optical radiation in ruby. *Nature*, 187(4736):493–494, Aug 1960.

- [27] A. Ashkin, J. M. Dziedzic, J. E. Bjorkholm, and Steven Chu. Observation of a single-beam gradient force optical trap for dielectric particles. *Opt. Lett.*, 11(5):288–290, May 1986.
- [28] A. Ashkin. Acceleration and trapping of particles by radiation pressure. *Phys. Rev. Lett.*, 24:156–159, Jan 1970.
- [29] H. Raab E. Kolmhofer. Fichier:Comet Hale-Bopp 1995O1.jpg — Wikipédia — fr.wikipedia.org. https://fr.wikipedia.org/wiki/Fichier:Comet_Hale-Bopp_1995O1.jpg, 1997. [Accessed 24-Jul-2023].
- [30] Uroš Delić, Manuel Reisenbauer, Kahan Dare, David Grass, Vladan Vuletić, Nikolai Kiesel, and Markus Aspelmeyer. Cooling of a levitated nanoparticle to the motional quantum ground state. *Science*, 367(6480):892–895, 2020.
- [31] Steven Chu, J. E. Bjorkholm, A. Ashkin, and A. Cable. Experimental observation of optically trapped atoms. *Phys. Rev. Lett.*, 57:314–317, Jul 1986.
- [32] E. L. Raab, M. Prentiss, Alex Cable, Steven Chu, and D. E. Pritchard. Trapping of neutral sodium atoms with radiation pressure. *Phys. Rev. Lett.*, 59:2631–2634, Dec 1987.
- [33] M. H. Anderson, J. R. Ensher, M. R. Matthews, C. E. Wieman, and E. A. Cornell. Observation of Bose-Einstein condensation in a dilute atomic vapor. *Science*, 269(5221):198–201, 1995.
- [34] Daniel Barredo, Sylvain de Léséleuc, Vincent Lienhard, Thierry Lahaye, and Antoine Browaeys. An atom-by-atom assembler of defect-free arbitrary two-dimensional atomic arrays. *Science*, 354(6315):1021–1023, 2016.
- [35] Manuel Endres, Hannes Bernien, Alexander Keesling, Harry Levine, Eric R. Anschuetz, Alexandre Krajenbrink, Crystal Senko, Vladan Vuletic, Markus Greiner, and Mikhail D. Lukin. Atom-by-atom assembly of defect-free one-dimensional cold atom arrays. *Science*, 354(6315):1024–1027, 2016.
- [36] Loïc Anderegg, Lawrence W. Cheuk, Yicheng Bao, Sean Burchesky, Wolfgang Ketterle, Kang-Kuen Ni, and John M. Doyle. An optical tweezer array of ultracold molecules. *Science*, 365(6458):1156–1158, 2019.
- [37] Miklós S. Z. Kellermayer, Steven B. Smith, Henk L. Granzier, and Carlos Bustamante. Folding-unfolding transitions in single titin molecules characterized with laser tweezers. *Science*, 276(5315):1112–1116, 1997.
- [38] L. B. Pires, D. S. Ether, B. Spreng, G. R. S. Araújo, R. S. Decca, R. S. Dutra, M. Borges, F. S. S. Rosa, G.-L. Ingold, M. J. B. Moura, S. Frases, B. Pontes, H. M. Nussenzveig, S. Reynaud, N. B. Viana, and P. A. Maia Neto. Probing the screening of the casimir interaction with optical tweezers. *Phys. Rev. Res.*, 3:033037, Jul 2021.

- [39] Kai-Niklas Schymik, Bruno Ximenez, Etienne Bloch, Davide Dreon, Adrien Signoles, Florence Nogrette, Daniel Barredo, Antoine Browaeys, and Thierry Lahaye. In situ equalization of single-atom loading in large-scale optical tweezer arrays. *Phys. Rev. A*, 106:022611, Aug 2022.
- [40] Udo Seifert. Stochastic thermodynamics, fluctuation theorems and molecular machines. *Reports on Progress in Physics*, 75(12), 2012.
- [41] V. Blickle, T. Speck, L. Helden, U. Seifert, and C. Bechinger. Thermodynamics of a colloidal particle in a time-dependent nonharmonic potential. *Phys. Rev. Lett.*, 96:070603, Feb 2006.
- [42] Jaehoon Bang, Rui Pan, Thai M Hoang, Jonghoon Ahn, Christopher Jarzynski, H T Quan, and Tongcang Li. Experimental realization of feynman’s ratchet. *New Journal of Physics*, 20(10):103032, Oct 2018.
- [43] Shoichi Toyabe, Takahiro Sagawa, Masahito Ueda, Eiro Muneyuki, and Masaki Sano. Experimental demonstration of information-to-energy conversion and validation of the generalized jarzynski equality. *Nature Physics*, 6(12):988–992, Dec 2010.
- [44] Antoine Bérut, Artak Arakelyan, Artyom Petrosyan, Sergio Ciliberto, Raoul Dillenschneider, and Eric Lutz. Experimental verification of landauer’s principle linking information and thermodynamics. *Nature*, 483(7388):187–189, Mar 2012.
- [45] Yonggun Jun, Mom čilo Gavrilov, and John Bechhoefer. High-precision test of landauer’s principle in a feedback trap. *Phys. Rev. Lett.*, 113:190601, Nov 2014.
- [46] Karel Svoboda, Christoph F. Schmidt, Bruce J. Schnapp, and Steven M. Block. Direct observation of kinesin stepping by optical trapping interferometry. *Nature*, 365(6448):721–727, Oct 1993.
- [47] Valentin Blickle and Clemens Bechinger. Realization of a micrometre-sized stochastic heat engine. *Nature Physics*, 8(2):143–146, Feb 2012.
- [48] Avinash Kumar and John Bechhoefer. Exponentially faster cooling in a colloidal system. *Nature*, 584(7819):64–68, Aug 2020.
- [49] Rémi Goerlich, Luís Barbosa Pires, Giovanni Manfredi, Paul-Antoine Hervieux, and Cyriaque Genet. Harvesting information to control nonequilibrium states of active matter. *Phys. Rev. E*, 106:054617, Nov 2022.
- [50] Arthur Alexandre, Maxime Lavaud, Nicolas Fares, Elodie Millan, Yann Louyer, Thomas Salez, Yacine Amarouchene, Thomas Guérin, and David S. Dean. Non-gaussian diffusion near surfaces. *Phys. Rev. Lett.*, 130:077101, Feb 2023.

- [51] Rémi Goerlich, Minghao Li, Luís Barbosa Pires, Paul-Antoine Hervieux, Giovanni Manfredi, and Cyriaque Genet. Experimental test of landauer’s principle for stochastic resetting, 2023.
- [52] Tongcang Li, Simon Kheifets, David Medellin, and Mark G. Raizen. Measurement of the instantaneous velocity of a brownian particle. *Science*, 328(5986):1673–1675, 2010.
- [53] Simon Kheifets, Akarsh Simha, Kevin Melin, Tongcang Li, and Mark G. Raizen. Observation of brownian motion in liquids at short times: Instantaneous velocity and memory loss. *Science*, 343(6178):1493–1496, 2014.
- [54] Thai M. Hoang, Rui Pan, Jonghoon Ahn, Jaehoon Bang, H. T. Quan, and Tongcang Li. Experimental test of the differential fluctuation theorem and a generalized jarzynski equality for arbitrary initial states. *Phys. Rev. Lett.*, 120:080602, Feb 2018.
- [55] Markus Rademacher, Michael Konopik, Maxime Debiossac, David Grass, Eric Lutz, and Nikolai Kiesel. Nonequilibrium control of thermal and mechanical changes in a levitated system. *Phys. Rev. Lett.*, 128:070601, Feb 2022.
- [56] Mario A. Ciampini, Tobias Wenzl, Michael Konopik, Gregor Thalhammer, Markus Aspelmeyer, Eric Lutz, and Nikolai Kiesel. Experimental nonequilibrium memory erasure beyond landauer’s bound, 2021.
- [57] Loïc Rondin, Jan Gieseler, Francesco Ricci, Romain Quidant, Christoph Delgado, and Lukas Novotny. Direct measurement of kramers turnover with a levitated nanoparticle. *Nature Nanotechnology*, 12(12):1130–1133, Dec 2017.
- [58] Jan Gieseler and James Millen. Levitated Nanoparticles for Microscopic Thermodynamics—A Review. *Entropy*, 20(5):326, April 2018.
- [59] Nikolai Kiesel, Florian Blaser, Uroš Deliĉ, David Grass, Rainer Kaltenbaek, and Markus Aspelmeyer. Cavity cooling of an optically levitated submicron particle. *Proceedings of the National Academy of Sciences*, 110(35):14180–14185, 2013.
- [60] Nadine Meyer, Andrés de los Rios Sommer, Pau Mestres, Jan Gieseler, Vijay Jain, Lukas Novotny, and Romain Quidant. Resolved-sideband cooling of a levitated nanoparticle in the presence of laser phase noise. *Phys. Rev. Lett.*, 123:153601, Oct 2019.
- [61] Tongcang Li, Simon Kheifets, and Mark G. Raizen. Millikelvin cooling of an optically trapped microsphere in vacuum. *Nature Physics*, 7(7):527–530, Jul 2011.

- [62] Jan Gieseler, Bradley Deutsch, Romain Quidant, and Lukas Novotny. Subkelvin parametric feedback cooling of a laser-trapped nanoparticle. *Phys. Rev. Lett.*, 109:103603, Sep 2012.
- [63] Felix Tebbenjohanns, Martin Frimmer, Andrei Militararu, Vijay Jain, and Lukas Novotny. Cold damping of an optically levitated nanoparticle to microkelvin temperatures. *Phys. Rev. Lett.*, 122:223601, Jun 2019.
- [64] Felix Tebbenjohanns, M. Luisa Mattana, Massimiliano Rossi, Martin Frimmer, and Lukas Novotny. Quantum control of a nanoparticle optically levitated in cryogenic free space. *Nature*, 595(7867):378–382, July 2021.
- [65] Lorenzo Magrini, Philipp Rosenzweig, Constanze Bach, Andreas Deutschmann-Olek, Sebastian G. Hofer, Sungkun Hong, Nikolai Kiesel, Andreas Kugi, and Markus Aspelmeyer. Real-time optimal quantum control of mechanical motion at room temperature. *Nature*, 595(7867):373–377, July 2021.
- [66] Sougato Bose, Anupam Mazumdar, Gavin W. Morley, Hendrik Ulbricht, Marko Toroš, Mauro Paternostro, Andrew A. Geraci, Peter F. Barker, M. S. Kim, and Gerard Milburn. Spin entanglement witness for quantum gravity. *Phys. Rev. Lett.*, 119:240401, Dec 2017.
- [67] Henning Rudolph, Klaus Hornberger, and Benjamin A. Stickler. Entangling levitated nanoparticles by coherent scattering. *Phys. Rev. A*, 101:011804, Jan 2020.
- [68] A. Vinante, A. Pontin, M. Rashid, M. Toroš, P. F. Barker, and H. Ulbricht. Testing collapse models with levitated nanoparticles: Detection challenge. *Phys. Rev. A*, 100:012119, Jul 2019.
- [69] Yuqiang Jiang, Tetsuya Narushima, and Hiromi Okamoto. Nonlinear optical effects in trapping nanoparticles with femtosecond pulses. *Nature Physics*, 6(12):1005–1009, Dec 2010.
- [70] Arthur Ashkin and James P Gordon. Stability of radiation-pressure particle traps: an optical earnshaw theorem. *Optics letters*, 8(10):511–513, 1983.
- [71] L. Bellando, M. Kleine, Y. Amarouchene, M. Perrin, and Y. Loyer. Giant diffusion of nanomechanical rotors in a tilted washboard potential. *Phys. Rev. Lett.*, 129:023602, Jul 2022.
- [72] J. A. Zielińska, F. van der Laan, A. Norrman, M. Rimlinger, R. Reimann, L. Novotny, and M. Frimmer. Controlling optomechanical libration with the degree of polarization. *Phys. Rev. Lett.*, 130:203603, May 2023.

- [73] Philip H. Jones, Onofrio M. Maragò, and Giovanni Volpe. *Optical Tweezers: Principles and Applications*. Cambridge University Press, 2015.
- [74] Susan E. Skelton Spesytyseva and Kishan Dholakia. Trapping in a material world. *ACS Photonics*, 3(5):719–736, May 2016.
- [75] B. Richards, E. Wolf, and Dennis Gabor. Electromagnetic diffraction in optical systems, ii. structure of the image field in an aplanatic system. *Proceedings of the Royal Society of London. Series A. Mathematical and Physical Sciences*, 253(1274):358–379, 1959.
- [76] Lukas Novotny and Bert Hecht. *Principles of Nano-Optics*. Cambridge University Press, 2 edition, 2012.
- [77] David S Simon. *A Guided Tour of Light Beams (Second Edition)*. 2053-2563. IOP Publishing, 2020.
- [78] Graham Milne, Kishan Dholakia, David McGloin, Karen Volke-Sepulveda, and Pavel Zemánek. Transverse particle dynamics in a bessel beam. *Opt. Express*, 15(21):13972–13987, Oct 2007.
- [79] John Lekner and Petar Andrejic. Nonexistence of exact solutions agreeing with the gaussian beam on the beam axis or in the focal plane. *Optics Communications*, 407:22–26, 2018.
- [80] Jan Gieseler, Lukas Novotny, and Romain Quidant. Thermal nonlinearities in a nanomechanical oscillator. *Nature Physics*, 9(12):806–810, Dec 2013.
- [81] Erik Hebestreit. *Thermal Properties of Levitated Nanoparticles*. Doctoral thesis, ETH Zurich, Zurich, 2017.
- [82] Ron Lifshitz and M. C. Cross. *Nonlinear Dynamics of Nanomechanical and Micromechanical Resonators*, chapter 1, pages 1–52. John Wiley & Sons, Ltd, 2008.
- [83] Marc T. Cuairan, Jan Gieseler, Nadine Meyer, and Romain Quidant. Precision calibration of the duffing oscillator with phase control. *Phys. Rev. Lett.*, 128:213601, May 2022.
- [84] Yacine Amarouchene, Matthieu Mangeat, Benjamin Vidal Montes, Lukas Ondic, Thomas Guérin, David S. Dean, and Yann Louyer. Nonequilibrium dynamics induced by scattering forces for optically trapped nanoparticles in strongly inertial regimes. *Phys. Rev. Lett.*, 122:183901, May 2019.
- [85] François Rivière. *Lévitación d'une nanoparticule de diamant dans le vide*. PhD thesis, Ecole Doctorale Ondes et Matière, 2021. Thèse de doctorat Physique Université Paris-Saclay 2021.

- [86] Asimina Arvanitaki and Andrew A. Geraci. Detecting high-frequency gravitational waves with optically levitated sensors. *Phys. Rev. Lett.*, 110:071105, Feb 2013.
- [87] Erik Hebestreit, Martin Frimmer, René Reimann, and Lukas Novotny. Sensing static forces with free-falling nanoparticles. *Phys. Rev. Lett.*, 121:063602, Aug 2018.
- [88] Vijay Jain, Jan Gieseler, Clemens Moritz, Christoph Dellago, Romain Quidant, and Lukas Novotny. Direct measurement of photon recoil from a levitated nanoparticle. *Phys. Rev. Lett.*, 116:243601, Jun 2016.
- [89] Lukas Martinetz, Klaus Hornberger, and Benjamin A. Stickler. Gas-induced friction and diffusion of rigid rotors. *Phys. Rev. E*, 97:052112, May 2018.
- [90] François Rivière, Timothée de Guillebon, Damien Raynal, Martin Schmidt, Jean-Sébastien Lauret, Jean-François Roch, and Loïc Rondin. Hot brownian motion of optically levitated nanodiamonds. *ACS Photonics*, 9(2):420–425, Feb 2022.
- [91] S. A. Beresnev, V. G. Chernyak, and G. A. Fomyagin. Motion of a spherical particle in a rarefied gas. part 2. drag and thermal polarization. *Journal of Fluid Mechanics*, 219:405–421, 1990.
- [92] N.I. Akhiezer. *The Classical Moment Problem: And Some Related Questions in Analysis*. University mathematical monographs. Oliver & Boyd, 1965.
- [93] George Deodatis and Raymond C. Micaletti. Simulation of highly skewed non-gaussian stochastic processes. *Journal of Engineering Mechanics*, 127(12):1284–1295, 2001.
- [94] Aleksei V. Chechkin, Flavio Seno, Ralf Metzler, and Igor M. Sokolov. Brownian yet non-gaussian diffusion: From superstatistics to subordination of diffusing diffusivities. *Phys. Rev. X*, 7:021002, Apr 2017.
- [95] Taylor Wampler and Andre C Barato. Skewness and kurtosis in stochastic thermodynamics. *Journal of Physics A: Mathematical and Theoretical*, 55(1):014002, Dec 2021.
- [96] Simon J. Julier and Jeffrey K. Uhlmann. New extension of the Kalman filter to nonlinear systems. In Ivan Kadar, editor, *Signal Processing, Sensor Fusion, and Target Recognition VI*, volume 3068, pages 182 – 193. International Society for Optics and Photonics, SPIE, 1997.
- [97] Hannes Risken. *Fokker-Planck Equation*, pages 63–95. Springer Berlin Heidelberg, Berlin, Heidelberg, 1996.

- [98] AA OPTO-ELECTRONIC. Acousto-optic theory application notes. <http://www.aaoptoelectronic.com/wp-content/uploads/documents/AAOPTO-Theory2013-4.pdf>, 2014.
- [99] Jan Gieseler, Romain Quidant, Christoph Dellago, and Lukas Novotny. Dynamic relaxation of a levitated nanoparticle from a non-equilibrium steady state. *Nature Nanotechnology*, 9(5):358–364, May 2014.
- [100] Weiqun Lu, Zeliang Gao, Qian Wu, Xiangxin Tian, Youxuan Sun, Yang Liu, and Xutang Tao. Tailored fabrication of a prospective acousto-optic crystal tite3o8 endowed with high performance. *J. Mater. Chem. C*, 6:2443–2451, 2018.
- [101] V. Venkataraman, Vasant Natarajan, and N. Kumar. Venkataraman, natarajan, and kumar reply:. *Phys. Rev. Lett.*, 98:189803, May 2007.
- [102] C. Simonelli, E. Neri, A. Ciamei, I. Goti, M. Inguscio, A. Trenkwalder, and M. Zaccanti. Realization of a high power optical trapping setup free from thermal lensing effects. *Opt. Express*, 27(19):27215–27228, Sep 2019.
- [103] Xiao Zhang, Yang Chen, Jianxiong Fang, Tishuo Wang, Jiaming Li, and Le Luo. Beam pointing stabilization of an acousto-optic modulator with thermal control. *Opt. Express*, 27(8):11503–11509, Apr 2019.
- [104] J. Kobayashi, Y. Izumi, M. Kumakura, and Y. Takahashi. Stable all-optical formation of bose–einstein condensate using pointing-stabilized optical trapping beams. *Applied Physics B*, 83(1):21–25, Apr 2006.
- [105] Felix Tebbenjohanns, Martin Frimmer, and Lukas Novotny. Optimal position detection of a dipolar scatterer in a focused field. *Phys. Rev. A*, 100:043821, Oct 2019.
- [106] T. Briant, P. F. Cohadon, M. Pinard, and A. Heidmann. Optical phase-space reconstruction of mirror motion at the attometer level. *The European Physical Journal D - Atomic, Molecular, Optical and Plasma Physics*, 22(1):131–140, Jan 2003.
- [107] T. J. Kippenberg and K. J. Vahala. Cavity optomechanics: Back-action at the mesoscale. *Science*, 321(5893):1172–1176, 2008.
- [108] Charlotte Bond, Daniel Brown, Andreas Freise, and Kenneth A. Strain. Interferometer techniques for gravitational-wave detection. *Living Reviews in Relativity*, 19(1):3, Feb 2017.
- [109] Carl G. Chen, Paul T. Konkola, Juan Ferrera, Ralf K. Heilmann, and Mark L. Schattenburg. Analyses of vector gaussian beam propagation and the validity of paraxial and spherical approximations. *J. Opt. Soc. Am. A*, 19(2):404–412, Feb 2002.

- [110] Kishan Dholakia and Pavel Zemánek. Colloquium: Gripped by light: Optical binding. *Rev. Mod. Phys.*, 82:1767–1791, Jun 2010.
- [111] Jakob Rieser, Mario A. Ciampini, Henning Rudolph, Nikolai Kiesel, Klaus Hornberger, Benjamin A. Stickler, Markus Aspelmeyer, and Uroš Delić. Tunable light-induced dipole-dipole interaction between optically levitated nanoparticles. *Science*, 377(6609):987–990, 2022.
- [112] L.G. Gouy. *Sur une propriété nouvelle des ondes lumineuses*. Mélanges scientifiques. Gauthier-Villars, 1890.
- [113] A. T. M. Anishur Rahman, A. C. Frangeskou, P. F. Barker, and G. W. Morley. An analytical model for the detection of levitated nanoparticles in optomechanics. *Review of Scientific Instruments*, 89(2):023109, 02 2018.
- [114] Marie-Sophie Hartig, Sönke Schuster, and Gudrun Wanner. Geometric tilt-to-length coupling in precision interferometry: mechanisms and analytical descriptions. *Journal of Optics*, 24(6):065601, May 2022.
- [115] Marie-Sophie Hartig, Sönke Schuster, Gerhard Heinzl, and Gudrun Wanner. Non-geometric tilt-to-length coupling in precision interferometry: mechanisms and analytical descriptions. *Journal of Optics*, 25(5):055601, Apr 2023.
- [116] G. P. Agrawal and M. Lax. Free-space wave propagation beyond the paraxial approximation. *Phys. Rev. A*, 27:1693–1695, Mar 1983.
- [117] T. Schmiedl and U. Seifert. Efficiency at maximum power: An analytically solvable model for stochastic heat engines. *Europhysics Letters*, 81(2):20003, dec 2007.
- [118] I. A. Martínez, É Roldán, L. Dinis, D. Petrov, J. M. R. Parrondo, and R. A. Rica. Brownian carnot engine. *Nature Physics*, 12(1):67–70, Jan 2016.
- [119] Andreas Dechant, Nikolai Kiesel, and Eric Lutz. All-optical nanomechanical heat engine. *Phys. Rev. Lett.*, 114:183602, May 2015.
- [120] D. Guéry-Odelin, A. Ruschhaupt, A. Kiely, E. Torrontegui, S. Martínez-Garaot, and J. G. Muga. Shortcuts to adiabaticity: Concepts, methods, and applications. *Rev. Mod. Phys.*, 91:045001, Oct 2019.
- [121] Ignacio A. Martínez, Artyom Petrosyan, David Guéry-Odelin, Emmanuel Trizac, and Sergio Ciliberto. Engineered swift equilibration of a brownian particle. *Nature Physics*, 12(9):843–846, Sep 2016.
- [122] Geng Li, H. T. Quan, and Z. C. Tu. Shortcuts to isothermality and nonequilibrium work relations. *Phys. Rev. E*, 96(1):012144, July 2017.

- [123] John A. C. Albay, Pik-Yin Lai, and Yonggun Jun. Realization of finite-rate isothermal compression and expansion using optical feedback trap. *Appl. Phys. Lett.*, 116(10):103706, March 2020.
- [124] Anne Le Cunuder, Ignacio A. Martínez, Artyom Petrosyan, David Guéry-Odelin, Emmanuel Trizac, and Sergio Ciliberto. Fast equilibrium switch of a micro mechanical oscillator. *Applied Physics Letters*, 109(11):113502, 2016.
- [125] Marie Chupeau, Sergio Ciliberto, David Guéry-Odelin, and Emmanuel Trizac. Engineered swift equilibration for brownian objects: from underdamped to overdamped dynamics. *New Journal of Physics*, 20(7):075003, Jul 2018.
- [126] Christine Zerbe, Peter Jung, and Peter Hänggi. Brownian parametric oscillators. *Phys. Rev. E*, 49:3626–3635, May 1994.
- [127] Andrei Militaru, Antonio Lasanta, Martin Frimmer, Luis L. Bonilla, Lukas Novotny, and Raúl A. Rica. Kovacs memory effect with an optically levitated nanoparticle. *Phys. Rev. Lett.*, 127:130603, Sep 2021.
- [128] John A. C. Albay, Govind Paneru, Hyuk Kyu Pak, and Yonggun Jun. Optical tweezers as a mathematically driven spatio-temporal potential generator. *Opt. Express*, 26(23):29906–29915, Nov 2018.
- [129] Erik Aurell, Carlos Mejía-Monasterio, and Paolo Muratore-Ginanneschi. Optimal protocols and optimal transport in stochastic thermodynamics. *Phys. Rev. Lett.*, 106:250601, Jun 2011.
- [130] Jin-Fu Chen. Optimizing brownian heat engine with shortcut strategy. *Phys. Rev. E*, 106:054108, Nov 2022.
- [131] Xiu-Hua Zhao, Zheng-Nan Gong, and Z. C. Tu. Low-dissipation engines: Microscopic construction via shortcuts to adiabaticity and isothermality, the optimal relation between power and efficiency. *Phys. Rev. E*, 106:064117, Dec 2022.
- [132] Johannes Piotrowski, Dominik Windey, Jayadev Vijayan, Carlos Gonzalez-Ballester, Andrés de los Ríos Sommer, Nadine Meyer, Romain Quidant, Oriol Romero-Isart, René Reimann, and Lukas Novotny. Simultaneous ground-state cooling of two mechanical modes of a levitated nanoparticle. *Nature Physics*, Mar 2023.
- [133] Carlos A. Plata, Antonio Prados, Emmanuel Trizac, and David Guéry-Odelin. Taming the Time Evolution in Overdamped Systems: Shortcuts Elaborated from Fast-Forward and Time-Reversed Protocols. *Phys. Rev. Lett.*, 127(19):190605, November 2021.

- [134] Marie Chupeau, Jannes Gladrow, Alexei Chepelianskii, Ulrich F. Keyser, and Emmanuel Trizac. Optimizing brownian escape rates by potential shaping. *Proceedings of the National Academy of Sciences*, 117(3):1383–1388, 2020.
- [135] Thai M. Hoang, Rui Pan, Jonghoon Ahn, Jaehoon Bang, H. T. Quan, and Tongcang Li. Experimental Test of the Differential Fluctuation Theorem and a Generalized Jarzynski Equality for Arbitrary Initial States. *Phys. Rev. Lett.*, 120(8):080602, February 2018.
- [136] C. Samanta, S. L. De Bonis, C. B. Møller, R. Tormo-Queralt, W. Yang, C. Urgell, B. Stamenic, B. Thibeault, Y. Jin, D. A. Czaplewski, F. Pistolesi, and A. Bachtold. Nonlinear nanomechanical resonators approaching the quantum ground state. *Nat. Phys.*, pages 1–5, June 2023.
- [137] Marc Roda-Llordes, Andreu Riera-Campeny, Davide Candoli, Piotr T. Grochowski, and Oriol Romero-Isart. Macroscopic Quantum Superpositions via Dynamics in a Wide Double-Well Potential, July 2023.
- [138] Lukas Neumeier, Mario A. Ciampini, Oriol Romero-Isart, Markus Aspelmeyer, and Nikolai Kiesel. Fast Quantum Interference of a Nanoparticle via Optical Potential Control, July 2022.
- [139] T. Weiss, M. Roda-Llordes, E. Torrontegui, M. Aspelmeyer, and O. Romero-Isart. Large quantum delocalization of a levitated nanoparticle using optimal control: Applications for force sensing and entangling via weak forces. *Phys. Rev. Lett.*, 127:023601, Jul 2021.
- [140] Bo Deng, Moritz Göb, Benjamin A. Stickler, Max Masuhr, Kilian Singer, and Daqing Wang. Amplifying a zeptonewton force with a single-ion nonlinear oscillator, May 2023.
- [141] G. Q. Cai and Y. K. Lin. Generation of non-gaussian stationary stochastic processes. *Phys. Rev. E*, 54:299–303, Jul 1996.
- [142] W.Q. Zhu and G.Q. Cai. Generation of non-gaussian stochastic processes using nonlinear filters. *Probabilistic Engineering Mechanics*, 36:56–62, 2014.
- [143] Guillaume Gauthier, Thomas A. Bell, Alexander B. Stilgoe, Mark Baker, Halina Rubinsztein-Dunlop, and Tyler W. Neely. *Chapter One - Dynamic high-resolution optical trapping of ultracold atoms*, volume 70, pages 1–101. Academic Press, Jan 2021.
- [144] Daniel Barredo, Vincent Lienhard, Sylvain de Léséleuc, Thierry Lahaye, and Antoine Browaeys. Synthetic three-dimensional atomic structures assembled atom by atom. *Nature*, 561(7721):79–82, Sep 2018.

- [145] Graham D. Bruce, James Mayoh, Giuseppe Smirne, Lara Torralbo-Campo, and Donatella Cassettari. A smooth, holographically generated ring trap for the investigation of superfluidity in ultracold atoms. *Phys. Scr.*, 2011(T143):014008, 2011.
- [146] Tomáš Čižmár and Kishan Dholakia. Tunable bessel light modes: engineering the axial propagation. *Opt. Express*, 17(18):15558–15570, Aug 2009.
- [147] Miguel A. Preciado, Kishan Dholakia, and Michael Mazilu. Generation of attenuation-compensating airy beams. *Opt. Lett.*, 39(16):4950–4953, Aug 2014.
- [148] B. Melo, I. Brandão, B. Silva Pinheiro da, R.B. Rodrigues, A.Z. Khoury, and T. Guerreiro. Optical trapping in a dark focus. *Phys. Rev. Appl.*, 14:034069, Sep 2020.
- [149] Matthew R. Foreman, Sherif S. Sherif, Peter R. T. Munro, and Peter Török. Inversion of the debye-wolf diffraction integral using an eigenfunction representation of the electric fields in the focal region. *Opt. Express*, 16(7):4901–4917, Mar 2008.
- [150] Ivan Vishniakou and Johannes D. Seelig. Differentiable optimization of the debye-wolf integral for light shaping and adaptive optics in two-photon microscopy. *Opt. Express*, 31(6):9526–9542, Mar 2023.
- [151] Xiaorui Yin. High frame-rate and low-latency control of Digital Micromirror Devices (DMD) using FPGA for ultracold atom-based quantum experiments, 2021.
- [152] Ahmed B. Ayoub and Demetri Psaltis. High speed, complex wavefront shaping using the Digital Micro-mirror Device. *Scientific Reports*, 11(1):18837, Sep 2021.
- [153] K. Visscher, G. J. Brakenhoff, and J. J. Krol. Micromanipulation by “multiple” optical traps created by a single fast scanning trap integrated with the bilateral confocal scanning laser microscope. *Cytometry*, 14(2):105–114, 1993.
- [154] Ignacio A. Martínez and Dmitri Petrov. Force mapping of an optical trap using an acousto-optical deflector in a time-sharing regime. *Appl. Opt.*, 51(22):5522–5526, Aug 2012.
- [155] K Henderson, C Ryu, C MacCormick, and M G Boshier. Experimental demonstration of painting arbitrary and dynamic potentials for bose–einstein condensates. *New Journal of Physics*, 11(4):043030, Apr 2009.

- [156] G. Condon, M. Rabault, B. Barrett, L. Chichet, R. Arguel, H. Eneriz-Imaz, D. Naik, A. Bertoldi, B. Battelier, P. Bouyer, and A. Landragin. All-optical bose-einstein condensates in microgravity. *Phys. Rev. Lett.*, 123:240402, Dec 2019.
- [157] Yonggun Jun and John Bechhoefer. Virtual potentials for feedback traps. *Phys. Rev. E*, 86:061106, Dec 2012.
- [158] Avinash Kumar and John Bechhoefer. Nanoscale virtual potentials using optical tweezers. *Applied Physics Letters*, 113(18), 10 2018. 183702.
- [159] Salambô Dago, Jorge Pereda, Sergio Ciliberto, and Ludovic Bellon. Virtual double-well potential for an underdamped oscillator created by a feedback loop. *Journal of Statistical Mechanics: Theory and Experiment*, 2022(5):053209, May 2022.
- [160] Yu Zheng, Lyu-Hang Liu, Xiang-Dong Chen, Guang-Can Guo, and Fang-Wen Sun. Arbitrary Non-equilibrium Steady State Construction with a Levitated Nanoparticle, April 2023.
- [161] Dimitris Trypogeorgos, Tiffany Harte, Alexis Bonnin, and Christopher Foot. Precise shaping of laser light by an acousto-optic deflector. *Opt. Express*, 21(21):24837–24846, Oct 2013.
- [162] B. Suassuna, B. Melo, and T. Guerreiro. Path integrals and nonlinear optical tweezers. *Phys. Rev. A*, 103(1):013110, January 2021.
- [163] Ignacio A. Martínez and Dmitri Petrov. Back-focal-plane position detection with extended linear range for photonic force microscopy. *Appl. Opt.*, 51(25):5973–5977, Sep 2012.
- [164] V. Delaubert, N. Treps, M. Lassen, C. C. Harb, C. Fabre, P. K. Lam, and H-A. Bachor. tem_{10} homodyne detection as an optimal small-displacement and tilt-measurement scheme. *Phys. Rev. A*, 74:053823, Nov 2006.
- [165] Yugang Ren, Enrique Benedetto, Harry Borrill, Yelizaveta Savchuk, Molly Message, Katie O’Flynn, Muddassar Rashid, and James Millen. Event-based imaging of levitated microparticles. *Applied Physics Letters*, 121(11), 09 2022. 113506.
- [166] Stefan Berg-Johansen, Martin Neugebauer, Andrea Aiello, Gerd Leuchs, Peter Banzer, and Christoph Marquardt. Microsphere kinematics from the polarization of tightly focused nonseparable light. *Opt. Express*, 29(8):12429–12439, Apr 2021.
- [167] Sandro Perrone, Giovanni Volpe, and Dmitri Petrov. 10-fold detection range increase in quadrant-photodiode position sensing for photonic force microscope. *Review of Scientific Instruments*, 79(10), 10 2008. 106101.

- [168] R. E. Kalman and R. S. Bucy. New Results in Linear Filtering and Prediction Theory. *Journal of Basic Engineering*, 83(1):95–108, 03 1961.
- [169] Mohinder S. Grewal and Angus P. Andrews. Applications of kalman filtering in aerospace 1960 to the present [historical perspectives]. *IEEE Control Systems Magazine*, 30(3):69–78, 2010.
- [170] J.-Y. Lee, J. Marotzke, G. Bala, L. Cao, S. Corti, J.P. Dunne, F. Engelbrecht, E. Fischer, J.C. Fyfe, C. Jones, A. Maycock, J. Mutemi, O. Ndiaye, S. Panickal, and T. Zhou. Future global climate: Scenario-based projections and near-term information. In V. Masson-Delmotte, P. Zhai, A. Pirani, S. L. Connors, C. Péan, S. Berger, N. Caud, Y. Chen, L. Goldfarb, M. I. Gomis, M. Huang, K. Leitzell, E. Lonnoy, J. B. R. Matthews, T. K. Maycock, T. Waterfield, O. Yelekçi, R. Yu, and B. Zhou, editors, *Climate Change 2021: The Physical Science Basis. Contribution of Working Group I to the Sixth Assessment Report of the Intergovernmental Panel on Climate Change*, book section 4. Cambridge University Press, Cambridge, UK and New York, NY, USA, 2021.
- [171] Francois Counillon, Ingo Bethke, Noel Keenlyside, Mats Bentsen, Laurent Bertino, and Fei Zheng. Seasonal-to-decadal predictions with the ensemble kalman filter and the norwegian earth system model: a twin experiment. *Tellus A: Dynamic Meteorology and Oceanography*, 66(1):21074, 2014.
- [172] Witlef Wieczorek, Sebastian G. Hofer, Jason Hoelscher-Obermaier, Ralf Riedinger, Klemens Hammerer, and Markus Aspelmeyer. Optimal state estimation for cavity optomechanical systems. *Phys. Rev. Lett.*, 114:223601, Jun 2015.
- [173] Ashley Setter, Marko Toroš, Jason F. Ralph, and Hendrik Ulbricht. Real-time kalman filter: Cooling of an optically levitated nanoparticle. *Phys. Rev. A*, 97:033822, Mar 2018.
- [174] S.J. Julier, Jeffrey K. Uhlmann, and H.F. Durrant-Whyte. A new approach for filtering nonlinear systems. *Proceedings of 1995 American Control Conference - ACC'95*, 3:1628–1632 vol.3, 1995.
- [175] S.J. Julier and J.K. Uhlmann. Unscented filtering and nonlinear estimation. *Proceedings of the IEEE*, 92(3):401–422, 2004.
- [176] Martin Brossard, Axel Barrau, and Silvère Bonnabel. A code for unscented kalman filtering on manifolds (ukf-m). In *2020 IEEE International Conference on Robotics and Automation (ICRA)*, pages 5701–5708, 2020.
- [177] Stephan Thaler and Julija Zavadlav. Learning neural network potentials from experimental data via differentiable trajectory reweighting. *Nature Communications*, 12(1):6884, Nov 2021.

- [178] Samuel S. Schoenholz and Ekin D. Cubuk. Jax m.d. a framework for differentiable physics. In *Advances in Neural Information Processing Systems*, volume 33. Curran Associates, Inc., 2020.
- [179] John Bechhoefer. *Control Theory for Physicists*. Cambridge University Press, 2021.
- [180] Eric A. Wan and Rudolph van der Merwe. *The Unscented Kalman Filter*, chapter 7, pages 221–280. John Wiley & Sons, Ltd, 2001.
- [181] S. Julier, J. Uhlmann, and H.F. Durrant-Whyte. A new method for the nonlinear transformation of means and covariances in filters and estimators. *IEEE Transactions on Automatic Control*, 45(3):477–482, 2000.
- [182] Quade Butler, Waleed Hilal, Brett Sicard, Youssef Ziada, and S. Andrew Gadsden. Generalizing the unscented Kalman filter for state estimation. In Ivan Kadar, Erik P. Blasch, and Lynne L. Grewe, editors, *Signal Processing, Sensor/Information Fusion, and Target Recognition XXXII*, volume 12547, page 1254703. International Society for Optics and Photonics, SPIE, 2023.
- [183] Leticia F. Cugliandolo. Out-of-equilibrium dynamics of classical and quantum complex systems. *Comptes Rendus Physique*, 14(8):685–699, 2013. Disordered systems / Systèmes désordonnés.
- [184] Rob Phillips. Schrödinger’s what is life? at 75. *Cell Systems*, 12(6):465–476, 2021.
- [185] Adolfo del Campo and Wojciech H. Zurek. Universality of phase transition dynamics: Topological defects from symmetry breaking. *International Journal of Modern Physics A*, 29(08):1430018, 2014.
- [186] Artemy Kolchinsky and David H. Wolpert. Dependence of dissipation on the initial distribution over states. *Journal of Statistical Mechanics: Theory and Experiment*, 2017(8):083202, Aug 2017.
- [187] Erik Aurell, Carlos Mejía-Monasterio, and Paolo Muratore-Ginanneschi. Boundary layers in stochastic thermodynamics. *Phys. Rev. E*, 85:020103, Feb 2012.
- [188] David Guéry-Odelin, Christopher Jarzynski, Carlos A Plata, Antonio Prados, and Emmanuel Trizac. Driving rapidly while remaining in control: classical shortcuts from hamiltonian to stochastic dynamics. *Reports on Progress in Physics*, 86(3):035902, Jan 2023.
- [189] L. G. Villanueva, E. Kenig, R. B. Karabalin, M. H. Matheny, Ron Lifshitz, M. C. Cross, and M. L. Roukes. Surpassing fundamental limits of oscillators using nonlinear resonators. *Phys. Rev. Lett.*, 110:177208, Apr 2013.

- [190] Roberto Benzi, Giorgio Parisi, Alfonso Sutera, and Angelo Vulpiani. Stochastic resonance in climatic change. *Tellus*, 34(1):10–16, 1982.
- [191] Fabing Duan, François Chapeau-Blondeau, and Derek Abbott. Weak signal detection: Condition for noise induced enhancement. *Digital Signal Processing*, 23(5):1585–1591, 2013.
- [192] Pengfei Xu, Yanfei Jin, and Yanxia Zhang. Stochastic resonance in an underdamped triple-well potential system. *Applied Mathematics and Computation*, 346:352–362, 2019.
- [193] Zijian Qiao, Jian Liu, Xin Ma, and Jinliang Liu. Double stochastic resonance induced by varying potential-well depth and width. *Journal of the Franklin Institute*, 358(3):2194–2211, 2021.
- [194] Jian Liu, Zijian Qiao, Xiaojian Ding, Bing Hu, and Chuanlai Zang. Stochastic resonance induced weak signal enhancement over controllable potential-well asymmetry. *Chaos, Solitons & Fractals*, 146:110845, 2021.
- [195] David H. Wolpert and Artemy Kolchinsky. Thermodynamics of computing with circuits. *New Journal of Physics*, 22(6):063047, Jun 2020.
- [196] Martin Frimmer, Karol Luszcz, Sandra Ferreiro, Vijay Jain, Erik Hebestreit, and Lukas Novotny. Controlling the net charge on a nanoparticle optically levitated in vacuum. *Phys. Rev. A*, 95:061801, Jun 2017.
- [197] Marie Chupeau, Benjamin Besga, David Guéry-Odelin, Emmanuel Trizac, Artyom Petrosyan, and Sergio Ciliberto. Thermal bath engineering for swift equilibration. *Phys. Rev. E*, 98(1):010104, July 2018.
- [198] Marco Baldovin, David Guéry-Odelin, and Emmanuel Trizac. Shortcuts to adiabaticity for lévy processes in harmonic traps. *Phys. Rev. E*, 106:054122, Nov 2022.
- [199] Édgar Roldán, Izaak Neri, Raphael Chetrite, Shamik Gupta, Simone Pigolotti, Frank Jülicher, and Ken Sekimoto. *Martingales for physicists*, 2023.
- [200] Gonzalo Manzano, Gülce Kardeş, Édgar Roldán, and David Wolpert. Thermodynamics of computations with absolute irreversibility, unidirectional transitions, and stochastic computation times, 2023.
- [201] S. Martínez-Garaot, M. Palmero, J. G. Muga, and D. Guéry-Odelin. Fast driving between arbitrary states of a quantum particle by trap deformation. *Phys. Rev. A*, 94:063418, Dec 2016.

- [202] Pinyu Wu, Rongxin Huang, Christian Tischer, Alexandr Jonas, and Ernst-Ludwig Florin. Direct measurement of the nonconservative force field generated by optical tweezers. *Phys. Rev. Lett.*, 103:108101, Sep 2009.
- [203] Benoît Mahault, Evelyn Tang, and Ramin Golestanian. A topological fluctuation theorem. *Nature Communications*, 13(1):3036, May 2022.
- [204] Adam Griffin, Marius Gaudesius, Robin Kaiser, Sergey Nazarenko, and Guillaume Labeyrie. Analysing spatiotemporal instabilities in magneto-optical traps with the tools of turbulence theory. *Europhysics Letters*, 141(2):25002, Jan 2023.

Résumé de la thèse

Durant la dernière décennie, la lévitation de nanoparticules dans le vide s'est illustrée comme une plateforme de choix pour l'étude de nombreux phénomènes, parmi lesquels les interactions élémentaires, la physique quantique à l'échelle mésoscopique, ainsi que la nano-thermodynamique hors d'équilibre. Comparée à d'autres systèmes, un atout majeur de cette approche réside dans le contrôle remarquable qu'il est possible d'exercer sur la nanoparticule et son environnement. Dans ce contexte, la maîtrise complète de l'évolution spatio-temporelle du potentiel de piégeage représente un ajout significatif aux techniques existantes, en permettant par exemple la génération de statistiques non Gaussiennes.

Un premier objectif de cette thèse est l'étude et le contrôle de la dynamique hors équilibre d'une nanoparticule dans le régime sous-amorti, dont l'importance est à la fois fondamentale et pratique, étant donné qu'une grande partie des systèmes nano-mécaniques opère dans ce régime.

La nature stochastique des processus thermodynamiques à l'œuvre a d'abord été étudiée à travers la relaxation d'une particule en lévitation entre deux équilibres thermiques. A ainsi été mis en lumière un temps de relaxation caractéristique, correspondant au temps nécessaire à la dissipation de l'énergie de la particule dans son environnement. Dans le régime sur-amorti (à pression ambiante ou dans des fluides), le temps de relaxation dépend linéairement de l'amortissement, alors que dans le régime sous-amorti (dans le vide), il est inversement proportionnel à l'amortissement.

Par la suite, des protocoles de raccourcis vers l'équilibre ont pour la première fois été implémentés et testés dans le régime sous-amorti, permettant d'accélérer le retour à l'équilibre de la particule d'un ordre de grandeur. Comparé au régime sur-amorti où des protocoles similaires ont été précédemment étudiés, le régime sous-amorti nécessite de contrôler non seulement l'évolution de la distribution des positions de la particule, mais aussi celle des vitesses. Surmontant ce défi expérimental, le retour à l'équilibre a pu être accéléré de plus d'un ordre de grandeur.

Par ailleurs, pour de modestes accélérations, ces protocoles se sont avérés robustes, au sens où un protocole défini pour accélérer l'équilibre d'un mode d'oscillation donné était également efficace à plus basse fréquence, ce qui revêt un intérêt certain pour les systèmes multimodes couramment rencontrés à ces échelles.

Dans un deuxième temps, la génération et la caractérisation de potentiels de formes arbitraires ont été explorées, avec comme objectif initial d'étendre l'étude de processus thermodynamiques au cas de potentiels non harmoniques, pour lesquels les non-linéarités entrent en jeu.

Parmi les multiples techniques existantes pour générer ces potentiels, le choix s'est porté sur l'utilisation d'un modulateur acousto-optique. En le contrôlant à l'aide d'un signal multifréquences soigneusement défini, il est alors possible de diffracter plusieurs faisceaux lasers en contrôlant leur position et leur intensité. La superposition de ces faisceaux permet ainsi de générer des potentiels de formes arbitraires : harmonique, plat, double puits. . .

Une première approche a alors consisté à étudier les potentiels générés par la superposition de deux faisceaux que l'on écarte progressivement, pour lesquels la fréquence caractéristique d'oscillation est déterminable analytiquement. Le bon accord entre prédictions théoriques et mesures expérimentales confirme la finesse du contrôle ainsi atteint.

Enfin, pour reconstituer de façon non ambiguë la forme du potentiel à partir de la dynamique réelle de la particule, une utilisation originale du filtre de Kalman sans parfum (*Unscented Kalman Filter*) a permis d'étendre la plage de linéarité de la détection d'un facteur cinq, couvrant ainsi toute l'étendue du potentiel.

Ce travail ouvre la voie à l'étude de transformations générales d'état à état entre potentiels arbitraires, et offre de nouvelles perspectives à l'étude de la thermodynamique à l'échelle nanométrique.